Lightweight Aluminum Structures with Embedded Reinforcement Fibers via Ultrasonic Additive Manufacturing

A Thesis

Presented in Partial Fulfillment of the Requirements for the Degree
Master of Science in the Graduate School of The Ohio State
University

By

Matthew Scheidt, B.S.

Graduate Program in Department of Mechanical Engineering

The Ohio State University

2016

Master's Examination Committee:

Professor Marcelo Dapino, Advisor

Professor Farhang Pourboghrat

© Copyright by

Matthew Scheidt

2016

Abstract

Ultrasonic additive manufacturing (UAM) is a state of the art, low temperature, solid-state metal welding 3-D printing process. Metal foil, referred to as a tape, approximately 0.006 in. (0.1524 mm) thick, is fed through an automated feeder, and is welded, through the use of pressure and 20 kHz ultrasonic vibrations, to a base plate and/or additional foil, stacking, to build up material. The welder is integrated within a Computer Numerically Controlled (CNC) framework that uses standard machining operations to remove materials to create complex geometries, before and/or after each weld pass. With relatively low welding temperatures, thermally sensitive materials can be embedded, allowing for integrated sensing and thermal expansion control. Additionally, materials can be embedded that allow for the strengthening and lightweighting of structures. This thesis focuses on two aspects related to increasing the strength along the axis that tapes are welded, otherwise known as the weld direction. The primary focus of this research is to achieve lightweighting by embedding high strength/low density materials within an aluminum matrix using UAM. This method of creating composites revealed a reduction in strength of the metal matrix due to the UAM process. Investigating the cause of this reduction in strength became the second focus area of this thesis.

The first aspect of this research explores different lightweight and strong materials to integrate within a welded area to increase axial strength. The embedded materials explored include metal wires, ceramic fibers, thermoplastics, thermoset polymers and MetPreg, a commercial off the shelf metal matrix composite. Additionally, Al 6061-H18 tape was welded to 0.9 mm 5052-O baseplate, becoming the metal matrix for the embedded materials. Normalizing for density, all added materials increase the specific strength of the metal matrix alone. A key finding is the significance of the interface strength between the fibers and the matrix when channels are used to integrate strengthening materials into a structure.

The second aspect of this research is a design of experiments study to explore the effects of weld parameters on the strength, in the weld direction, of UAM created parts in order to understand the cause for the reduction in strength compared to pre-welded materials. Weld force, weld speed, and weld amplitude are varied across the parameters used for previous design of experiment studies, using both 1 kW and 9 kW welding systems. This study shows statistically significant correlations with weld force, weld speed and weld amplitude on the tensile strength of manufactured parts in the weld direction. Additionally, weld force, speed and amplitude are shown to significantly correlate with the failure strain in tension. A new weld energy density term is introduced that correlates with X-tensile stress-strain behavior of UAM constructed tensile coupons. The strongest and weakest samples tested show vastly different weld quality suggesting increasing weld direction strength is negatively correlated with gapless welds.

Acknowledgments

I would like to thank my advisor, Professor Marcelo Dapino for giving me an opportunity to work within the Smart Materials and Structures Laboratory, focusing on Ultrasonic Additive Manufacturing. The amount that I was able to learn, the experience gained and the lessons learned being a part of the lab were invaluable. Thanks to Professor Farhang Pourboghrat for serving on my committee, and Professor Soledad Fernandez for her help with statistical analysis. I would also like to thank Dr. Adam Hehr and Dr. Leon Headings for serving as mentors throughout my time in the lab, and Dr. Ryan Hahnlen for helping to steer the direction of my research.

Additionally, I would like to thank my colleagues, Dr. Xiang Chen, who contributed to modeling efforts, and Dr. Paul Wolcott, Bryant Gingerich, Brad Losey, Jack Schomer, and Gowtham Venkatraman for their help with different aspects of this research, training and support.

I would also like to thank the sponsors of my research, including the National Science Foundation Industry/University Cooperative Research Center on Smart Vehicle Concepts.

Vita

2006	B.S. Human Resource Management, New School University.
2009	B.S. Mechanical Engineering, Honors, Purdue University.
2014-present	Graduate Research Associate, Ohio State University.

Fields of Study

Major Field: Mechanical Engineering

Studies in Ultrasonic Additive Manufacturing: Professor Marcelo Dapino

Table of Contents

Appendices 129

List of Tables

Table **Page**

List of Figures

Chapter 1: Introduction

1.1 Motivation

Automotive and aerospace companies are interested in lightweighting their vehicles and craft without sacrificing strength. Lighter weight vehicles can travel farther and/or faster with the same fuel usage. With corporate average fuel economy standards [1] pushing an ever increasing drive toward better fuel economy and the cost of sending one kilogram into space being around $22,000 [2], the need to make components and structures lighter is real and is becoming increasingly demanding. One method that can be used to lightweight structures while maintaining strength is through continuous fiber reinforced components constructed using Ultrasonic Additive Manufacturing (UAM).

1.2 Ultrasonic Additive Manufacturing

1.2.1 General Description of UAM Machine and Process

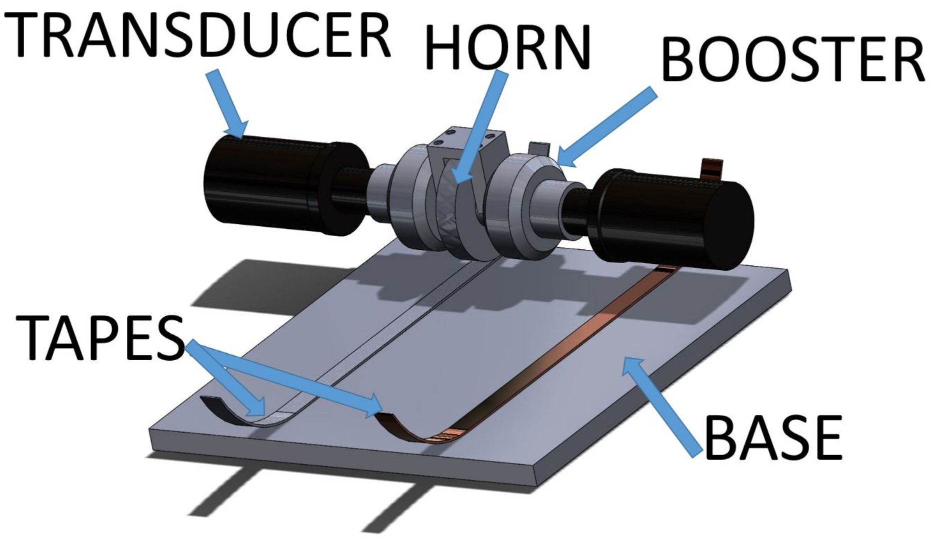

Figure 1.1: Graphic showing the 9 kW Fabrisonic UAM weld assembly.

UAM is a low temperature solid-state metal welding process. A horn, or sonotrode, is vibrated at 20 kHz with two piezoelectric transducers, shown in Figure 1.1, vibrating in tandem. Metal foils, or tapes, are usually fed under the textured horn as part of an automated process. The horn applies both a normal force and transverse 20 kHz vibration to the foil against an anvil in a Computer Numerically Controlled (CNC) 3-axis vertical mill framework, shown in Figures 1.2 and 1.3. The anvil moves longitudinally along the direction of the foil, ultrasonically welding the foil to the anvil. The foil is then cut and an additional layer is allowed to be deposited. The term anvil is used loosely to mean what the horn pushes the foil against, which could be a baseplate that could be integrated into the UAM welded part, or the most recently deposited tape.

Figure 1.2: Fabrisonic's SonicLayer® 4000, Ohio State University's UAM machine.

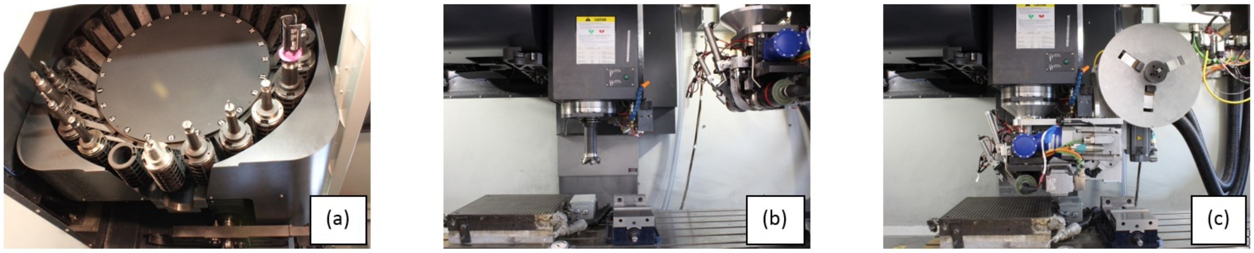

Figure 1.3: Welder treated as a tool within the CNC framework. (a) Tool magazine, which holds up to 25 different tools. (b) Clamshell cutter loaded in spindle and welder in storage position. (c) Welder loaded in spindle.

As an intermediate step, material can be removed from the anvil or the deposited tape(s) using standard metal cutting tooling and can then be welded over with additional tapes. Being integrated into a CNC framework allows for the creation of complex shapes and internal features that cannot be created through forging or through other additive processes. Figure 1.3 shows how the welder is treated as a tool, showing it loaded it in the spindle and in its storage location, as well as the tool magazine.

1.2.2 UAM Welding and Bond Formation

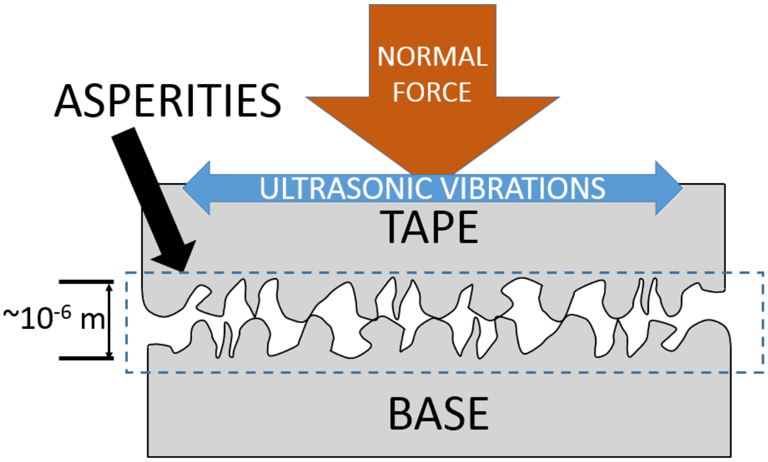

Figure 1.4: Normal force and ultrasonic vibrations applied to the tape by the horn. This causes plastic deformation and shearing of asperities allowing for nascent surfaces to be in intimate contact forming a metal-metal bond.

Solid state welding occurs when nascent surfaces of a metal come into contact. In the UAM process, this is accomplished through a normal force which pushes the horn against a tape and the anvil, ultrasonic vibrations applied perpendicular to the weld direction, and relative motion between the tape and the baseplate, see Figure 1.4. With the applied normal force and shearing action of the vibrating horn, asperities, or tiny peaks and valleys, on the surface of metals are plastically deformed at both base plate and tape and are collapsed exposing nascent surfaces. The nascent surfaces are in intimate contact, approximately 10^{-9} m, and form a metal-metal bond under the horn. The bond interface undergoes grain refinement, with the grain size changing as much as two orders of magnitude [3] as a result of the plastic deformation. The horn rolls with the motion of the base underneath to weld a tape to the base. The tapes are additively built up layer by layer as part of a UAM build.

1.2.3 UAM Process Parameters

1. **Normal Force:** Within the CNC framework, the UAM welder is treated as a tool with custom additional fixturing for support. Between the welder and the spindle is a load cell that is used for force control during the UAM process. The welder is capable of applying up to 2,250 lbf (10 kN) of normal force during the welding process.

2. **Speed:** Speed is defined as the relative motion between the horn and the anvil in the longitudinal direction of the tape feed. The maximum speed with which the welder can operate is 300 in/min (127 mm/sec).

3. **Amplitude:** Two 5 kW transducers are mounted to the sonotrode and vibrate in unison to drive the horn near 20 kHz, one of the natural frequencies of the horn. The horn is tuned to operate at around 20 kHz, the driving frequency of the transducers. The maximum amplitude of the horn vibration that has been

observed is $\sim$50 μm, peak to peak, which is achieved with the help of boosters with mass at half wavelengths, shown in Figure 1.1.

4. **Temperature:** The vacuum chuck that secures most of the parts that are produced on OSU's welder has embedded heating elements. The base can be heated to up to 400 ^{o}F.

5. **Spot Parameters:** The spot parameters are force, amplitude and dwell time. The force and amplitude are no different than the force and amplitude described above except that they are only applied for the prescribed dwell time, which is limited by the manufacturer's software to less than 1 sec. The spot parameters allow for the welder to stay in one spot long enough to ideally weld the tape to the base or proceeding layer, as applicable, before moving along the weld direction and continuing the weld, at which point the programmed force, speed and amplitude are used for the remainder of the weld.

1.3 Composite Behavior and Theory

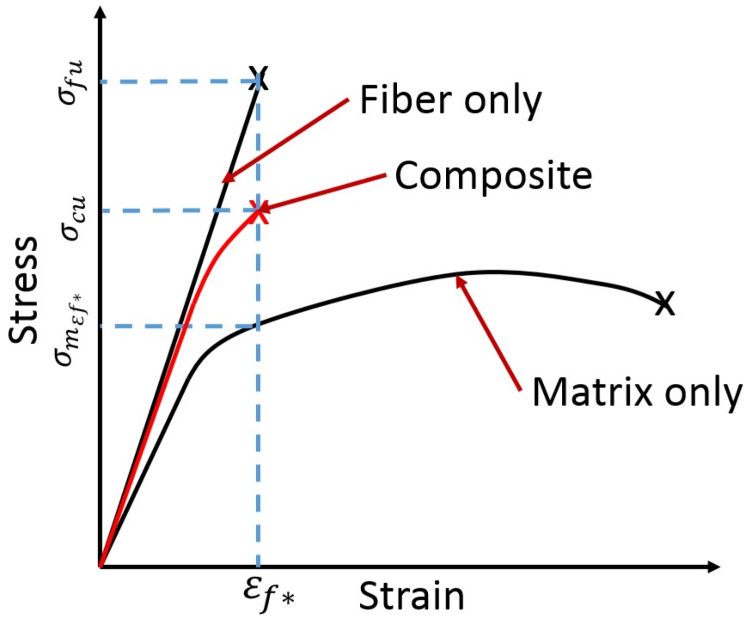

Figure 1.5: Graph depicting terms used as part of calculations of modified rule of mixtures for long fiber reinforced composites. Composite failure (σ_{cu}) is based on volume fraction of fiber and matrix.

Metal Matrix Composites (MMCs) are of special interest in UAM, and are the basis for the research within this document. The UAM process allows for selective placement of fibers within the metal matrix allowing for the creation of higher strength and lighter weight components with reduced bulk density compared with bulk metal properties. For illustrative purposes, the below is an example of how fibers can be used within a metal matrix to increase overall strength and stiffness with each term represented graphically in Figure 1.5. The modified rule of mixtures [4, 5] ,

$$\sigma_{cu}(V_f) = \sigma_{fu}V_f + (\sigma_m)_{\epsilon f^*}(1 - V_f), \tag{1.1}$$

represents the calculation required to predict the theoretically attainable Ultimate Tensile Strength (UTS) for a given composite where σ_{fu} is the ultimate strength of fibers, $(\sigma_m)_{\epsilon f^*}$ is the matrix stress at fiber fracture strain, V_f is the volume fraction of fibers, and σ_{cu} is the longitudinal strength of composite material, as a function of volume fraction. This model assumes that there is no slip between the matrix and the fibers, as well as homogeneity within the sample along the stressed axis. While a useful tool in helping to direct which fibers and matrices may work together to provide increase strength or stiffness, it cannot be used to predict behavior in composites with slip between a matrix and fiber.

1.4 Testing and Observations

1.4.1 Tensile Testing

To characterize stress-strain behavior in tension, tensile testing is conducted in accordance with ASTM-E8 [6]. Test constructions must conform to the specifications for sub-sized dog-bones with dimensions as shown in ASTM-E8 for sub-sized dog-bones. Tensile testing is conducted at what is determined to be quasi-static for the test, approximately 0.050 in/min (0.021 mm/s). During the test, load and displacement are recorded. Strain, which is defined as change in length divided by original length, and engineering stress, which is defined as the force divided by the original cross-sectional area of the gage region, are plotted against each other [7]. Force is measured through an in-line load cell. There are several ways of measuring strain described below.

On-Contact Strain Measurement

There are two primary methods used for on-contact strain measurement, strain gages and extensometers.

1. **Strain Gages:** Strain gages are made of a material that has an electrical resistance that varies with strain. A voltage source is applied to the strain gage and the voltage across the strain gage is measured. Strain gages are devices that are traditionally epoxied to the surface to be measured. High quality strain gages are somewhat expensive and time consuming to mount. Depending upon the strain of the sample being tested and the range of the strain gage, along with the fragility of the strain gages, they can have limited re-usability. Strain gages can effect the overall performance of a sample because they can act as a composite would, potentially reinforcing a sample. Strain gages are ideally suited to measure strain within a material's elastic region. Failure strain is generally not possible to adequately capture in tensile samples because of the need to have failure occur at the location of the strain gage.

2. **Extensometers:** Extensometers use built in strain gages to measure strain as the two connection points deflect under a tensile or compressive axial force. Extensometers mount to a sample and are held in place with rubber-bands or springs. The connection points are of fixed initial length, and require enough of a normal force against the sample to remain rigidly fixed to the sample throughout the duration of the test. They are somewhat expensive and fragile,

but reusable. Because of their construction, they have a limited range. Generally, an extensometer can capture strain of a failed sample as long as the failure occurs between the connection points.

Non-Contact Strain Measurement

There are several means of inferring and measuring strain without being in contact with the sample. Although not all inclusive, the following list discusses three different methods.

1. **Load Frame Displacement:** Utilizing the load frame's displacement output is by far the simplest approach to inferring strain. However, there are many sources of error that affect the strain measurement. For one, by design, the samples have a narrowed gage region, and a larger gripped section to ensure that failure occurs in the gage region. The filleted area and un-gripped areas of the sample undergo strain during testing, albeit to a lesser degree due to the larger cross-sectional area. Additionally, the grips as well as the load frame, although ideally minute, are strained during loading. All of this strain is not easily accounted for when determining strain of the sample using a load frame's displacement.

2. **Laser Extensometers:** A laser extensometer can be used similarly to a traditional extensometer. Considered to be a non-contact form of measuring strain, the laser extensometer requires a pair of reflective tape pieces or markers along the gage section. A laser system tracks the motion of the marker set and calculates the relative motion of the markers to each other, providing the change in

length needed for a strain calculation. This system is relatively expensive, but provides repeatable and representative strain measurements.

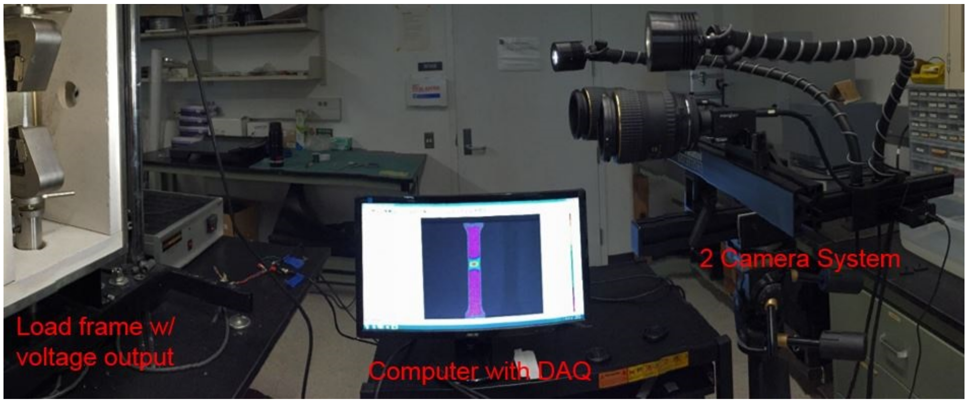

Figure 1.6: Ohio State University Smart Material and Structures Laboratory's DIC system setup for a tensile test. The tensile sample is installed in the load frame on the left, the cameras, on the right, are set up to observe the sample throughout the test. The software, which correlates the images with the voltage signals from the load frame, showing a post-processed sample on the screen is in the center.

3. **Digital Image Correlation:** Digital Image Correlation (DIC) is another non-contact means of measuring displacement and strain during testing. Additionally, DIC can be used as a means of surface mapping of static objects. Three-dimensional DIC uses a set of cameras, mounted at an angle with respect to each other, with the sample to be photographed within the field of view of both cameras. The cameras are calibrated using plates of evenly spaced dots, of known geometry, with multiple images of the plates at different aspect angles. Once calibration is complete, the system is able to coordinate the movement of subsets of pixels in the image, with physical 3-D motion. The resolution

is based on pixels, and the software's ability to track the motion of the pixels from image to image. At the same time each image is taken, a Data Aquisistion (DAQ) system takes in voltage inputs that correlate to force measurements. The advantage to DIC over a laser extensometer, is that DIC allows for full field strain measurements, while the laser extensometer will only track the relative motion of two points. Motion in all three dimensions can be captured using DIC, providing insight into material behavior that would otherwise remain unobserved. A photograph of the test setup is shown in Figure 1.6, with the tensile sample installed in the load frame on the left, the cameras, on the right, set up to observe the sample throughout the test, and the software showing a post-processed sample on the screen (center).

DIC systems are relatively expensive. Like the laser extensometer, they require additional time to setup and calibrate, which is not needed when using an on-contact extensometer. With DIC, each set of images is a data point that must be post-processed to extract strain information. Depending on the number of data points, and the resolution needed to for adequate results, post-processing can take an extended amount of time to extract data compared with other strain measurement techniques. Additionally, because each image set represents a data point, using a five megapixel camera, a set of images uses roughly ten megabytes of hard drive space, becoming very memory intensive.

Even though DIC is computer memory intensive, and takes an extended amount of time to setup and process results compared with other methods, it was the primary means of measuring strain during this study.

1.4.2 Fiber Pullout Testing

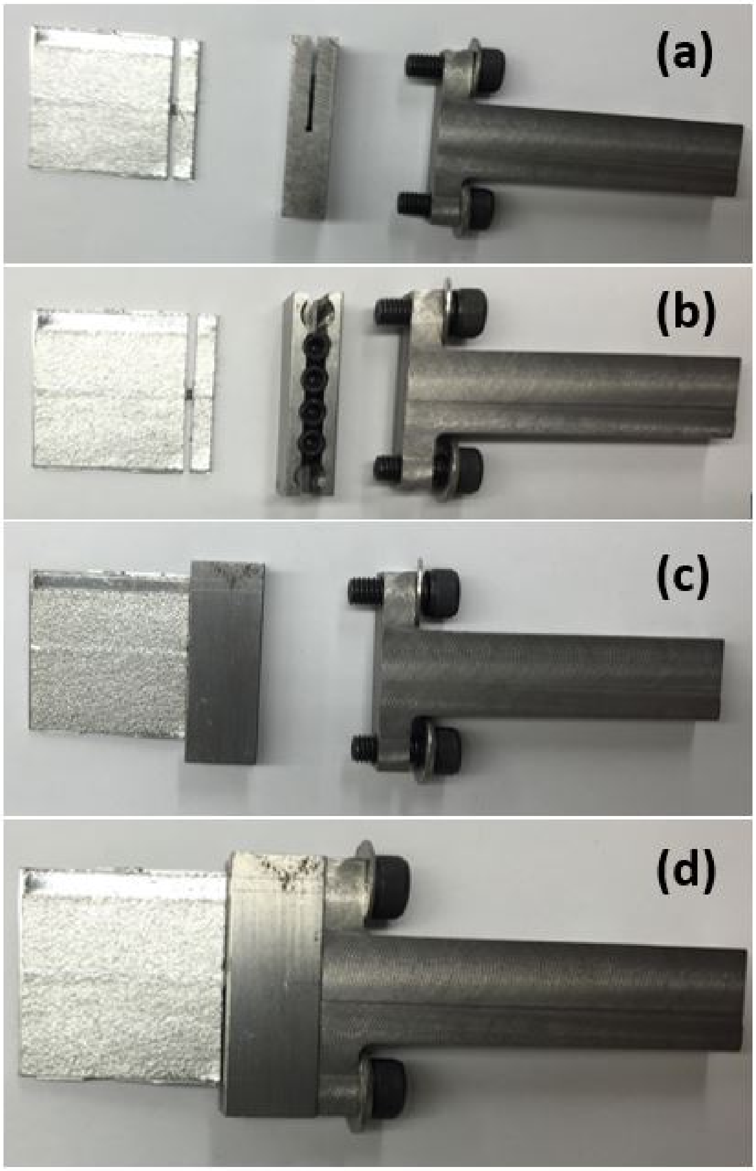

Figure 1.7: Fiber pull sample test rig setup. Images (a) and (b) show the disassembled fixture with a sample on the left. The sample's fibers slide into the slot shown in (a). The tab is held in place with set screws shown in (b). The sample with the bottom fixture attached is shown in (c). Image (d) shows the sample and fixture before they are loaded into standard tensile grips.

Although fiber pullout testing has been around since the 1950s, where researchers constructed single fiber composites and pulled out the fiber to model failure of the composite material [8], there is no standardized test available. Hehr et al. [9] developed a testing fixture, shown in Figure 1.7 with an aluminum matrix fiber pull sample, that allows the fiber alone to bear load during the testing. Small tabs are created using a custom CNC program that hold the fiber and represent the load bearing capabilities of the fiber throughout a sample. To achieve a representative sample, the critical fiber length (l_c) must satisfy

$$l_c > \frac{d_{eff}\sigma_f}{2\tau_m}, \tag{1.2}$$

where d_{eff} is the effective diameter of the fiber, σ_f is the fracture stress of the fiber, and τ_m is the maximum shear stress of the matrix [8, 5]. At this l_c, the center of the fiber will reach σ_f when the composite is under load. During testing, the load behavior as the fiber is pulled out is plotted as a function of displacement which allows for the determination of bonding characteristics and frictional behavior. This force displacement profile can be used to model fiber-matrix behavior.

1.4.3 Optical Microscopy

Optical microscopy is a useful tool for qualitative analysis of UAM constructed parts. It allows for the observation of voids within the material, if present, as well as the observation of consolidation of metal around fibers in UAM created metal matrix composites.

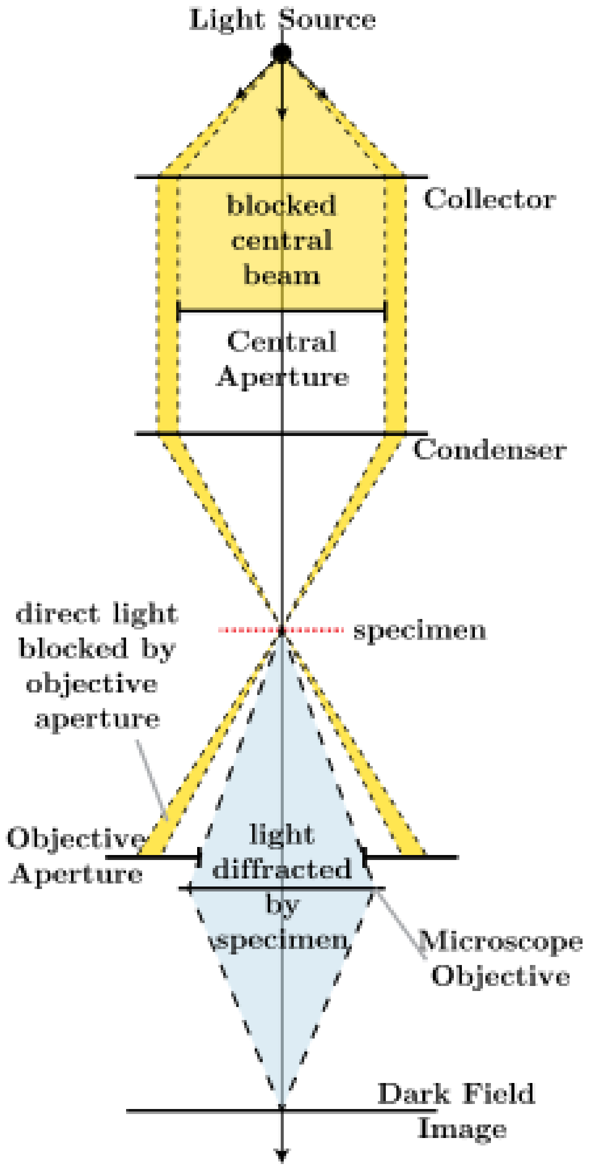

Figure 1.8: Graphical illustration of how light is captured using Dark field microscopy [10].

Dark field microscopy blocks light from hitting the specimen normal to the sample plane. This allows for light that hits the sample at an angle, not normal to the sample plane, to be visible. This allows for observing different materials at the polished surface, but also makes any sample imperfections or polishing artifacts which cause changes in the reflective plane visible. The graphic in Figure 1.8 represents this method of microscopy.

1.4.4 Weld Quality

UAM has been shown to produce high quality welds [11]. The weld quality of UAM has been defined multiple ways, including Linear Weld Density (LWD) [12, 13, 14] and push pin testing [11, 15, 16].

LWD is the proportion of bonded area to un-bonded area along the layer interface [12]. LWD relies on visual voids at the weld interface. Voidless looking welds do not necessarily correspond to consistent joint strength between layers due to the inability to observe microstucture and the possibility of polishing artifacts and smearing of material over void regions limiting the effectiveness of LWD. The Fabrisonic 9 kW welding system has shown to generate essentially voidless welds, making LWD obsolete as a weld quality quantification tool.

Push pin testing, while not a conventional ASTM standardized test, has been used to both qualitatively and quantitatively compare weld quality in the build direction [11, 15, 16]. Push-pin testing is used where LWD cannot be used. The failure mechanism, as well as the load magnitude and profile, are used to identify high or low quality welds to identify weld quality qualitatively and quantitatively, respectfully.

1.5 Design of Experiments

The idea to design experiments systematically with a view to their statistical analysis was first presented by Mann [17]. It is important to select the right experimental design for the desired outcome, and the experimental design is dependent on the reason for performing the experiment to [18]:

1. determine the principle causes of variation in a measured response.
2. find the conditions that give rise to a maximum or minimum response.
3. compare the responses achieved at different settings of controllable variables.
4. obtain a mathematical model in order to predict future responses.

An additional concern when designing an experiment is cost, both time and money. For example, a full factorial design includes all possible combinations of parameters. This is a very good design for measuring effects and interactions, but can involve many more experiments than a fractional factorial design. An example of a fractional factorial design was developed by Genechi Taguchi, for off-line quality control [19]. The purpose of off-line quality control is to put a product on target with minimum variation [19], but has been shown to be effective for analyzing the UAM process, and determining optimal weld parameters [11, 20].

After a design of experiments has been constructed, analysis of variance (ANOVA) can be conducted on a linear model of the form

$$y_{ijk} = \mu + \alpha_i + \beta_j + \gamma_k + \alpha_i\beta_j + \alpha_i\gamma_k + \beta_j\gamma_k + \alpha_i\beta_j\gamma_k + e_{ijk}, \tag{1.3}$$

where y_{ijk} are the observations corresponding to different parameter levels, μ is the overall mean, $\alpha/\beta/\gamma$ are input parameters with i, j, k representing different levels, and e_{ijk} is the unobservable random error. The ANOVA analysis supplies confidence intervals, whereby the general acceptance of a 95% confidence interval, or a p-value of less than 0.05, indicates a statistically significant term within the model [21]. The model initially assumes all individual and combinations of effects are significant. During analysis, terms determined to be statistically insignificant are removed.

1.6 Objectives

This thesis explores multiple means of adding different continuous materials for the purpose of lightweighting, attempting to maximize the volume fraction of reinforcement to reach the highest attainable strength to weight ratios. To that end, multiple tensile coupons were created using different base materials as the matrix to maximize ease of transition into industrial applications. Different types of materials were also investigated as potential reinforcement including polymers, metals and ceramics.

During the construction of the above coupons, it was noted that the post weld tensile behavior of the matrix was degraded compared to the pre-weld tensile behavior of the tapes. An experimental design was created that looks at the affect of weld force, weld speed and weld amplitude on the ultimate tensile strength and failure strain of UAM welded components. The insight gained from this experiment allows for better understanding of the weld parameter's affect on strength and ductility to develop a parameter set that can help to maximize strength, without sacrificing weld quality.

Chapter 2: Reinforced Metal Matrix Composites Using Ultrasonic Additive Manufacturing

2.1 Motivation

As discussed in Chapter 1, combining materials of high strength and stiffness with generally inexpensive and ductile materials, such as aluminum, allows for a matrix to be strengthened and stiffened in order to make parts either stronger, or lighter with the same mechanical properties. This chapter explores the use of different fibers and embedding methods that can be used to strengthen aluminum substrates using UAM.

2.2 Candidate Reinforcement Materials

Multiple reinforcement materials were explored: Metpreg, wires, and various fiber bundles. Metpreg is a metal matrix composite composed of 1100 series aluminum as the matrix and Al_2O_3 as the fiber reinforcement. The fibers explored include: high strength steel music wire, silicon carbide (SiC) ceramic wires, aramid (Kevlar$^{®}$) thread and tows, PBO (Zylon$^{®}$) and UHMWPE (Dyneema$^{®}$). Each of the reinforcing materials are described below.

Embedding reinforcing materials through the use of UAM has been demonstrated to be possible in literature. Many high strength materials have been combined to

Table 2.1: Composite fiber properties

	Yarn Count	**Density**	**Cross-Sectional Area of 1 tow**	**Tensile Strength**	**Specific Strength**	**Elongation at Break**
	[dtex]	**[g/cm^3]**	**[cm^2]**	**[GPa]**	**[MPa-m^3/kg]**	**[%]**
HSS	-	7.85	1.82×10^{-4}	2.8	0.36	14
UHMWPE	1740	0.975	1.79×10^{-3}	3.4	3.49	3.5
Zylon	1700	1.54	1.10×10^{-3}	5.8	3.77	3.5
Aramid	241	1.45	1.66×10^{-4}	2.7	1.84	3.1
SiC	-	3	1.59×10^{-4}	3.9	1.3	1

add strength to otherwise low strength materials [22, 23, 24, 25]. MetPreg has been welded with Al 3003-H18 [23, 24, 25]. High strength steel wires along with steel wire meshes have been embedded to add strength uniaxially and bidirectionally, respectively [13, 22, 23, 26]. Silicon carbide fibers have been embedded individually in Al 3003 [13, 20, 22, 23]. This research focuses on different materials and different fiber embedment techniques, where different base materials and channel geometries are used to integrate larger volume fractions of reinforcement. As an example, previous researchers have constructed samples with 0.77% volume fraction of reinforcing material to see an increase in stiffness of 8.9% [26]. Some of the reinforcement volume fractions achieved in this research approach 12%. The previous research was conducted using 1 kW capable UAM welders, whereas this research uses a UAM welded capable of inputing 9 kW of power to the transducer sets.

2.3 Continuous Fiber Reinforcement

2.3.1 UAM Reinforcement with MetPreg

MetPreg is a continuous fiber reinforced composite with Al-1100 as the matrix and Al_2O_3 fibers as the reinforcement produced by Touchstone Research Laboratory.

The advertised properties for MetPreg are shown in Table 2.2, however, local testing showed MetPreg to have a UTS of 668 MPa, with a standard deviation of 12 MPa, as compared to the advertised 1450 MPa.

Table 2.2: Advertised properties of MetPreg [27].

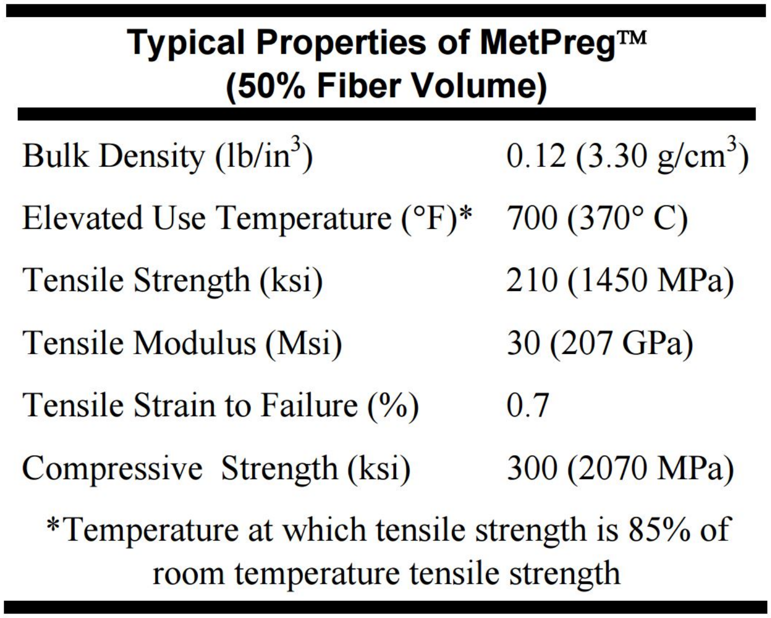

Typical Properties of MetPreg™
(50% Fiber Volume)

Bulk Density (lb/in^3)	0.12 (3.30 g/cm^3)
Elevated Use Temperature (°F)*	700 (370° C)
Tensile Strength (ksi)	210 (1450 MPa)
Tensile Modulus (Msi)	30 (207 GPa)
Tensile Strain to Failure (%)	0.7
Compressive Strength (ksi)	300 (2070 MPa)

*Temperature at which tensile strength is 85% of room temperature tensile strength

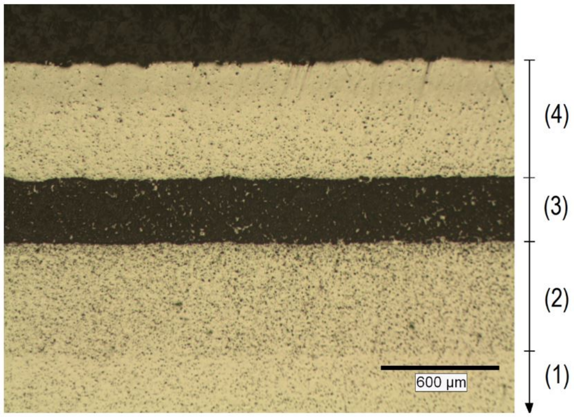

Figure 2.1: Al 6061/MetPreg Weld [(1) Base Plate Material; (2) 4 Layers of Al 6061 Tape; (3) 1 Layer of MetPreg; (4) 4 Layers of Al 6061 Tape] Dark spots that are observed in layer (2) and appear to be more dense than in layer (4) are believed to be ceramic composite polishing artifacts that became embedded in the surface of the Al 6061 as part of the polishing process. Also, the MetPreg layer appears very dark in the above image.

MetPreg was welded between layers of Al 6061-H18 to verify welding ability and cross sections were mounted and polished to examine the interfaces. Figure 2.1 shows the one tape of MetPreg welded in between layers of Al 6061-H18. The MetPreg layer appears very dark in Figure 2.1. The sample was re-polished to better show the MetPreg layer and interface (Figure 2.2). The polishing techniques allowed for individual fibers of Al_2O_3 to become more visible against the aluminum matrix.

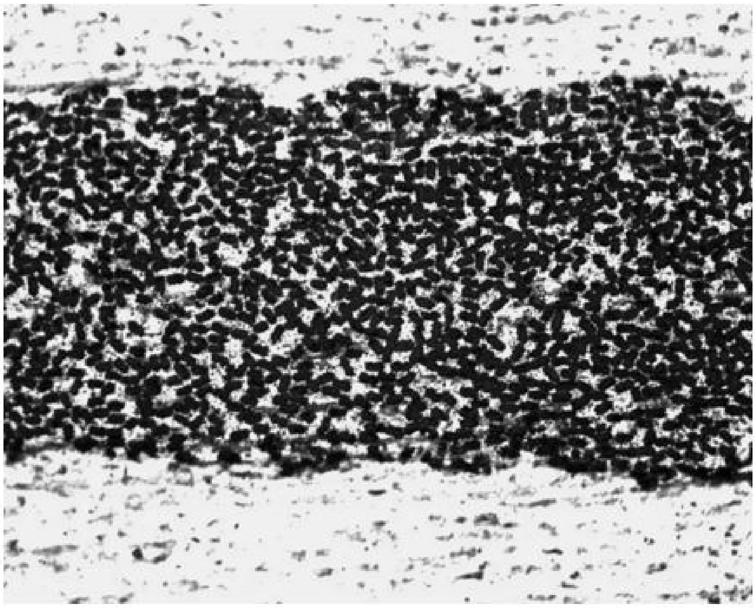

Figure 2.2: Al 6061/MetPreg weld after re-polishing sample shown in Figure 2.1.

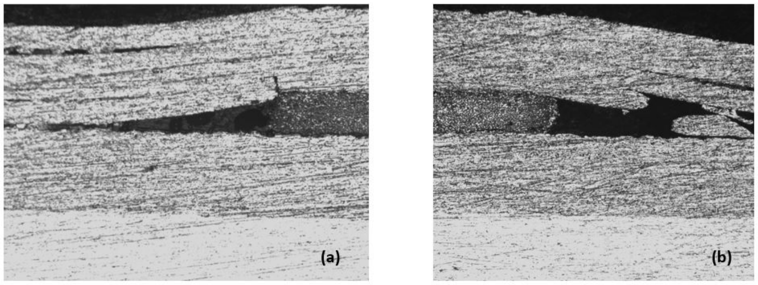

Figure 2.3: Al 6061/MetPreg weld right edge (a) and left edge (b) after re-polishing sample shown in Figure 2.1.

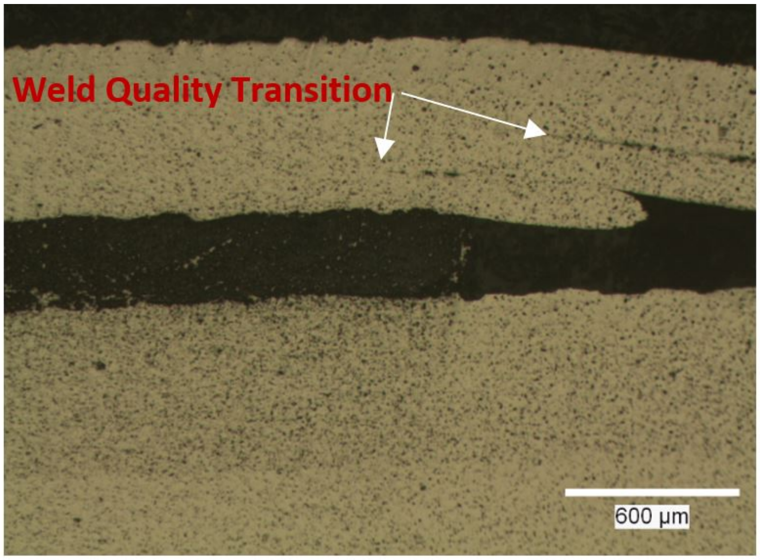

Figure 2.4: Al 6061/MetPreg weld right edge.

Figure 2.3 and Figure 2.4 show the left and right edges of the MetPreg/Al 6061 weld where the 1 in. (25.4 mm) 6061 tape hangs over the 0.5 in. (12.7 mm) MetPreg strip. The same view is shown with different polishing techniques. Visibly, especially in Figure 2.4, the weld quality transition can be seen just to the inside of the MetPreg tape where subsequent additional layers are welded to each other as the stiffness of the layered region increases.

Adding MetPreg to a structure does not require any pre-machining operations to integrate to a structure through the UAM process, which is a huge advantage to other reinforcement methods discussed in this thesis. However, while MetPreg has a lot of potential, the fact that its strength did not perform to its advertised value, and that it is difficult to machine to post-weld net shape dimensions, led to the pursuit of different reinforcement material candidates. If MetPreg can be produced reliably, the difficulties associated with machining may be worthwhile to work through. Tensile results are presented in Section 2.5.

2.3.2 UAM Reinforcement with High Strength Steel Music Wire

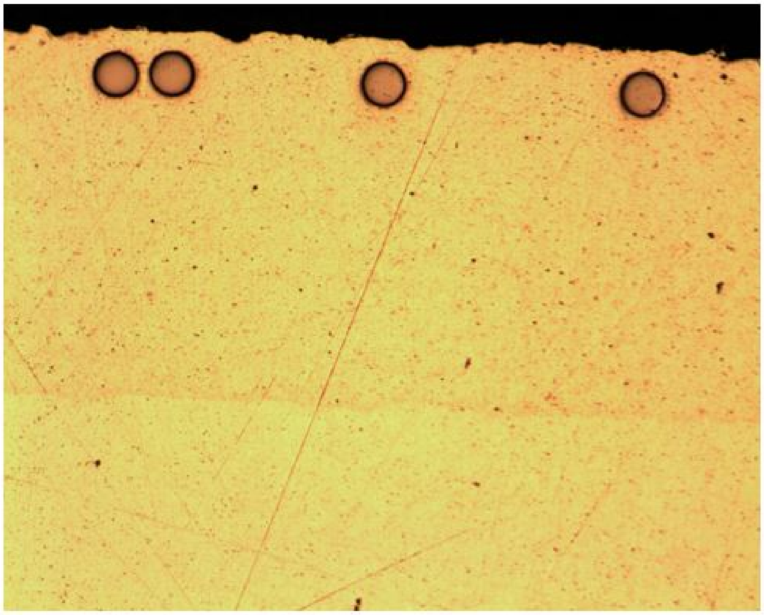

Figure 2.5: 0.006" HSS wire embedded in Al 6061-H18.

High Strength Steel (HSS) music wire is produced under the ASTM Standard Specification for Steel Wire, Music Spring Quality [28]. The HSS wire used during these tests was commercially available music wire. To test the ability to weld wires into an Al 6061-H18 matrix, (4) 0.006 in. (0.1524 mm) phosphate coated HSS piano wires were embedded between layers of Al 6061-H18 tape. The wires were mounted under minimal tension to keep them stationary. Micrographs of the wires embedded within the aluminum, Figures 2.5 and 2.6, show that the aluminum consolidated around the HSS wires without the need for channels. Some drift of the wire placement along the weld direction occurred through the welded region. Channels could help to prevent this drift, but at the cost of labor, machine time and tooling to cut precision channels that could yield similar substrate consolidation results. Welding parameters are listed in Appendix A.

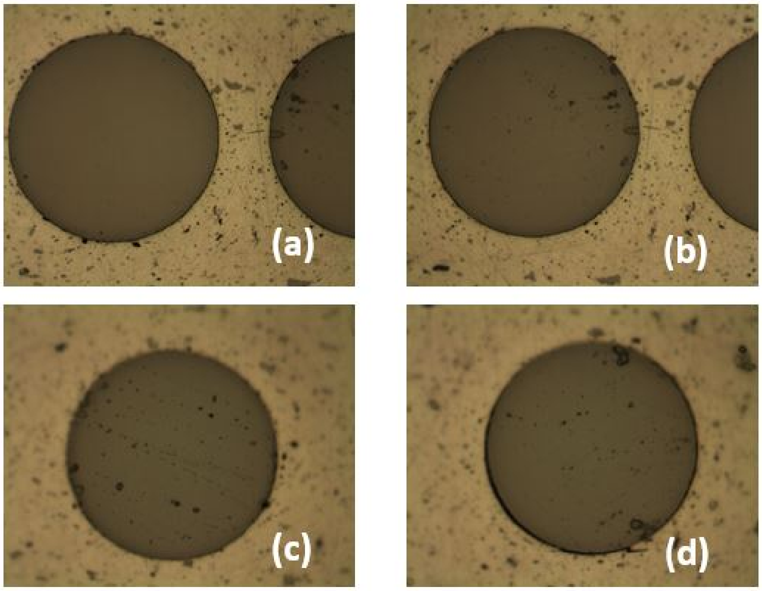

Figure 2.6: 0.006" HSS Wire Embedded in Al 6061-H18

An attempt to embed (20) HSS wires within a 0.25 in. (6.35 mm) wide strip was conducted. As shown in Figure 2.7, the fibers drifted and created a serpentine shape as the welder attempted to weld them into place. It is believed that this is due to the wires rolling as the welder passes over them, not bonding, and subsequently causing the shiny strip.

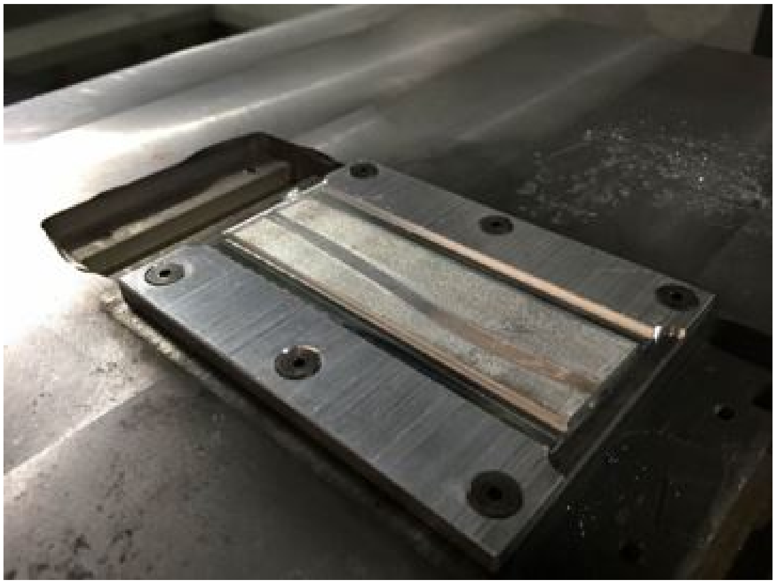

Figure 2.7: Twenty 0.006” diameter HSS wire attempt in Al 6061-H18.

When the number of wires was reduced to (10), the welder was able to successfully weld over them, leaving a much less visible area where the wires were embedded underneath. Figure 2.8 shows this sample setup before and after the weld. The samples were cut out of the plates using a CNC machine. Only after destructive testing was it possible to determine that all of the wires were present within the test section. Figure 2.8(b) shows an expanded area in the center of the sample where the HSS wires were embedded.

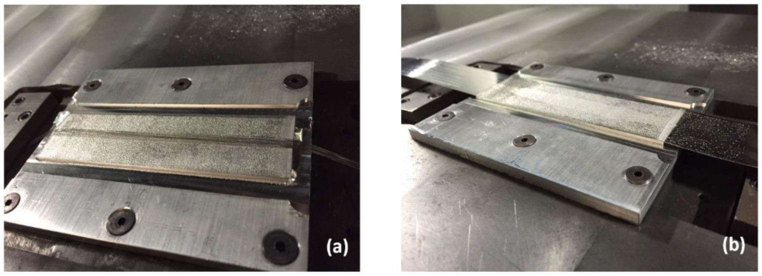

Figure 2.8: (a) Ten 0.006 in. diameter HSS wires laid out before welding over. (b) Ten 0.006 in. diameter HSS wires after welding over.

HSS wires proved to be possible to effectively embed, but the maximum volume fraction of wires was limited due to needing enough space between each wire to allow for consolidation of matrix material. Additionally, as a lightweighting method for aluminum, steel may not eb the best choice. With the steel being more dense, the added strength that comes from embedding it to aluminum is not as great as other polymer and ceramic materials. Although being able to embed the wires without creating channels was a huge benefit, other materials that offer more strength and add less weight were chosen for further investigation. Tensile testing results are presented in Section 2.5.

2.3.3 UAM Reinforcement with Aramid Threads

Aramid thread, 0.006 in. (0.1524 mm) in diameter, was purchased commercially from a thread supplier. In order to better observe the thread's fibers, a bundle of aramid threads was mounted in epoxy (Figure 2.9) to observe their appearance under high power optical microscopy. Two different imaging methods were used to observe the fibers. Bright field and dark field microscopy, Figure 2.10(a) and Figure 2.10 (b) respectively, were used to observe the individual fibers within the epoxy, with bright field better highlighting individual fibers. Figure 2.11 shows a cross-section of a single thread and that the aramid thread is constructed of a collection of aramid fibers, 8 μm in diameter.

Figure 2.9: Bundle of aramid threads mounted in epoxy to observe thread cross-section.

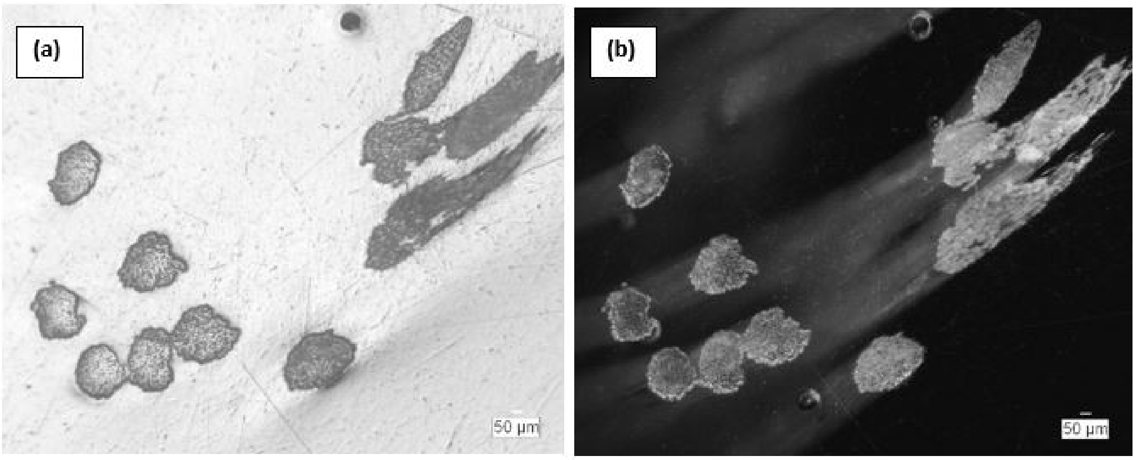

Figure 2.10: Close up of bundle of aramid threads mounted in epoxy to observe thread cross-section, with (a) using bright field imaging and (b) using dark field imaging.

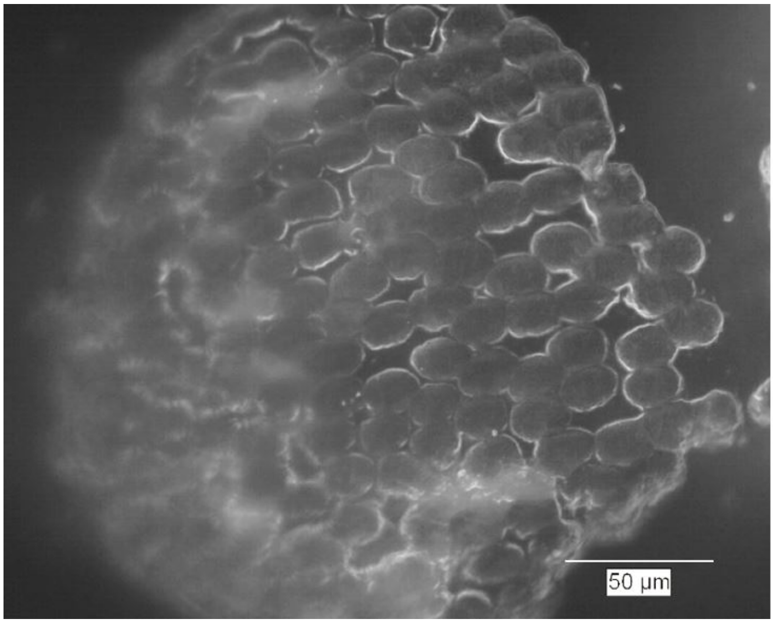

Figure 2.11: Single aramid thread mounted in epoxy to observe thread cross-section.

An attempt was made, without channels, to embed four 0.006 in. (0.1524 mm) aramid threads between layers of Al 6061-H18 tape. The threads were mounted under minimal tension to keep them stationary. Welding parameters are listed in Appendix A. Figure 2.12 shows the resultant aftermath, with the tape failing to stick at all in the beginning of the weld, and the tape tearing over the threads toward the end of the weld. The threads did not break, but were severely flattened and somewhat fused together. The underside of the aluminum tape directly above the fibers had a highly polished finish after the welding pass. This response presented the need to use channels when welding over aramid.

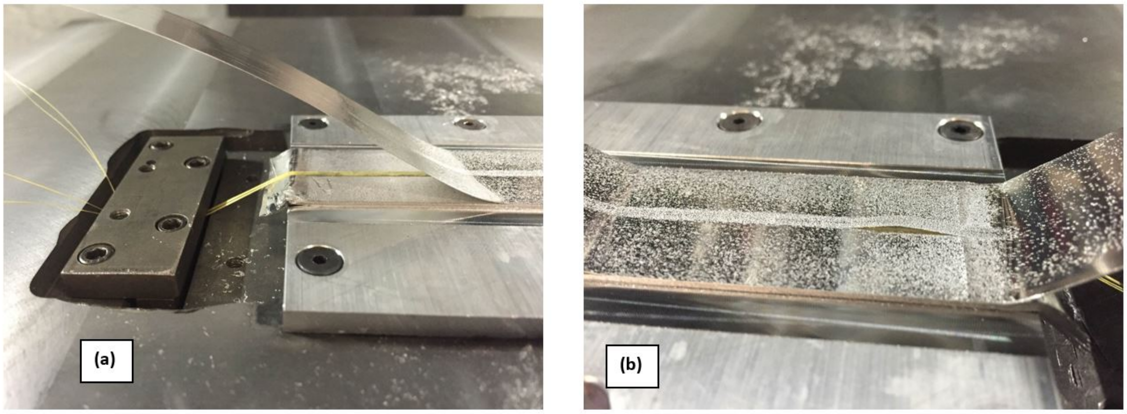

Figure 2.12: Initial attempt to embed four aramid threads without channels, (a) beginning of weld, (b) end of weld.

An attempt was then made to embed the threads into channels to determine minimum depth of channel to obtain an ultrasonic weld to encapsulate one aramid fiber. Four channels were cut to house the threads as the welder passed over them.

The channels were cut with a 0.010 in. (0.245 mm) diameter end mill at 0.002, 0.003, 0.004 and 0.005 in. (0.0508, 0.0762, 0.1016 and 0.127 mm) in 3 layers of UAM added Al 6061 H-18 (Figure 2.13 (a)). Four threads of 0.006 in. diameter aramid fiber were placed into the channels and held taut with a custom clamping mechanism and were then welded over with one layer of 0.006 in. thick Al 6061 H-18 tape. The resultant weld is shown in Figure 2.13 (b). After visually examining the weld, it appeared that the thread in the 0.002 in. channel was loose, the 0.003 in. channel thread was nearly encapsulated and the 0.004 in. and 0.005 in. were fully encapsulated.

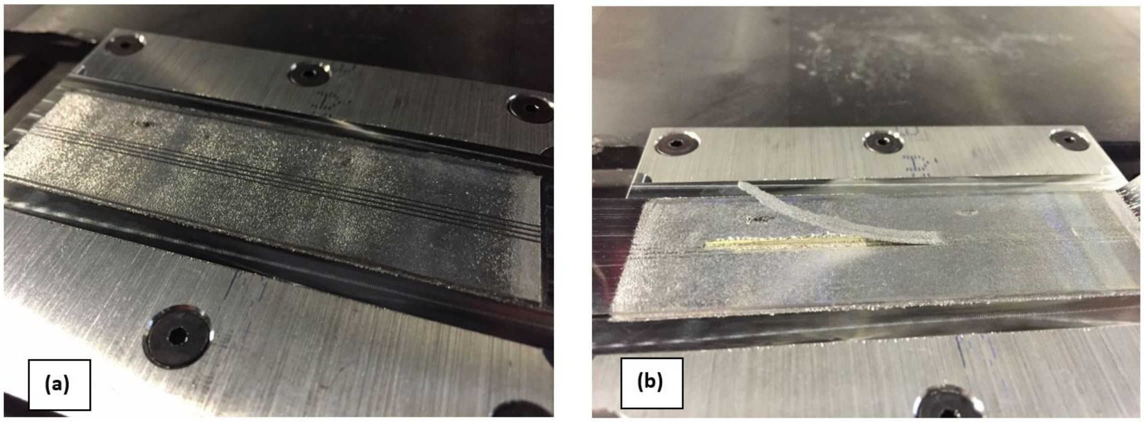

Figure 2.13: Initial attempt to embed four aramid threads with varying channel depths, (a) before welding, (b) after welding.

Figure 2.14 and Figure 2.15 show the channels using dark field imaging. Both figures show the individual fibers within the channels, Figure 2.14 showing two embedded fibers per image, and Figure 2.15 showing each fiber individually and at a higher magnification. Although the encapsulation of the fibers in the 0.002 inch and 0.003 inch channels appears to be more complete, weld quality is poor during the beginning of the weld due to the portion of the thread rising above the channel causing a lubricating effect, not allowing welds around the channels and subsequently causing tape tearing. The 0.005 inch deep channel appears to be too large allowing for a large void within the channel. By counting the number of visible fibers shown in Figure 2.15 (c), there are approximately 140 fibers per 0.006 in. diameter aramid thread.

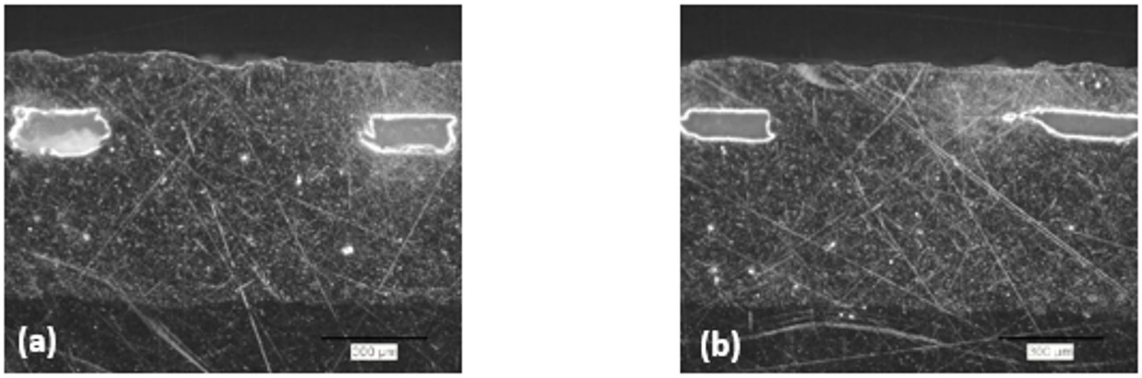

Figure 2.14: Dark field images (a) 0.005 in. and 0.004 in. channel (left to right), (b) 0.003 in. and 0.002 in. channel (left to right).

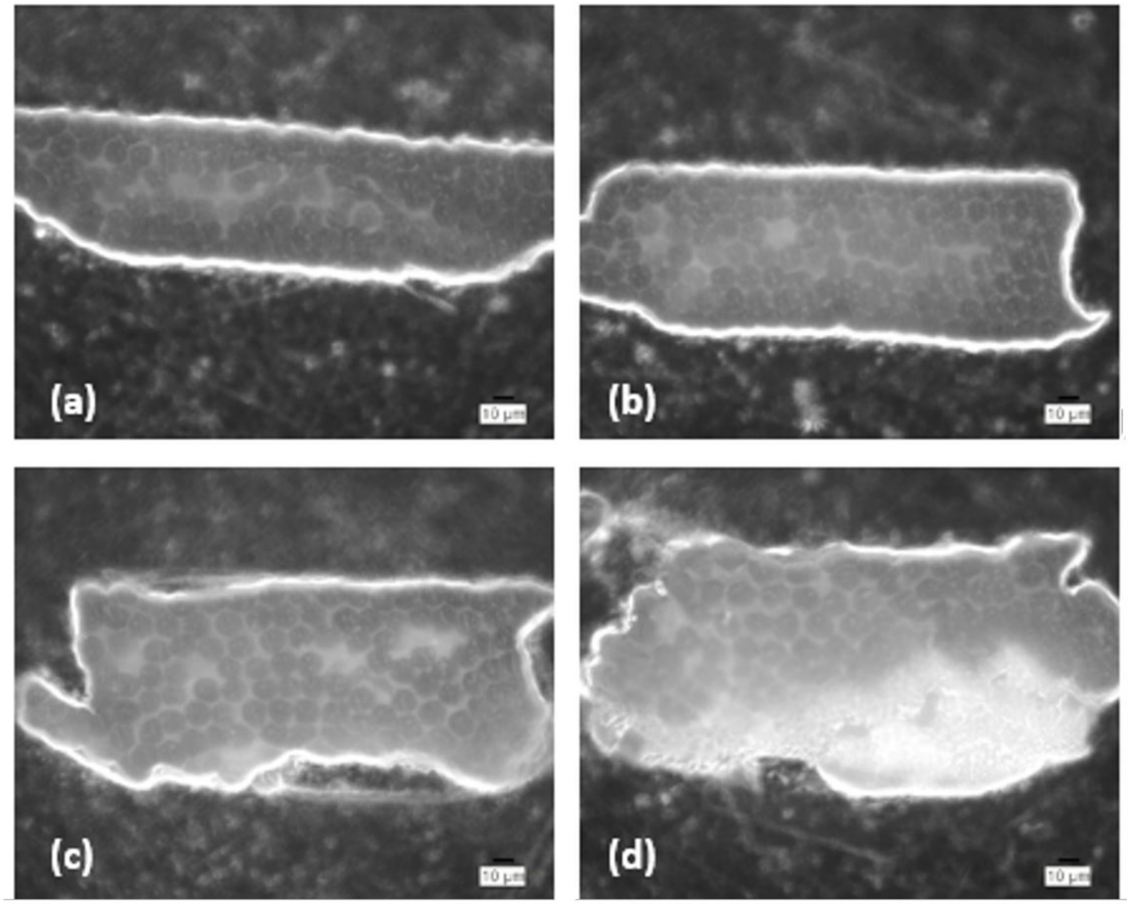

Figure 2.15: Dark field images (a) 0.002 in., (b) 0.003 in., (c) 0.004 in. and (d) 0.005 in. channel depth.

Assuming that the channel depth is accurate, the thread is a solid and closely packed within the channel, and that there is no flow of aluminum from the channel wall or welded tape into the channel, the table shows the expected void area. Table 2.3 helps to explain why the weld was unsuccessful for the 0.002 in. channel; there was not enough room within the channel for the welder to encapsulate the material.

Table 2.3: Estimated channel void area for single aramid fiber embedment.

	Channels			
Channel Depth [in]	0.005	0.004	0.003	0.002
Channel Area [in^2] (0.01 in. End Mill)	5E-5	4E-5	3E-5	2E-5
Expected Void Area [in^2] (0.006 in. Diam. Thread)	2.173E-05	1.17E-05	1.73E-06	-8.3E-06

Although this is a theoretical value of void space, it seems to closely match the visible void areas within the channels.

To increase the volume fraction of aramid fibers, two different approaches were attempted. Detailed procedures are listed in Appendix A.

1. The first approach was to embed 1 layer of closely packed aramid threads flat into a 0.005 in. (0.127 mm) deep channel that is 0.125 in. (3.175 mm) wide. During the sample preparation, tape tearing around the channel was experienced. It is believed that due to the aramid pushing out the tape and the bonding occurring with the metal outside of the channel, the tape shears. To minimize the tape shearing, welding initially at a lower amplitude and then rewelding the same joint at progressively higher amplitudes, minimizes the tape tearing.

2. The second approach is to embed a twisted thread bundle into a 0.020 in. (0.508 mm) deep channel 0.0625 in. (1.5875 mm) wide and is shown in Figure 2.16. It is believed that twisting of the threads helps to prevent pull out of the fibers due to the frictional contact with different threads against the channel throughout the length of the channel.

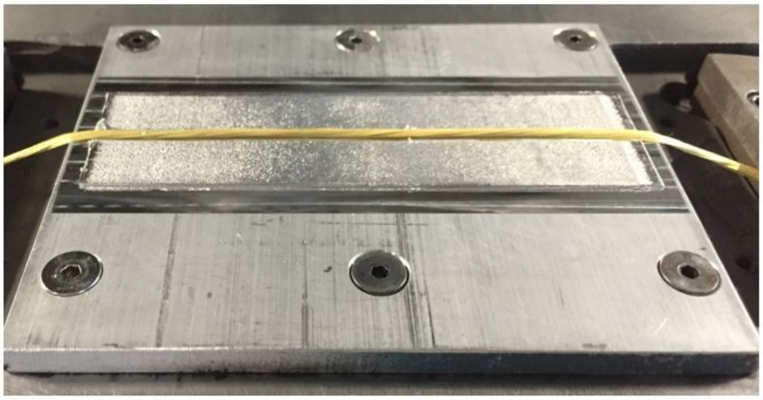

Figure 2.16: Twisted (approx. 3 twists/inch) aramid fiber bundle before embedding in aluminum.

Creating channels for fibers was effective, with approach two being more effective. It is possible to get a larger volume fraction of fibers within the channel using approach two. Regardless, both fibers did not adhere to the channels as well as anticipated, therefore not absorbing an appreciable amount of load during testing. This could be a desirable effect if one were attempting to design a structure that was still able to bear load after failure, thereby increasing the toughness of the structure. Tensile testing results are presented in Section 2.5.

2.3.4 UAM Fiber Reinforcement with UHMWPE

During pilot welds with Dyneema®, or Ultra High Molecular Weight Polyethylene (UHMWPE), it was found that the UHMWPE did not behave in the same manner as the aramid when attempting to embed 4 tows into a channel using the same procedures used during the welding of Aramid into a channel. Aramid is a thermoset polymer; UHMWPE is a thermoplastic with a melting temperature near 155°C. During the UAM process, UHMWPE that comes in contact with the tape seems to melt or ultrasonically weld to itself. Additionally, the UHMWPE fibers tend to spread out giving it a cotton-like appearance. When trying to embed enough UHMWPE to allow for significant compression inside the channel, the tape tears at the channel exposing the UHMWPE. The tape above the fiber tearing was also observed when attempting to weld over aramid within a channel and is shown in Figure 2.13 (b). To help eliminate the tape tearing, an iterative approach to determine the minimum channel depth that would allow for fiber embedment was used. The channel depth that did not result in tape tearing at the channel was too large to secure the UHMWPE within the channel using a compressive fit, allowing the UHMWPE to be pulled from the samples with minimal force. Figure 2.17 shows the UHMWPE fibers within the channel.

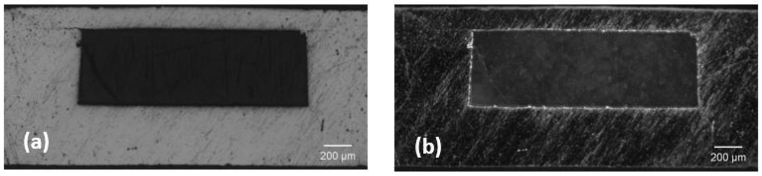

Figure 2.17: Bright and dark field images, (a) and (b) respectively, of UHMWPE within channel of 5052/6061-H18 MMC.

The more fiber that is compressed within the channel, the more strength is possible for the composite as the fiber is able to bear more load and slip less within the channel under tension. However, the greater the compressive force, the greater the reaction force applied by the fiber on the channel. It is postulated that this, in combination with potential nuggeting of the tape that covers the channel onto the horn, can lead to tape tearing as shown in Figure 2.13 (b).

Using cured epoxy (aluminum filled epoxy cures within 48 hours at room temperature and within 2 hours at 200°F) to bind the fibers into the channel as an intermediate step in the welding process was considered. However, with the welding/sample geometry design constraint, 0.035 in. (0.9 mm) thick aluminum sheet used a base material) the most effective way of embedding fibers was determined to be welding one layer onto the baseplate; cutting a channel for the fiber; laying the fiber in the channel and manually tensioning; and welding one layer on top of the channel, securing the fiber within the channel. Welding on the base plate causes severe deformation in the base plate making it nearly impossible to re-secure the base plate to the vacuum chuck once it has been removed. Because of this, all processes that must occur to effectively embed fibers must occur in situ and not be part of an intermediate process that takes place off of the vacuum chuck.

In an attempt to better secure the UHMWPE within the channel after welding, the UHMWPE fiber bundle was enrobed with aluminum filled epoxy and placed within the channel under mild tension. The ultrasonic welding process caused the wet epoxy to travel from the centered 0.0625 in. (1.5875 mm) channel throughout the weld interface and even up and onto the horn. As a result, the tape did not stick at all to the baseplate and great care was taken to remove all remaining epoxy from the horn. The process was attempted again using far less epoxy applied with similar results.

2.3.5 UAM Fiber Reinforcement with PBO

Another type of polymer, Zylon®, which has an increased strength and stiffness compared to UHMWPE was also welded in a channel using UAM. Zylon®, or Polybenzobisoxazole (PBO), is a thermoset polymer manufactured by Toyobo with properties listed in Table 2.1. Unlike UHMWPE, Zylon does not melt, but decomposes at 650°C.

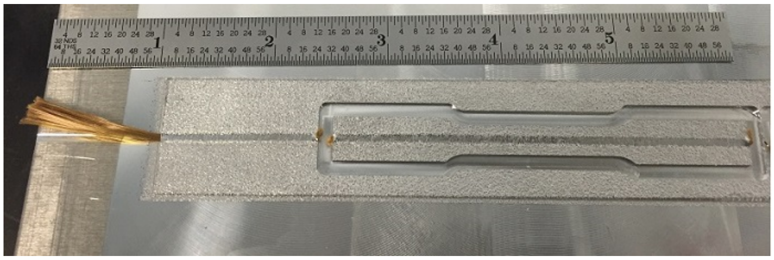

Figure 2.18: PBO embedded in 5052 and Al 6061-H18 matrix.

PBO, similar to aramid, was able to be welded (Figure 2.18) into a channel, using seven twisted (approx 3 twists/inch) tows, with enough compression around the fiber to keep it in place post weld. This is significant because it shows that there is not a fundamental difference between the PBO tows and the aramid thread bundles, with both fiber types being thermoset polymers. UHMWPE has a very low friction coefficient of 0.05-0.07 whereas PBO has a frictional coefficient of 0.18 [29], which could contribute to the difficulty with effectively constraining the UHMWPE within the channel whereas there was no difficulty with the Zylon. The sample geometry is shown in Figure 2.18. Figure 2.19 shows the PBO fibers within the channel.

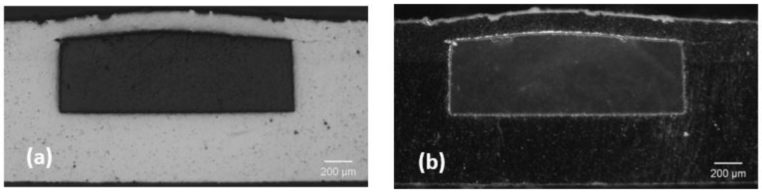

Figure 2.19: Bright and dark field images, (a) and (b) respectively, of PBO within channel of 5052/6061-H18 MMC.

2.3.6 UAM Fiber Reinforcement with SiC

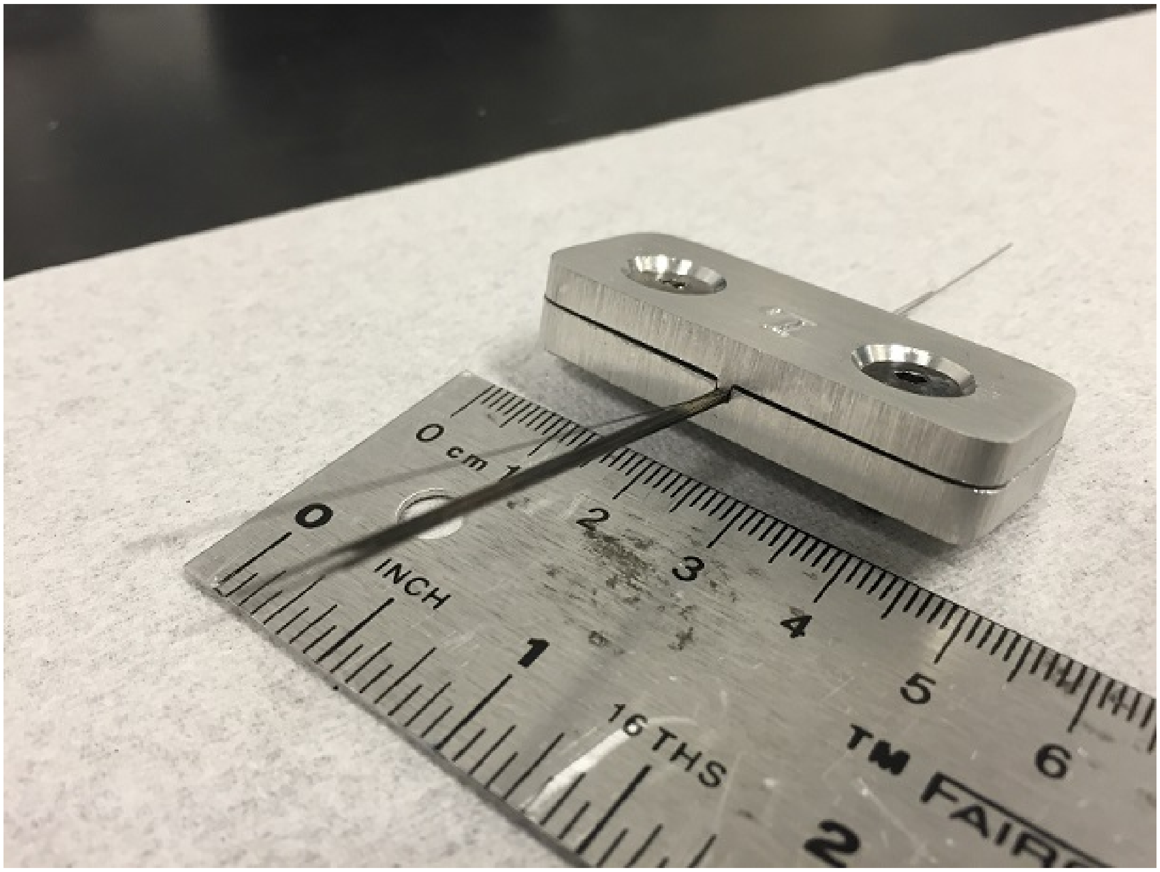

Figure 2.20: Custom tool to clamp SiC in place during welding allowing the SiC fiber bundle to be pulled taught.

Using the same sample geometry as the PBO samples, (45) SiC fibers were able to be welded into a channel. Although very brittle, the fibers were able to be clamped into place using a custom made tool, shown in Figure 2.20, that clamps the fibers in a rectangular-shaped channel so that they can be pulled taught in order to stay in place during welding. The tool is made of aluminum and has a 0.0625 in. (1.5875 mm) tung and groove that holds the fibers in place, without applying a damaging shear force. A slight twist was applied to the fibers, 1.5 revolutions per in. (0.6 revolutions per cm), to keep the fibers from pulling out of the center of the channel. Without the twist, when pulling the fibers taught, the fibers in the center of the channel pull free.

Figure 2.21: SiC embedded dog-bone with rough edges due to dulling of end-mill as part of the machining process.

Similar to the challenges associated with machining alumina-containing MetPreg samples in discussed earlier, the SiC embedded in the channel caused the end-mills used to dull very quickly. Each end-mill was only capable of cutting two samples before it was too dull to effectively cut (Figure 2.21). Even though Zylon is stronger and of similar ductility, there was no significant dulling of tooling while machining Zylon samples. Figure 2.22 shows the SiC fibers within the channel.

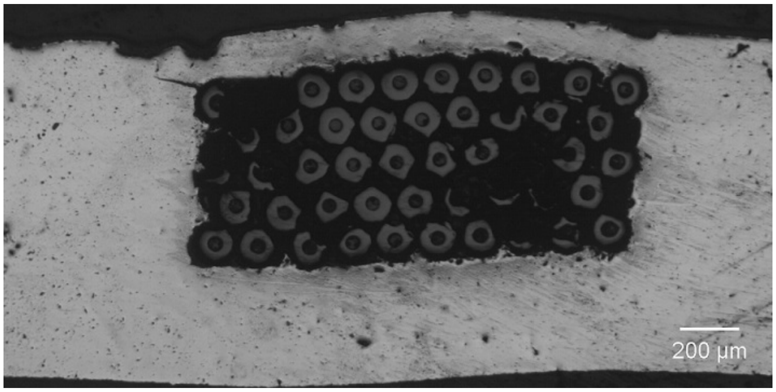

Figure 2.22: Micrograph of SiC fiber bundle within channel of 5052/ 6061-H18 MMC.

2.4 UAM Added Material as Part of the Reinforcement

2.4.1 Al 6061-H18 Tape to Al 5052-O Sheet

MetPreg, aramid, and the HSS wires were welded/placed in channels in between welded Al 6061-H18 tapes. The UHMWPE, PBO and SiC wires were all used along with 6061-H18 to reinforce 0.035 in. (0.9 mm) thick Al 5052-O sheet, further referred to as 5052, as the base material. The base material was integrated into the final part dimensions. This section discusses the complexities associated with welding on thin base plates, and dissimilar materials. The goal of the reinforcement was to achieve at least a 10% volume fraction (VF) of reinforcing fiber and at least 20% VF UAM welded material. The 20% VF is determined by the amount of tape laid, divided by the total height of tape and baseplate. The 10% VF is determined by dividing the cross-sectional area of the channel by the total cross-sectional area of the tensile specimen, both tape and baseplate. These areas are illustrated in Figure 2.23 and as shown have 25% VF added tape and 13% VF fiber material assuming the fiber material fully fills the channel. The reinforcing fiber was be embedded into 5052 using UAM welded Al 6061-H18. With the geometry described in Figure 2.23, after the channel has been cut and the is fiber is embedded, the total VF of fiber is 13%; the total VF of tape is 22%; and the total VF of 5052 is 64%. Modified rule of mixture calculations are demonstrated in Chapter 1.

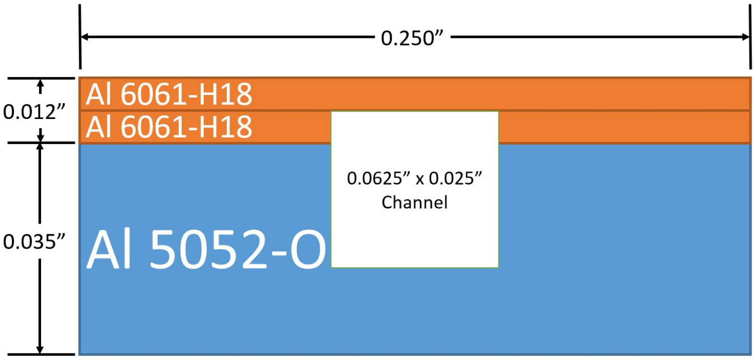

Figure 2.23: Tensile specimen sample design requirements with example channel graphic.

To better understand the impact of the welding process and to predict the 5052 and Al 6061-H18 composite behavior, individual material properties for 5052 and 6061-H18 were obtained experimentally using a 25 kN Interlaken load frame in concert with a Correlated Solutions Digital Image Correlation (DIC) system. Results for the tensile tests are shown with stress-strain plots in Figures 2.24 and 2.25 for 5052 and Al 6061-H18 respectively and are tabulated in Table 2.4, including Al 5052 yield strength, ultimate tensile strength, elongation at failure, as well as specific yield and ultimate strengths. The 5052 material property data was obtained from a sub-size tensile specimen (per ASTM E8) [6] cut from 0.035 in. (0.9 mm) sheet. The UAM welded Al 6061-H18 material property data was obtained by testing sub-size tensile specimens constructed by welding (8) layers of 0.006 in. (0.1524 mm) tape using procedures described in Appendix A for constructing aluminum only samples.

Table 2.4: Al 5052-O and Al 6061-H18 material properties. Values for material properties in tension are determined from Figures 2.24 and 2.25 and are consistent with published values for Al 5052-O. No published data is available for Al 6061-H18.

	σ_Y **[MPa]**	σ_{UTS} **[MPa]**	ϵ_f **[%]**	$\sigma_{Y_{spec}}$ **[MPa-m^3/kg]**	$\sigma_{UTS_{spec}}$ **[MPa-m^3/kg]**
Al 5052-O Sheet	95	200	23.5	0.035	0.074
UAM Welded Al 6061-H18 Tapes	195	206	2.5	0.072	0.076

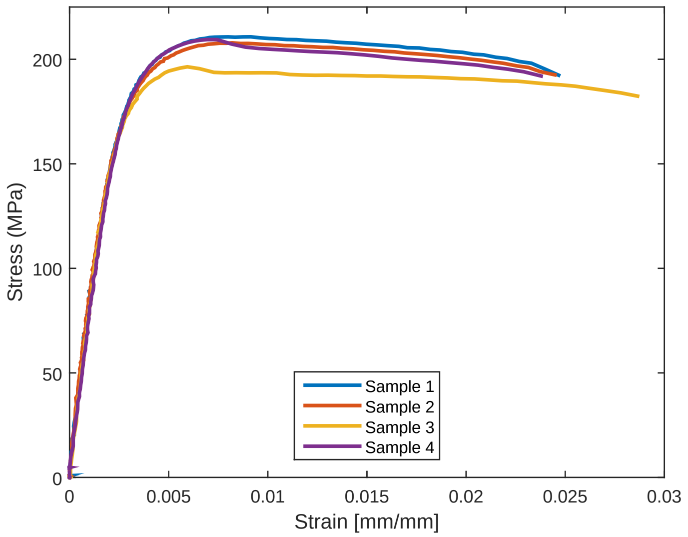

Figure 2.24: UAM welded Al 6061-H18 tapes stress-strain plot from sub-size dog-bone tensile specimens.

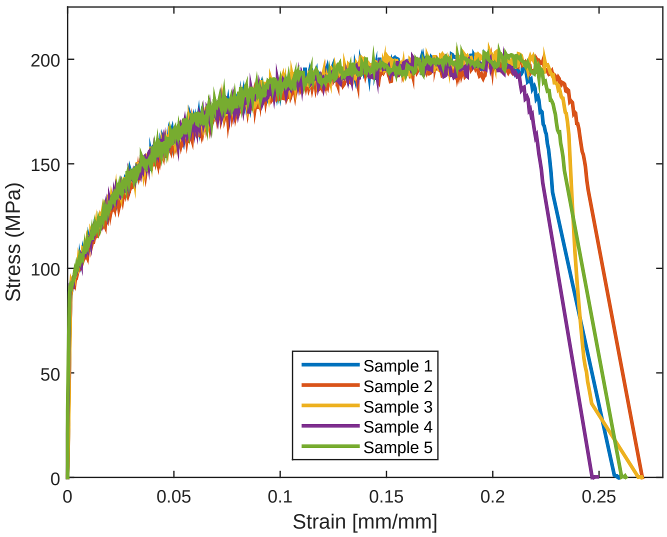

Figure 2.25: Al 5052-O stress-strain plot from sub-size dog-bone tensile specimens. Noise in the data is believed to be due to electromagnetic interference.

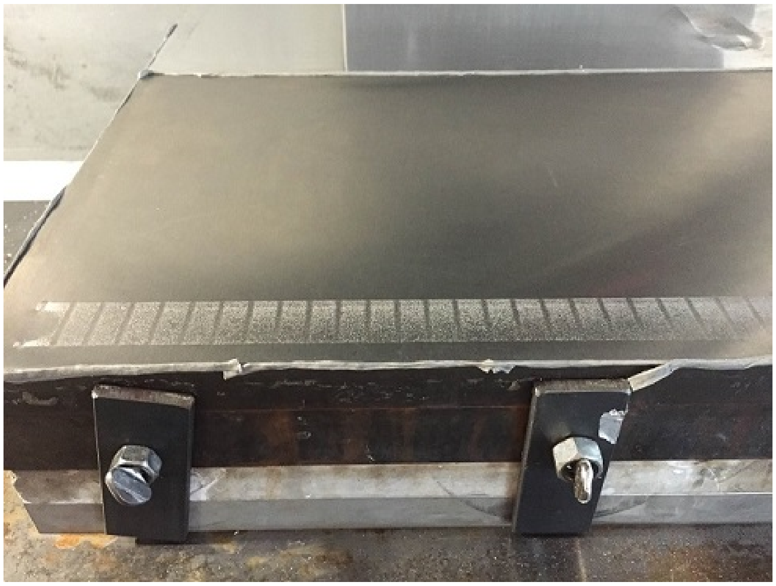

Figure 2.26: OSU vacuum chuck pattern revealed through welder pass.

Pilot welds were attempted by laying the 5052 sheet directly on top of the OSU vacuum chuck. The material was thin enough to push through the slits in the OSU vacuum chuck during a texturing pass due to the 4000 N down force applied by the welder, meaning, the vacuum chuck was not supporting the base plate at those points. The result is shown in Figure 2.26. This introduced the need for an anvil that would provide support throughout the welding process while still holding the sheet in place. A vacuum chuck adapter plate (Figure 2.27) was used to weld 2 layers of Al 6061-H18 tape, 1 in. (25.4 mm) wide x 0.006 in. (0.1524 mm) thick, to a 0.035 in. (0.889) thick 5052 sheet. Welds were made using OSU's Fabrisonic Sonic Layer 4000 UAM System.

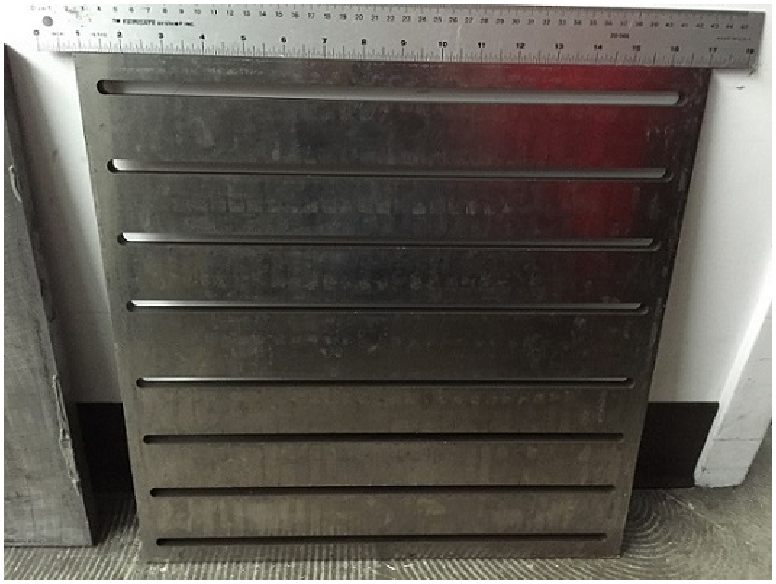

Figure 2.27: OSU vacuum chuck adapter plate.

Initially, welding Al 6061-H18 to a 0.035 in. 5052 base plate was attempted using weld parameters for typically used for welding Al 6061-H18 to thick (∼0.5 in) base plates. Weld parameters are shown in Table 2.5. A representative cross section is shown in Figure 2.28. Although the Al 6061-H18 tapes stuck to the 5052, the micrograph shows many voids and clear lines between tapes and between the baseplate and the tape. This was not expected. To remedy the poor weld quality, a series of pilot welds were made using different parameters to determine what parameters could produce a quality weld. Through many trials, the refined parameter set used for the construction was developed (Table 2.5). It was found that not only is a slower weld required, but the levelness of the base plate to the horn has a strong correlation with the quality of the weld. To help combat some of the levelness complications, a higher normal force was used for the welds, deforming the sheet to be more level with the horn. Additionally, the successful welds (Figure 2.29) required a surface machined parallel to the surface of the horn. It is believed that the thin plate is more susceptible to the effects of the precise levelness of the vacuum chuck than other geometries that have been previously attempted by the OSU UAM lab.

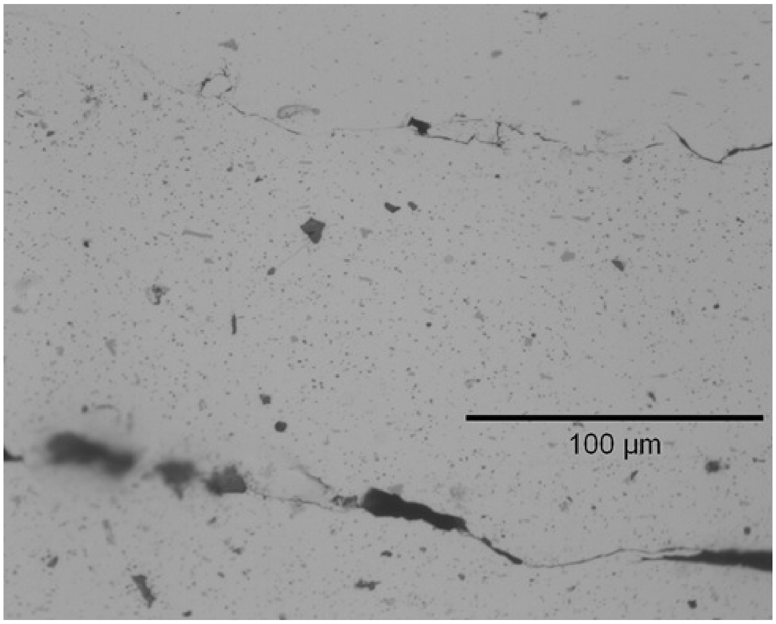

Figure 2.28: Initial weld attempt using the welding parameters listed in Table 2.5, showing voids at weld interfaces, attempting to weld Al-6061-H18 tapes to 5052.

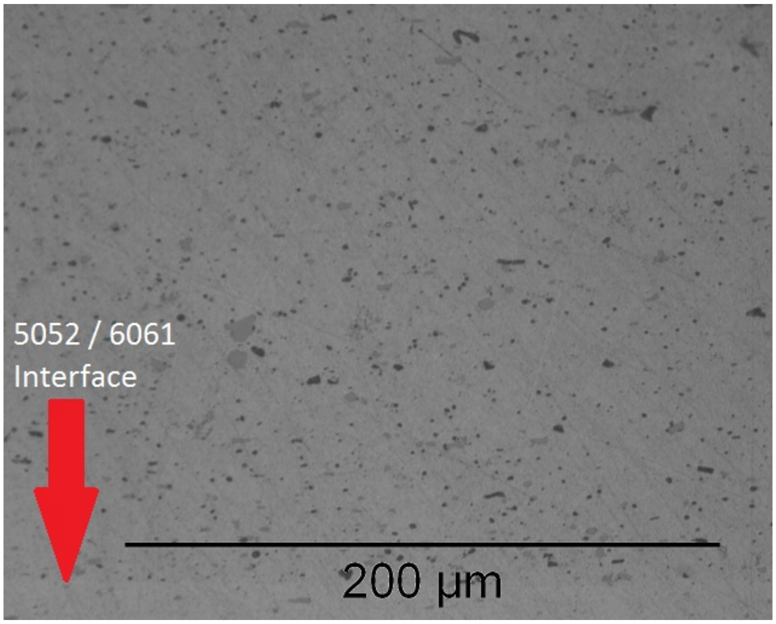

Figure 2.29: Weld of two layers of Al 6061-H18 on Al 5052-O using refined weld parameters listed in Table 2.5. No voids are evident. Black spots are precipitates commonly found in Al-6061.

Table 2.5: Weld parameters used for Al 6061-H18 to 5052.

	Weld Force (kN)	**Weld Amplitude** (μm)	**Weld Speed** (mm/s)
Initial Parameters	4	35	85
Refined Parameters	5	22	21

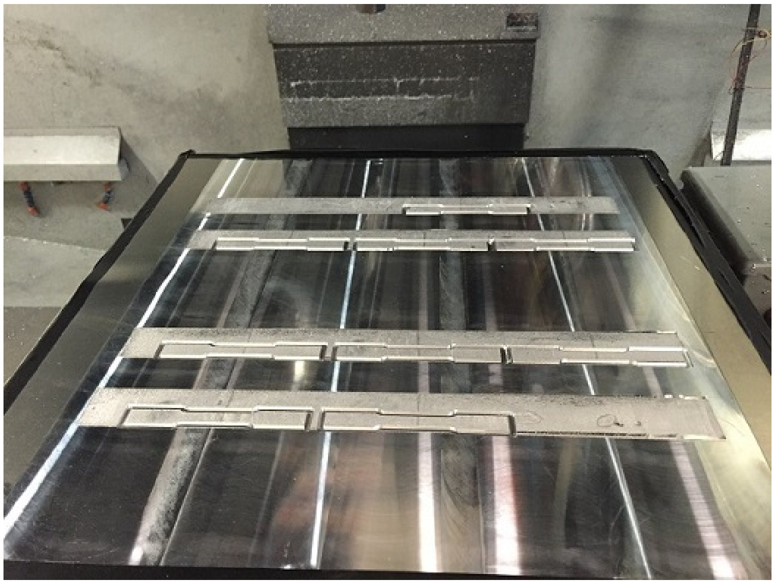

Figure 2.30: Dog-bone sample cutouts from 5052/6061-H18 composites.

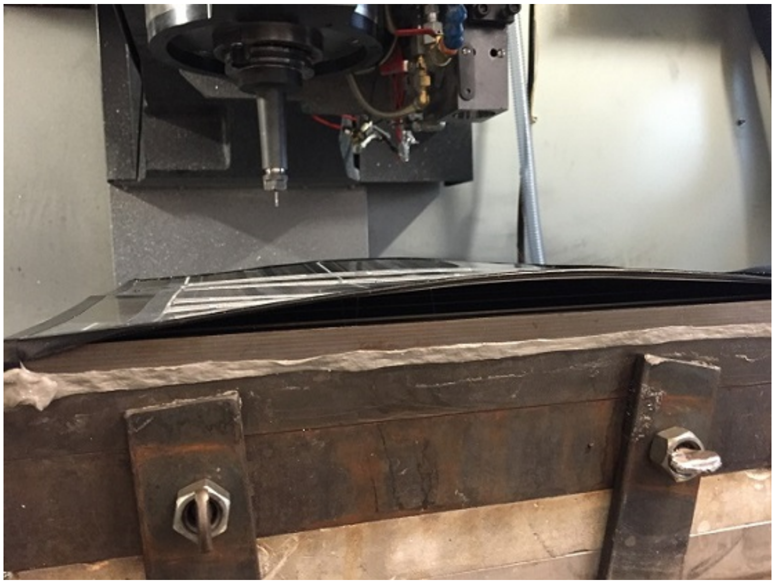

Figure 2.31: Bowed sheet after dog-bone sample cutouts from 5052/6061-H18 composites.

Using the refined weld parameters shown in Table 2.5, sub-sized dog-bone samples were constructed according to ASTM E8 [6]. Ten samples were created to compare both pre and post heat treated mechanical properties. Additionally, cross-sections were obtained from each to observe the welded interface as well as qualitatively compare pre and post heat treated welds. The sheet with tensile samples cut out is shown in Figure 2.30. After the samples were cut from the base plate, the vacuum was released which no longer constrained the base plate to the chuck. This allowed significant bowing of the base plate, Figure 2.31, which is believed to be due to residual stress as a result of the welding process. When a vacuum is applied, little to no distortion in the base plate is visible.

2.5 Tensile Testing Results

2.5.1 Al 6061-H18 with aramid thread bundle composite

For the purpose of this research, Digital Image Correlation was first used with the aramid samples during tensile testing to failure. This allowed for very high strain resolution and to observe the type, location and evolution of failure. The set of images shown in Figure 2.32 shows the evolution of failure from left to right. The bottom of the sample is plastically strained, but does not fail. The top of the sample is where failure occurs. The rightmost image in Figure 2.32 shows the aramid reinforcement in the center of the failed region, which continued to bear load after failure.

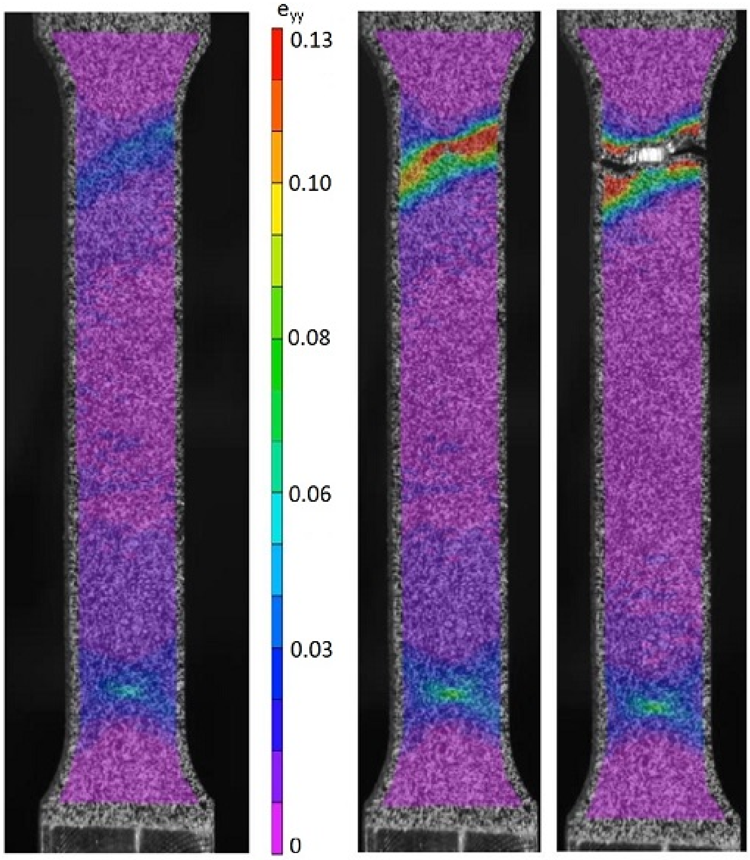

Figure 2.32: Failure evolution, left to right, of UAM created aluminum matrix, aramid reinforced composite with strain mapping using DIC.

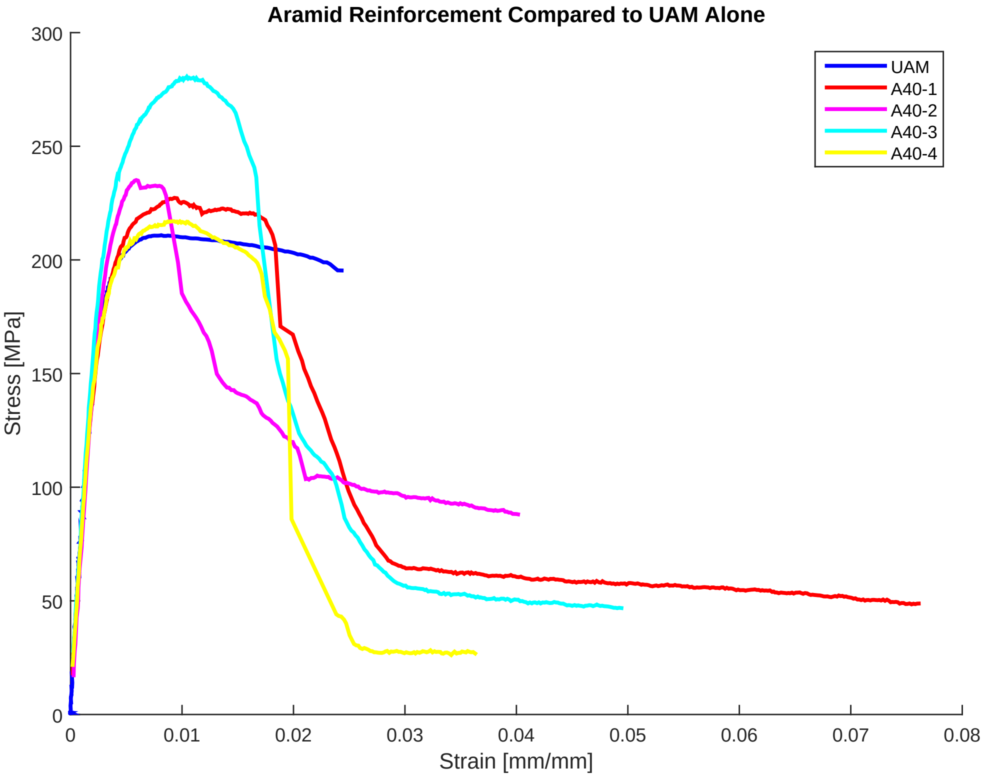

Figure 2.33: Tensile results of UAM created aramid reinforced aluminum metal matrix composites.

Figure 2.33 shows the tensile results for UAM created aramid reinforced aluminum Metal Matrix Composites (MMCs). All of the samples failed with a higher overall stress, but with lower overall strain. The variability of the failure could be due to differences in the frictional contact between the aluminum channel and the aramid thread bundle. Possible causes are manufacturing inconsistencies and/or testing inconsistencies such as varying grip force. All of the aramid samples continued to bear load after failure, increasing the overall toughness of the composite.

2.5.2 Al 6061-H18 with Embedded HSS Music Wires

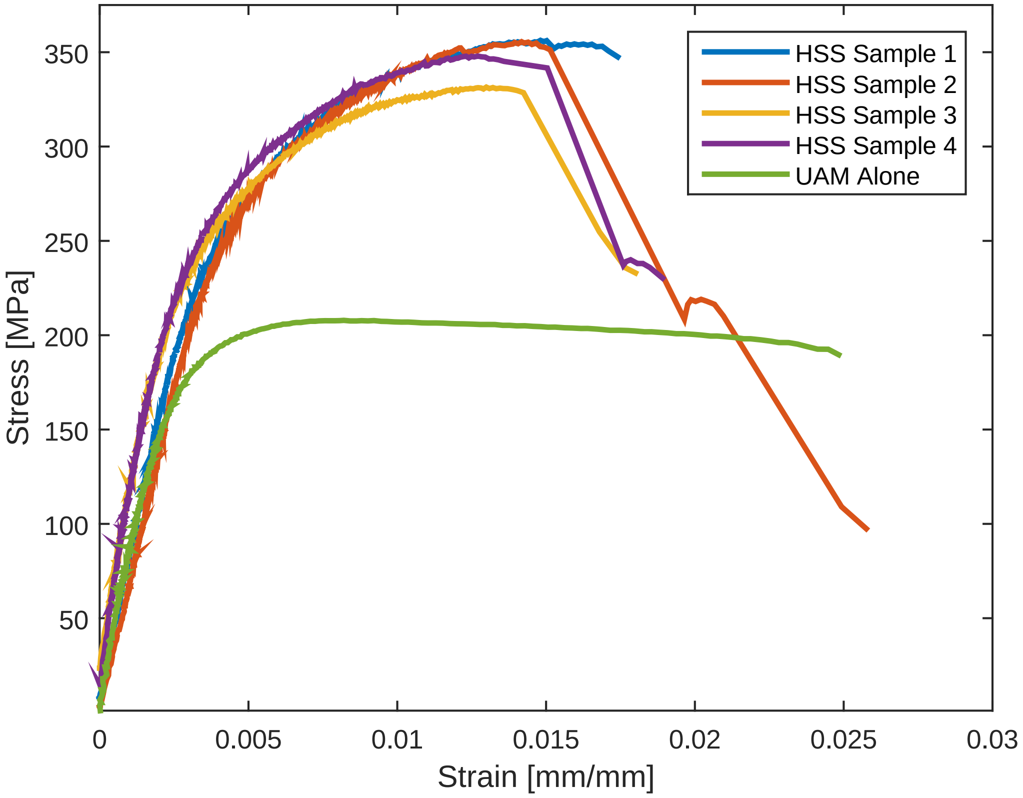

Figure 2.34: Tensile results of UAM created 6% VF HSS music wire reinforced aluminum MMCs.

Figure 2.34 shows the tensile results for the UAM created HSS music wire reinforced aluminum MMCs compared to UAM alone. The step decreases observed in samples 1, 2, and 4 are due to HSS wires breaking within the matrix. Their breaking was accompanied with a high pitched sound, similar to plucking a guitar string. As can be seen, the all of the samples failed at a greater overall UTS than the UAM alone sample, and more consistently than the aramid reinforced samples.

2.5.3 5052 Al 6061-H18 composite (matrix material)

Using a 25 kN Interlaken load frame in concert with a Correlated Solutions DIC system, tensile tests were performed on 5052/Al 6061-H18 composites. Graphs of the engineering stress-strain plots are shown in Figures 2.35 and 2.36.

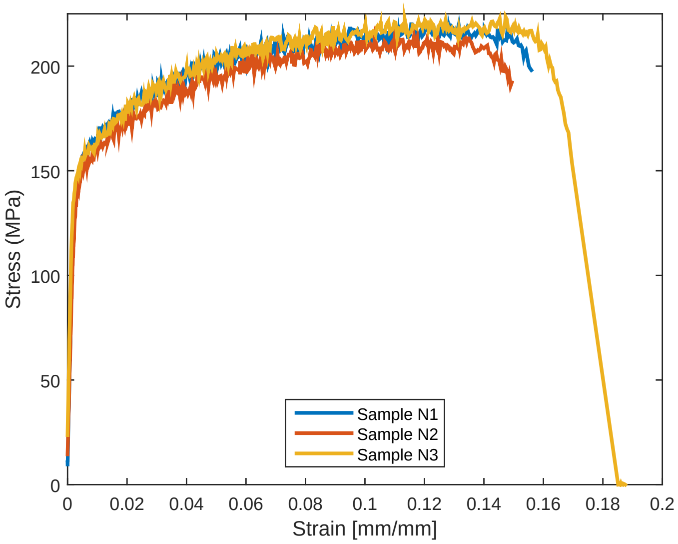

Figure 2.35: UAM welder induced work hardening of 5052 base plate tensile stress behavior.

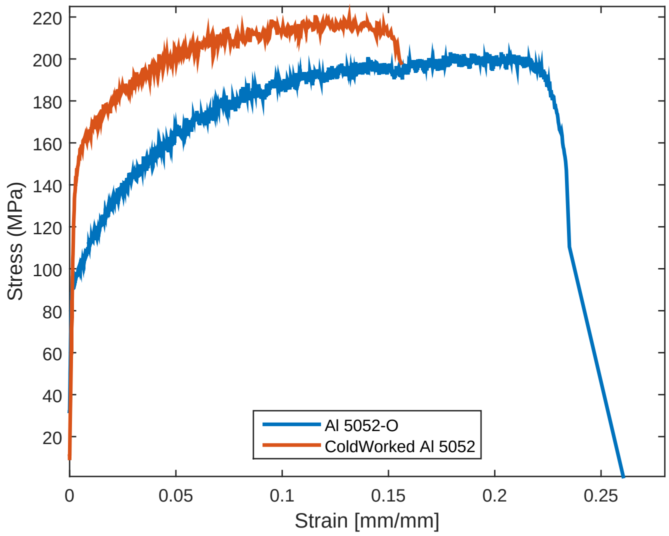

Figure 2.36: UAM welder-induced work hardening of 5052 base plate tensile stress representative sample behavior compared with a representative Al 5052-O sample.

What was initially expected was brittle behavior of the Al 6061-H18 causing a step decrease in stress, and the 5052 to continue to deform at a lower stress before failing at a strain near that of the 5052 alone. What occurred was a series of small cracks propagating through the Al 6061-H18 (discussed in Section 2.5.6) and, the 5052 was work hardened as a result of the welding process, allowing the composite to fail at a higher strength and lower strain. The series of small cracks were not observed using the DIC system because all samples were observed on the 5052 side of the composite due to the original assumption that the Al 6061-H18 side would experience brittle fracture near 3% elongation.

To observe the work hardening effects of the UAM process on the 5052, tensile samples were created using the same welding parameters and number of layers as shown above, but with the Al 6061-H18 layers being machined off before the dogbones were cut out, leaving only the 5052, making the samples thinner than those that had been tested with two Al 6061 H-18 welded layers. Tensile test results are shown in Figure 2.35. Figure 2.36 as well as Table 2.6 show a comparison between the as received Al 5052-O and the UAM cold rolled Al 5052. In addition to the 5052-O and cold rolled properties, H12 properties are included to demonstrate the change that is trending toward published strain hardened 5052 properties. Regarding "H12", the "H1" means strain-hardened only, and the second digit, in this case "2", is the degree to which the material was hardened, with "9" being the max. The Al 5052-O, after work hardening, exhibited increased ultimate and yield strength and decreased ductility, with properties lying between that of the "O" temper and "H12" temper.

Table 2.6: Al 5052 properties with different tempers.

5052	**UTS** [MPa]	**Yield Strength** [MPa]	**Elastic Modulus** [GPa]	**Elongation to Fai** [%]
O	203	95	70	26
UAM Work Hardened	220	150	70	16
H12[30]	230	180	70	11

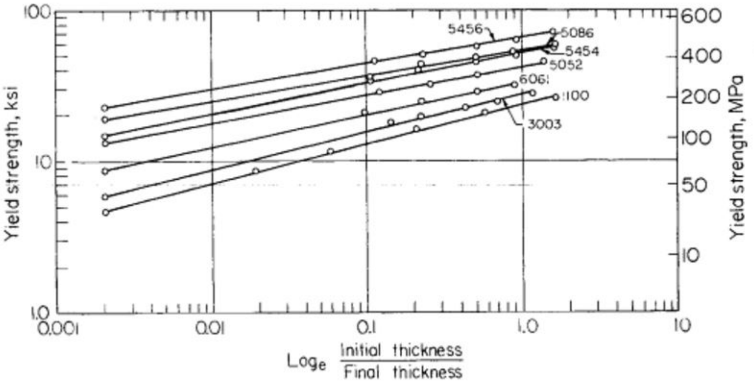

Figure 2.37: Strain-hardening curve for annealed aluminum alloys plotted according to the relation $\sigma = k\epsilon^n$, and substituting yield strength for true stress [31].

At room temperature, 5052-O yield strength is expected to increase from approximately 100 MPa (no strain condition) to the observed 155 MPa with approximately 1.5% change in thickness as shown in Figure 2.37 [31] due to work hardening. The 1.5% change would be equivalent to about a 0.0005 in. (0.0127 mm) change in thickness of the baseplate which cannot be easily observed during testing due to the small magnitude. Strain-hardening explains the rise in yield strength, in conjunction with the Al 6061-H18 bonding to the 5052.

2.5.4 UAM Fiber Reinforced Tensile Results

The UHMWPE, PBO and SiC fiber embedded dog-bone samples were tested using the same procedures outlined in Section 2.5.3. Figures 2.38, 2.40 and 2.41 show individual tensile results. Figure 2.42 shows all of the tensile results of samples containing embedded fibers and Tables 2.7 and 2.8 show actual and density normalized properties of tensile specimens. These composites were created with a different matrix than the aramid and HSS samples, which were created with Al 6061-H18 alone, while the UHMWPE, SiC and PBO samples were created with the Al 5052-O/Al 6061-H18 matrix discussed in Section 2.5.3.

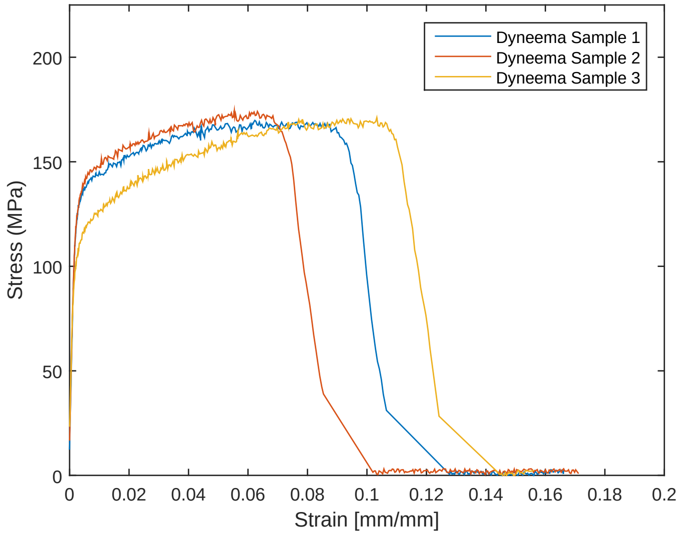

Figure 2.38: Tensile results with embedded UHMWPE.

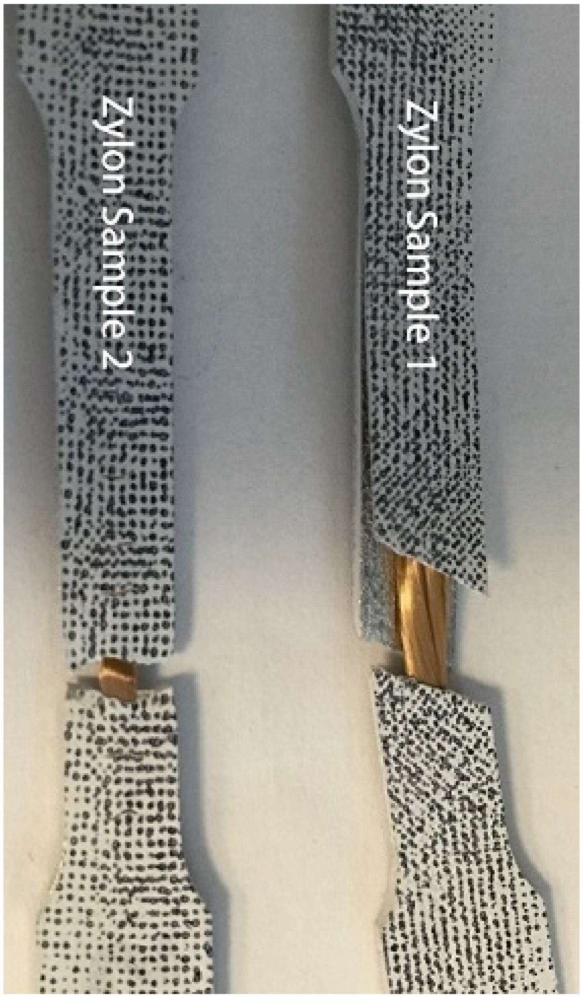

Figure 2.39: PBO Sample 1 and 2, post testing.

PBO Sample 1, shown in Figure 2.39, lost strain data as a result of failure and debonding of the Al-6061-H18 welded layer. Once the debonding occurred, the DIC could no longer track the strain, although the sample failed beyond the strain shown in Figure 2.40.

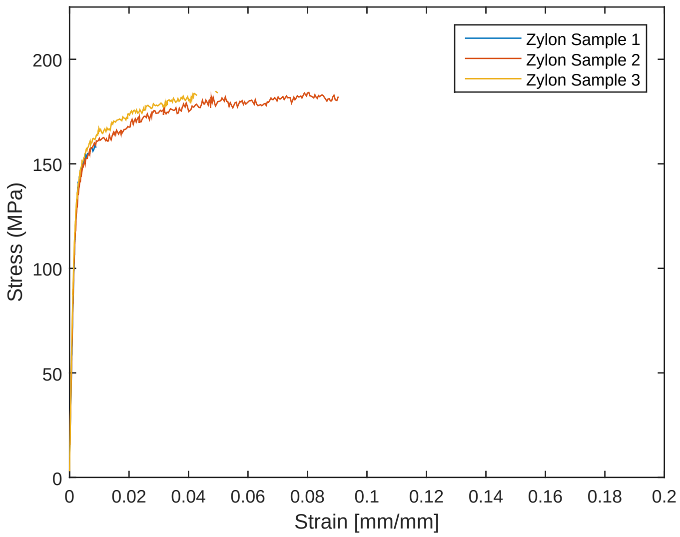

Figure 2.40: Tensile results with embedded PBO.

SiC sample 1's matrix failed earlier than the other samples, but the SiC still was able to bear some load. After the DIC system lost track of the sample, a dotted line was used to represent the actual stress but assumed strain values.

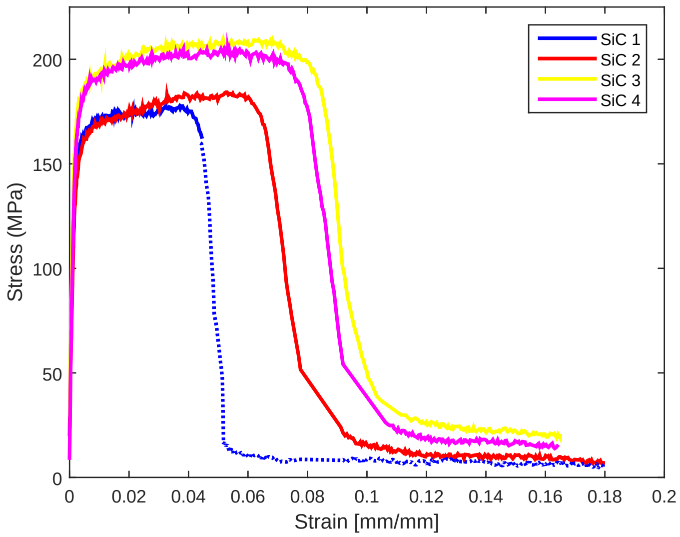

Figure 2.41: Tensile results with embedded SiC. Dotted line represents assumed strain behavior.

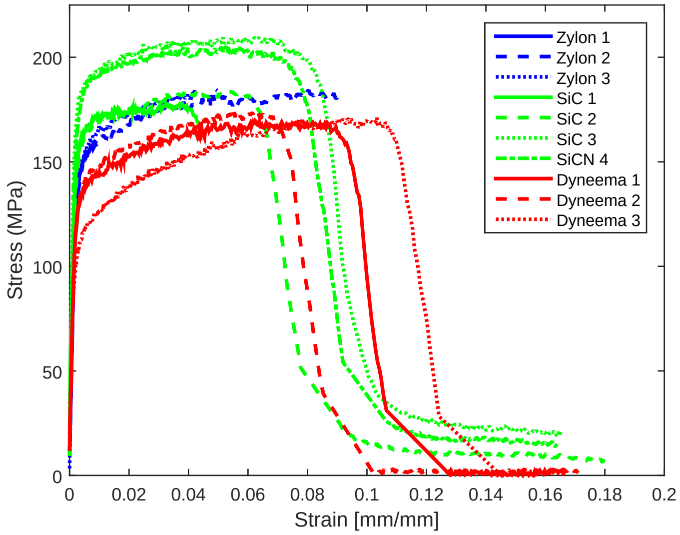

Figure 2.42: Tensile results for Dyneema, Zylon and SiC fibers for comparison.

Table 2.7: UAM/fiber reinforced tensile results

	Dyneema			**SiC**				**Zylon**		
Sample Number	**1**	**2**	**3**	**1**	**2**	**3**	**4**	**1**	**2**	**3**
Modulus [GPa]	60	59	56	72	65	85	83	58	63	69
Yield Stress [MPa]	133	136	111	161	156	183	179	150	147	150
UTS [MPa]	170	174	171	178	184	209	205	159	184	187

Based on both the rule of mixtures calculations as well as the difficulties associated with embedding the SiC while having it remain within the channel and pulled taught prior to welding, it was anticipated that the Zylon embedded samples would outperform the SiC embedded samples. It is believed that the reason that the SiC

Table 2.8: UAM/fiber reinforced tensile results (density normalized). Data taken from highest performing sample.

Reinforcement	**Modulus [GPa-m^3/kg]**	**Yield Stress [MPa-m^3/kg]**	**UTS [MPa-m^3/kg]**
SiC	0.031	0.068	0.077
Zylon	0.029	0.058	0.072
Dyneema	0.028	0.054	0.070

outperformed the Zylon is due to the clamping force of the grips during tensile testing. The Zylon, as a fiber bundle, is more compliant than the SiC fiber bundle. This would allow the grips to better secure the SiC in place during tensile testing. The results of the fiber pull testing are described in Section 2.6.2.

2.5.5 Experimental determination of residual stress

To help determine or possibly quantify the residual stress state between 6061 H18-on-5052 and the 5052 baseplate, four different samples were constructed:

- (a) Control, only machined
- (b) Rolled over the samples three times using the same force as used during welding
- (c) Welded two tapes using same parameters used to create all tensile samples
- (d) Welded two tapes using same parameters used to create all tensile samples, then machined off welded layers leaving only 5052 baseplate.

After the samples were cut from the baseplate, they were all painted and speckled on the bottom of the 5052 baseplate layer so that the DIC system could be used to map the surface. To serve as a control, for comparison, one sample was only subjected to surface machining (Fig. 2.43).

Three of the samples were created on the same baseplate, (a), (b) and (d).

For the control sample (a), the plate was placed on the vacuum chuck adapter plate and machined flat. The plate was then removed from the vacuum chuck, rotated ninety degrees and placed back on the vacuum chuck. When the plate was originally placed on the vacuum chuck it was relatively flat. After machining the plate flat and removing from the chuck, the plate was bowed concave up perpendicular to the machining direction. This shows that machining operations alone exude either some form of residual stress or plastic deformation to the baseplate.

After machining flat again, sample (a) was cut from the baseplate.

In order to differentiate cold rolling effects from welding effects, sample (b) was created using the same forces and welding amplitudes used during the creation of the tensile samples. However, due to concerns for nuggeting, a 200 in/min (85 mm/s) weld speed was used, as opposed to the 50 in/min (21.2 mm/s) weld speed used to create the welded samples. To further clarify, no tape was laid onto the cold rolled sample.

Samples (c) and (d) were created using the same parameters used for tensile test and identically to each other, with the exception that post weld, sample (d) laid tape was machined off.

Figures 2.43, 2.44, 2.45, and 2.46 show the surface maps with the 5052 facing up and the welded side, if applicable, facing down, for samples (a), (b), (c) and (d), respectively. To clarify, after the samples are cut out of a plate that was on the vacuum chuck, they are flipped over so that their underside can be painted and speckled.

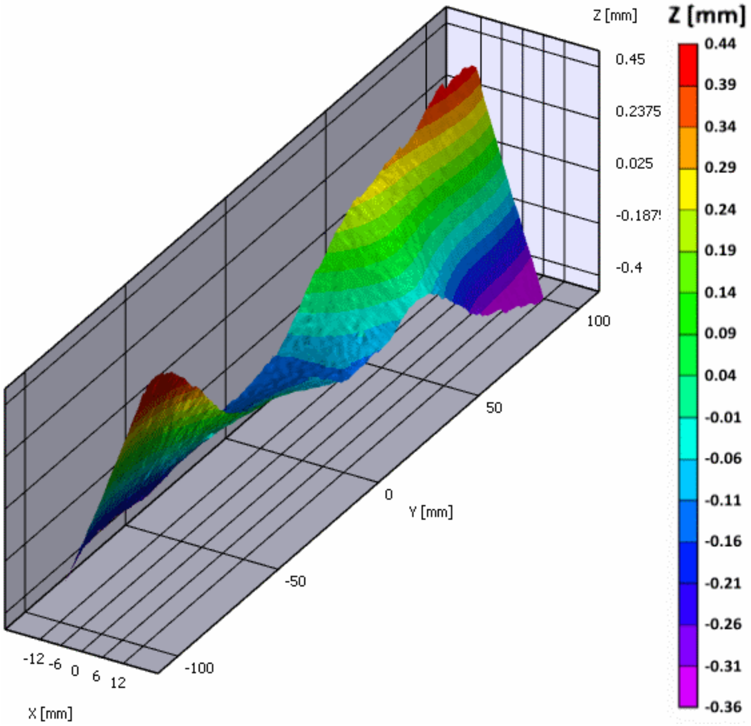

Figure 2.43: DIC surface map of sample (a), Control, only machined, for residual stress determination.

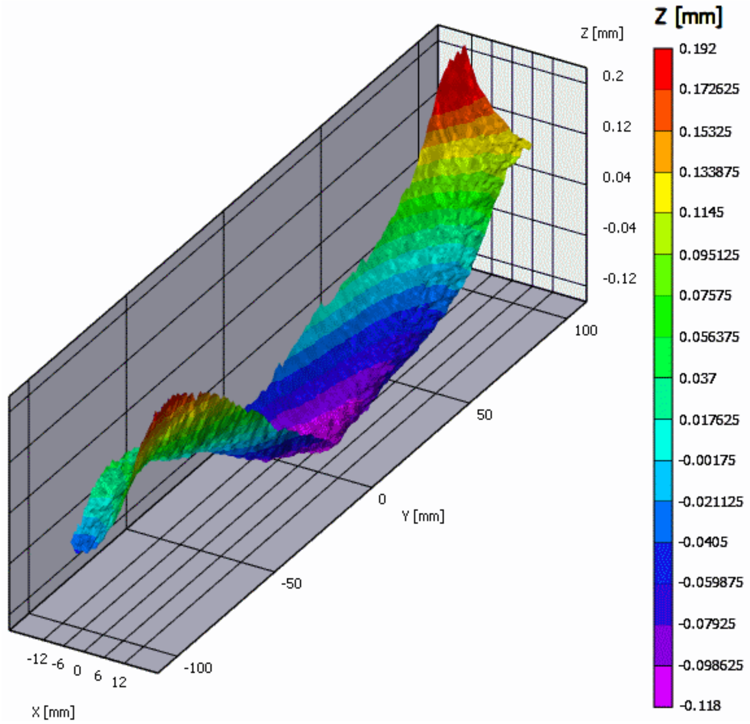

Figure 2.44: DIC surface map of sample (b), Rolled over the samples three times using same force as used during welding.

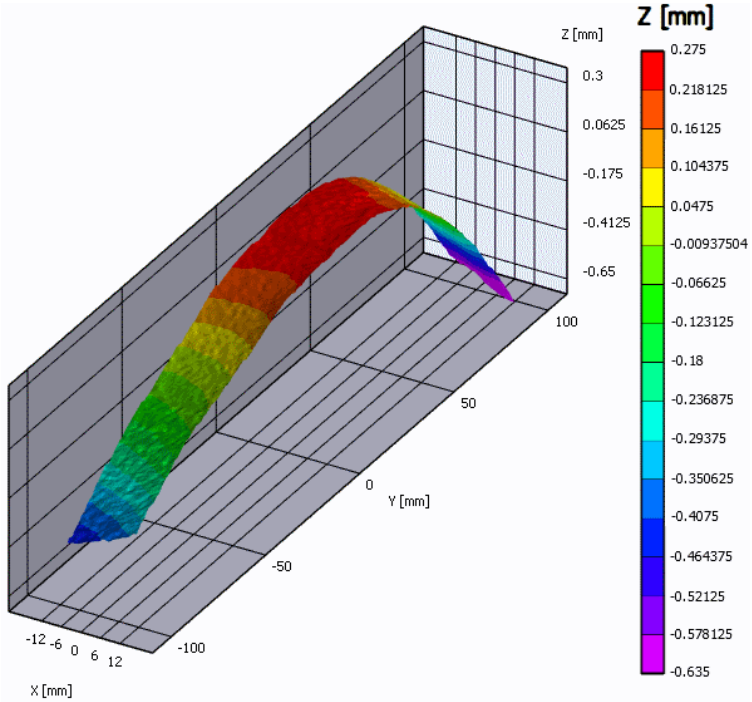

Figure 2.45: DIC surface map of sample (c), Welded two tapes using same parameters used to create all tensile samples.

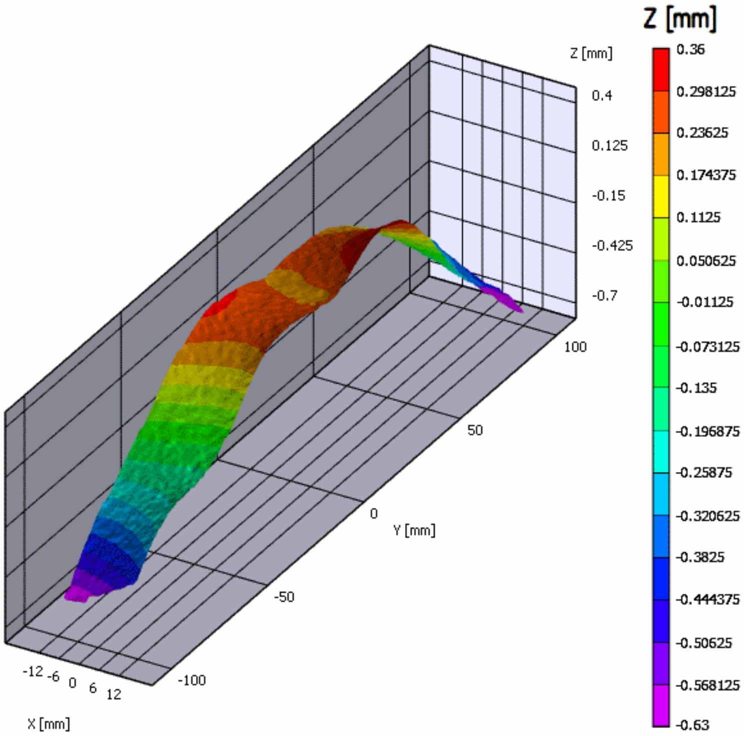

Figure 2.46: DIC surface map of sample (d), Welded two tapes using same parameters used to create all tensile samples, then machined off welded layers leaving only 5052 baseplate.

Samples (a) and (b) both exhibit a twisted shape consistent with the shapes observed as a result of the cutting forces. The magnitude of the twist for sample (b) is less, however, due to the cold rolling effects of the welder. Samples (c) and (d) have a similar concave shape, where the magnitude of the curvature of the sample is less where the welded material remains and more where the welded material was removed. Additionally, with sample (c), the shape exhibits some amount of deformation that is not seen in sample (d), possibly due to the added constraint of the remaining tape that is present in sample (c) but not in sample (d). In comparing samples (c) and (d), it appears that the UAM welded Al 6061-H18 is in tension after being welded, lessening the magnitude of the curvature. This phenomenon may have been lost after building the UAM welded only Al 6061-H18 samples as described in Section 2.4.1.

2.5.6 Comparison of welded versus non-welded composite stress-strain behavior

In order to determine the discrepancy between 5052 and welded Al 6061-H18 modeling by using individually calibrated material properties for the composite model, two tensile specimens were constructed. One tensile sample was constructed using the same welding parameters as all other tensile samples with the exception of the UAM welded Al 6061-H18 being hand polished prior to being cut from the baseplate. The second sample was constructed using 5052 baseplate alone, along with two individual strips of unwelded Al 6061-H18, where the strips were cut into sub-sized dog-bone shapes. As in previous tensile samples, the painted, speckled observed side of the sample was the 5052 baseplate side. Both the 5052 welded Al 6061-H18 and the 5052 plus two strip Al 6061-H18 composites were tested in tension. Figure 2.47 shows the tensile results and Figure 2.48 shows the samples after uniaxial tensile failure. The welded sample appears to have only one point of failure at a displacement of approximately 0.75 mm. However, on the Al 6061-H18 side of the sample, many surface cracks can be observed (Figure 2.49). It is theorized that as certain parts of the tape experience a strain of approximately 3%, they fail and relieve stain locally, allowing other parts of the tape to then experience approximately 3% strain, continuing on until the 5052 baseplate experiences enough strain to fracture.

The sample tested with the 5052 plus two free, or not welded, tapes behaves similarly to the model, in that the Al 6061-H18 fails and then at a later point, the 5052 fails. As shown in Figure 2.47, the force-displacement profile of both samples behave nearly identically until the first Al 6061-H18 tape fails. The expected reasons for the differences in overall strength and ductility between the two tested samples are two-fold. First, although the Al 6061-H18 has multiple failures throughout the gauge region, it is believed that it is still providing strength and support to the bulk sample throughout the tensile test. Second, because of sample construction, the strain hardening effects to the 5052 apply to the welded sample but do not apply to the unwelded sample.

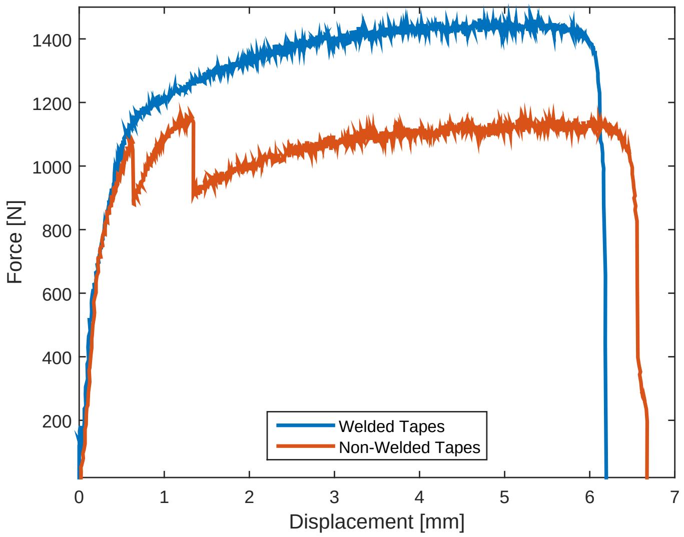

Figure 2.47: Comparison between testing two tapes welded to 5052 base and two unwelded tapes with 5052.

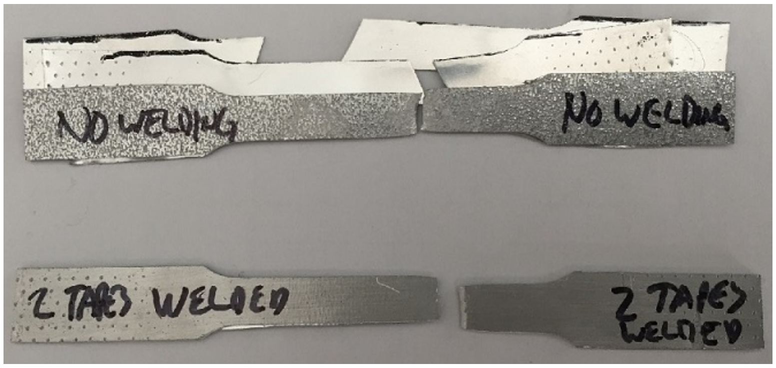

Figure 2.48: Sub-size dog-bone samples for two unwelded tapes with 5052 (Top) and two tapes welded to 5052 base (Bottom).

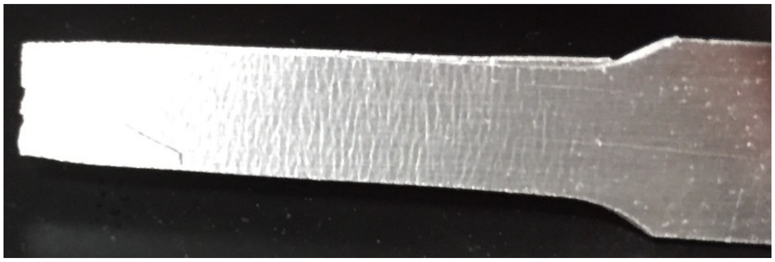

Figure 2.49: Al 6061-H18 welded onto 5052 base-layer post tensile test. Many small surface cracks are visible.

Figure 2.50 shows how the effective stress changes as each of the tapes breaks. At the point where each tape fails in tension, the area was adjusted assuming a new initial area corresponding to the remaining tensile load.

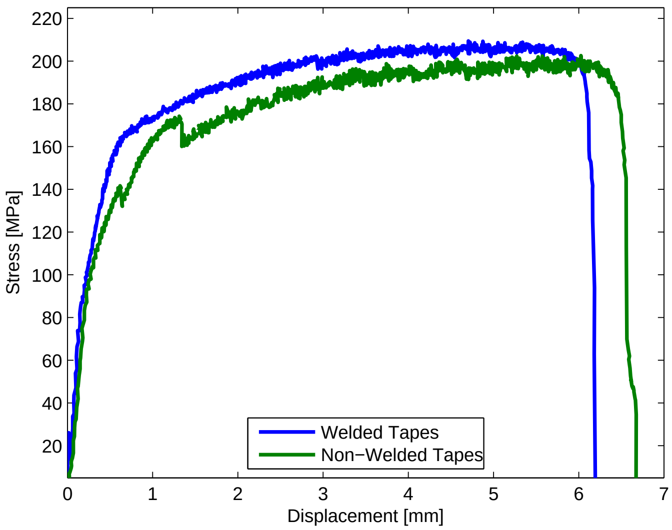

Figure 2.50: Comparison between testing two tapes welded to 5052 base and two unwelded tapes with 5052 accounting for the area loss as each tape breaks.

The welded-unwelded comparison was also conducted using finite element analysis (FEA), performed by Dr. Xiang Chen, assuming 5052-O baseplate and the cold rolled 5052 baseplate. The result is shown in Figures 2.51 and 2.52. In both unwelded cases, a sudden stress drop at around 2.3% engineering strain (the failure strain of 6061-H18) is predicted, which is expected. In comparison, stress drop in the welded cases happens closer to the true failure strain of 6061-H18. This is due to the transverse constraint of necking provided by the 5052 baseplate and carried through the bonded interface. However, such a transverse constraint cannot possibly increase the failure strain of 6061-H18 above its **true** failure strain. Therefore, the experimentally-observed failure mode of the welded bilayer, namely, the simultaneous fracture of both layers, cannot be reproduced in FEA without altering the single material model, which can be accomplished in future work.

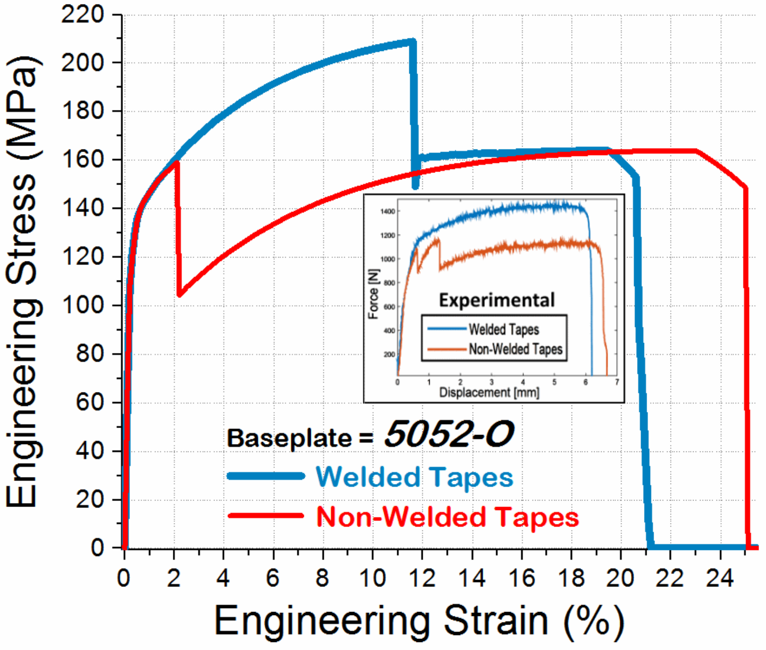

Figure 2.51: Comparison of welded and unwelded bilayer tensile stress-strain curves predicted by FEA, assuming 5052-O baseplate. The experimental force-displacement curve is included in the inset figure.

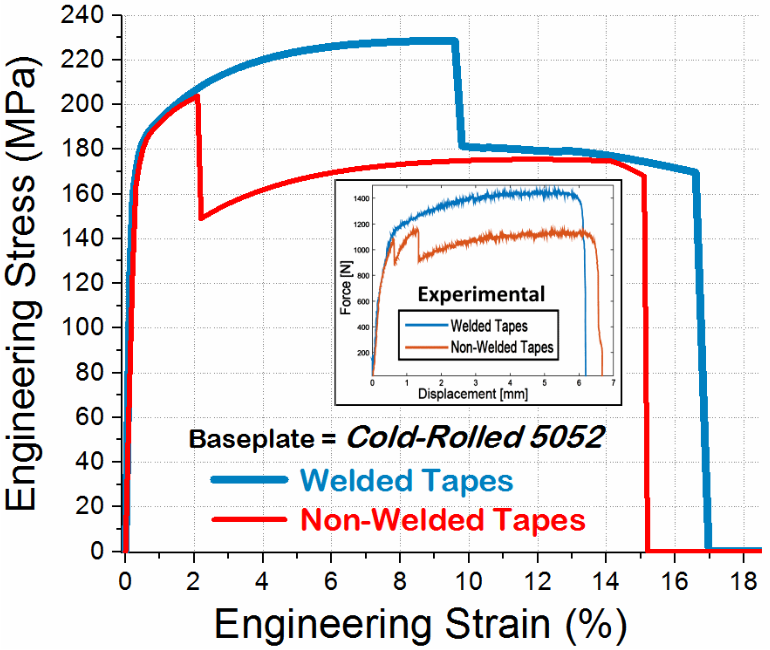

Figure 2.52: Comparison of welded and unwelded bilayer tensile stress-strain curves predicted by FEA, assuming cold-rolled 5052 baseplate. The experimental force-displacement curve is included in the inset figure.

2.6 Experimentally characterize the fiber-matrix interface of UAM reinforced coupons

2.6.1 Construct UAM fiber pullout coupons

Fiber pull coupons were constructed similarly to those constructed by Hehr [9] and are illustrated in Figure 2.53. Prior to welding Al 6061-H18 to the 5052 base plate, small channels, shown in Figure 2.54, were machined where the fiber will be loose between the tab and the fiber pullout fixture. The small channels are necessary to remove the material around the fiber without damaging the fiber or sample after all welding is complete. The channel serves as a hole for future removal of neighboring material. The size was minimized as to maximize the material that will support the welder as it welds over the hole. After the holes are cut, a channel was made in the same fashion as the channels made for the fibers in the tensile specimens. The fibers were welded over using the same welding parameters as the tensile samples. After welding, the fiber pullout samples were cut from base plate using a custom CNC program. After the samples were cut out, a utility knife was used to remove the material joining the test strip to the bulk tab, with extreme caution as to not damage the fibers or the fiber pull samples. Fiber pull samples were made for SiC and Zylon fiber bundles. Due to the excessive channel size compared to fiber geometry needed to embed Dyneema, the fibers were loose within the channel and Dyneema fiber pull samples could not be created.

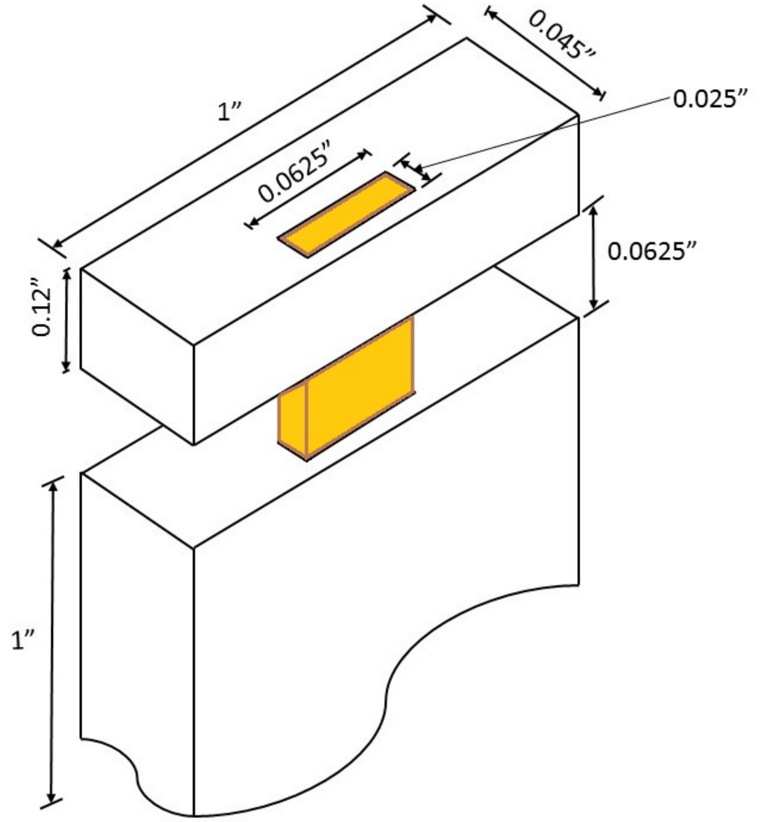

Figure 2.53: Fiber pull sample geometry with fiber represented in yellow.

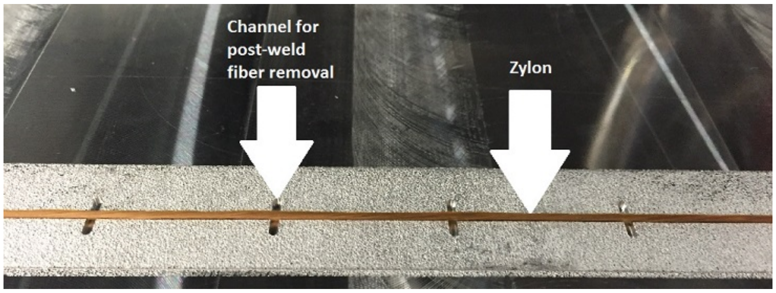

Figure 2.54: Intermediate stage of fiber pull sample construction where channels both for fiber placement and for material removal to final sample dimensions have been cut and a fiber bundle has been laid in the channel.

The same test rig and setup that Hehr [9] used for fiber pull samples was used for this testing. Figure 1.7 shows how the samples are placed in the fixture for testing. The number of fibers and channel depth was chosen so to meet the 10% VF goal while maintaining the integrity of the channel. The fiber pullout test results were used to guide the development of a representative tensile model of the SiC and Zylon MMCs.

2.6.2 Test UAM fiber pullout coupons

The results for fiber pull testing of SiC and Zylon are shown in Figures 2.55 and 2.56 as well as in Table 2.9. Fiber pullout test results show similar engagement of the fibers within the channel with both Zylon and the SiC fiber bundles with the exception that the SiC exhibits a sharp stick-slip behavior during the initial pull. Some of the Zylon samples held nearly three times the load of the SiC samples. This is most likely due to contact area. The SiC channel was filled with (45) 0.0056 in. (0.14224 mm) diameter fibers while the Zylon channel was filled with thousands of fibers into the same volume. Although the SiC outperformed the Zylon during tensile testing, the

SiC performed far worse than the Zylon during fiber pull testing because of better frictional fiber engagement of the fibers with the channel in the Zylon samples, which was the only force maintaining the fiber in the channel.

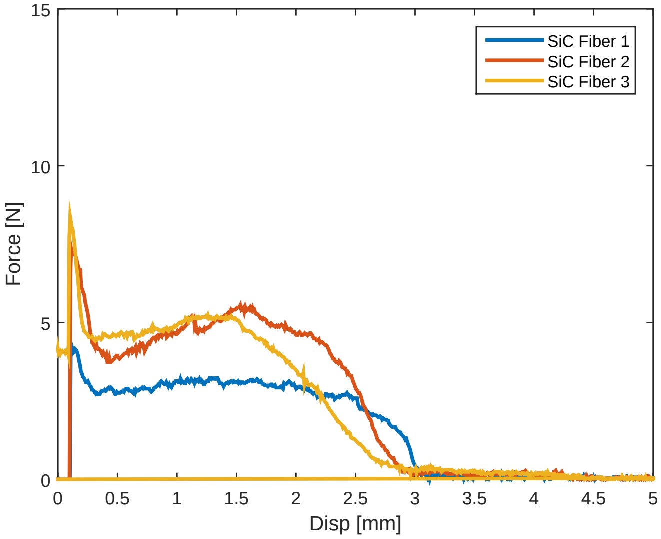

Figure 2.55: SiC fiber reinforced metal matrix composite fiber pull behavior.

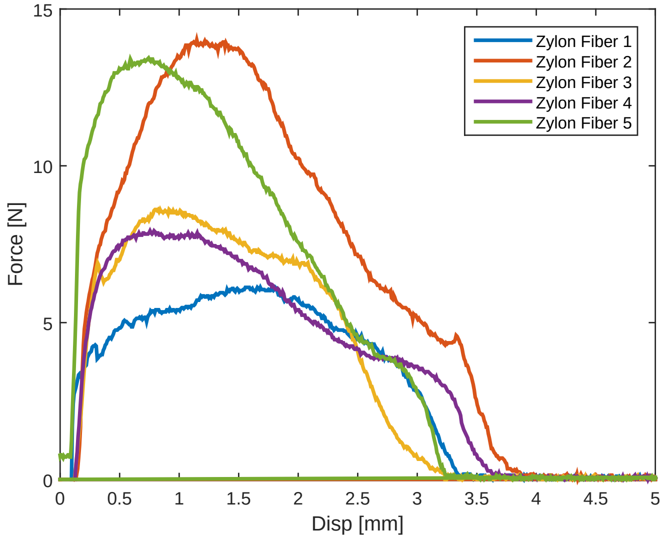

Figure 2.56: Zylon fiber reinforced metal matrix composite fiber pull behavior.

Table 2.9: Maximum observed force for fiber pull samples.

Sample	**Max Observed Force** [N]
SiC 1	4.3
SiC 2	7.3
SiC 3	8.4
Zylon 1	6.1
Zylon 2	14.0
Zylon 3	8.6
Zylon 4	7.9
Zylon 5	13.4

2.7 Key Findings and Recommendations

This study explored two new aspects to UAM as a means to reinforce base material. The first being a look at different materials, such as thermoplastics and thermoset polymers. The second being the use of UAM to directly reinforce a thin (0.9 mm) base material, both by welding Al 6061-H18 to the base, and by embedding reinforcing fibers within the aluminum, making an overall stronger component, relative to density. Welding on thin sheets has its complications, but has great potential for integrating the base material into the final part, instead of using the base as something to be discarded.

Key findings:

- Directly embedded HSS wires within Al 6061-H18 matrix without using channels.
- Embedded aramid thread bundle inside a machined channel within 6061-H18 matrix.
- Welded Al 6061-H18 tapes to a 0.9 mm thick Al 5052-O baseplate.
- Embedded Zylon, Dyneema and SiC fiber bundles, individually, inside a machined channel within Al 6061-H18/Al 5052-O matrix.
- Fiber friction alone is not enough to absorb significant composite load without slipping.
- Slipping of the fiber within the matrix can be used to increase the overall toughness of a composite with the fibers continuing to bear load after matrix failure.

Recommendations:

- Investigate means to improve matrix-fiber interface to allow the fiber to bear more load, increasing the overall strength of the composite.
- Tune the slippage of fibers within the matrix to maximize fiber loading without breaking, allowing the fiber to continue to bear load beyond its normal failure strain.
- Explore other types of thin base plate materials with higher yield strengths to determine if the deformation of the base can be avoided, and successful welds produced.
- Investigate discrepancy between model of Al 6061-H18 and 5052-O and observed behavior.
- Investigate embedding fibers in complex channels or chemically treating fibers, improving mechanical interlocking, to improve the friction between the fibers and the channel, allowing them to bear more load under tension.

Chapter 3: Strength Reduction in Weld Direction of Metal Matrix due to UAM Process Parameters of UAM-Only Constructed Parts

3.1 Motivation

When creating parts using UAM, it is desirable for the parts to be as strong as possible, without sacrificing weld quality. A decrease in the in-plane ultimate tensile strength of Al3003-H18 and Al6061-H18 as a result of welding with a 9 kW UAM system, as shown in Figures 3.1 and 3.2, and Table 3.1 was observed as a result of UAM welding. There was little change in the elongation at failure for the tested samples, but there was a reduction in overall strength. It was hypothesized that the decrease in strength that results from the UAM process is due to residual stress within the part imparted by the welding process. It was believed that the elastic deformation occurs in the tape when the sonotrode presses it against the metal base plate which is locked into place during the ultrasonic welding process. The initial focus of this study was to develop fundamental understanding of the cause for the reduction in x-tensile (in-plane) strength resulting from the UAM process and to attempt to develop weld parameters that can reduce or eliminate the reduction in strength without sacrificing interfacial bond strength.

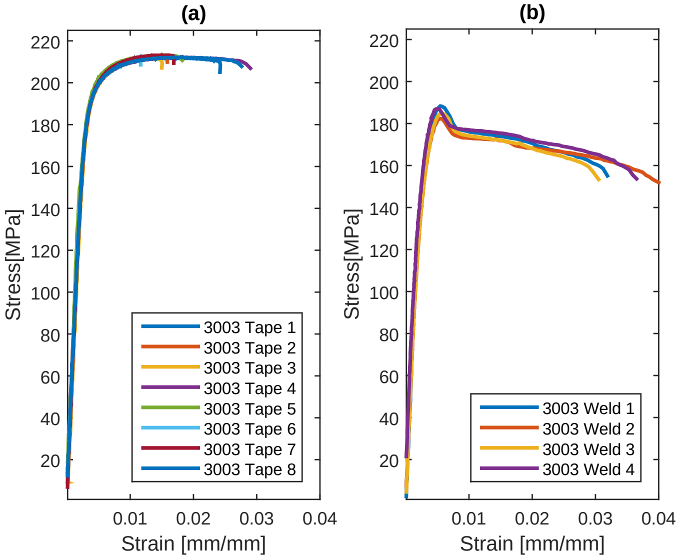

Figure 3.1: Tensile test comparison of Al 3003-H18 tape (a) as-received and (b) after UAM welding.

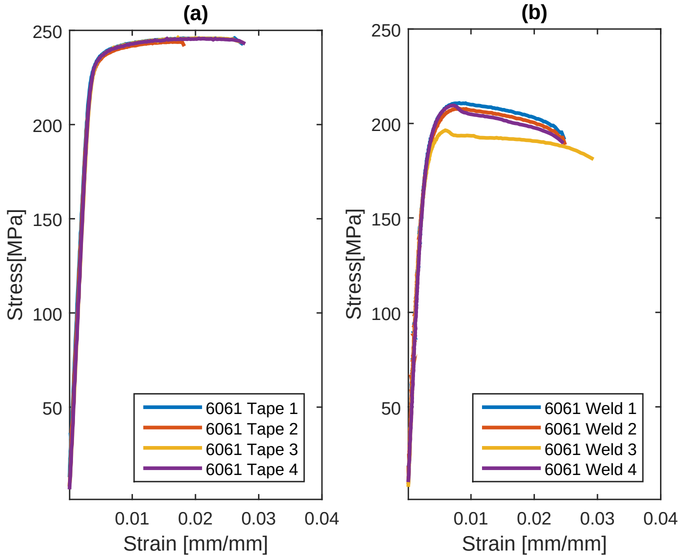

Figure 3.2: Tensile test comparison of Al 6061-H18 tape (a) as-received and (b) after UAM welding.

Table 3.1: Pre and post weld tensile strength comparison.

	6061 Tape	6061 UAM	3003 Tape	3003 UAM
Average UTS [MPa]	245.47	206.2	212.4	185.6
Standard Deviation [MPa]	0.923	6.63	0.63	2.62

During work discussed in the previous chapter, it was observed that a decrease in x-tensile (weld direction) strength occurred relative to the as-received tape after welding with a 9 kW UAM system. Figure 3.2 and Figure 3.1 show the difference in x-tensile behavior between as-received aluminum tapes (6061/3003) manufactured to an H18 condition (before being welded using UAM) and tapes after being welded together. For both materials, 5000 N was used as the normal force during the welding process. Using the average values, a reduction in ultimate tensile strength of 16.0% and 12.6% occurred for the 6061 and 3003 builds, respectively.

What causes the changes in mechanical properties of the UAM-welded tapes using a 9 kW UAM system are not yet understood. In contrast to the observed reduction, a study by Schick et al.[32] showed that welding Al 3003-H18 with a 1 kW UAM system, using the optimized parameters at the time (Table 3.2), increased x-tensile strength by 17% despite the presence of voids and lower weld strength compared to 9 kW builds. This difference in x-tensile strength may be due to the large difference between Schick's 1 kW system weld parameters and the 9 kW system parameters which were developed by Wolcott et al. [11] and used in related work (Table 3.2). Wolcott et al. [11] showed that the strength between layers (z-direction) increases as amplitude is increased and weld speed is decreased, but did not quantify the strength of the material along the weld direction. Before this document, there has been no published literature showing a decrease of in-plane mechanical properties post UAM welding.

Possible explanations for the observed knock-off of in-plane strength are that the 9 kW UAM process imparts residual stresses by locking elastic deformation within the build or imparts cold work by plastically deforming the tape with the rolling action of the horn. In order to isolate residual elastic stress from cold work due to rolling, as-received tape was cold rolled without ultrasonic welding and tested. No statistical difference in ultimate tensile strength or elongation was observed between the as-received and cold-rolled tapes. This indicates that the UAM welding process is causing the reduction in strength, and not cold work due to the rolling action of the horn over the tape. As a result, the hypothesis, which is described in the previous section, is that the decrease in strength that results from the UAM process is due to residual stress (stored elastic deformation) within the part. However, this hypothesis cannot be proven or dis-proven without accurately measuring the residual stress. Assuming that the residual stress is uniform across the plane perpendicular to the weld force, the residual stress can be determined using the hole-drilling strain-gage method as well as neutron diffraction. If the residual stress hypothesis is confirmed, then 1 kW weld parameters may eliminate the knock-off in x-tensile strength, but with lower weld quality and resulting z-tensile strength. It is therefore necessary to examine the effects of weld parameters on both in-plane strength and weld quality in order to maximize overall part strength. It is also necessary to investigate heat treatments as a means of mitigating the residual stress imparted by the UAM process.

Table 3.2: 1 kW (Schick et al. [32]) vs 9 kW system weld parameter comparison.

	1 kW System Parameters	9 kW System Parameters
Amplitude [μm]	18-21	31
Speed [mm/s]	25-50	84.7
Force [N]	800-1500	5000
Pre-Heat [^{o}C]	65-150	26

3.2 Design of Experiments Setup

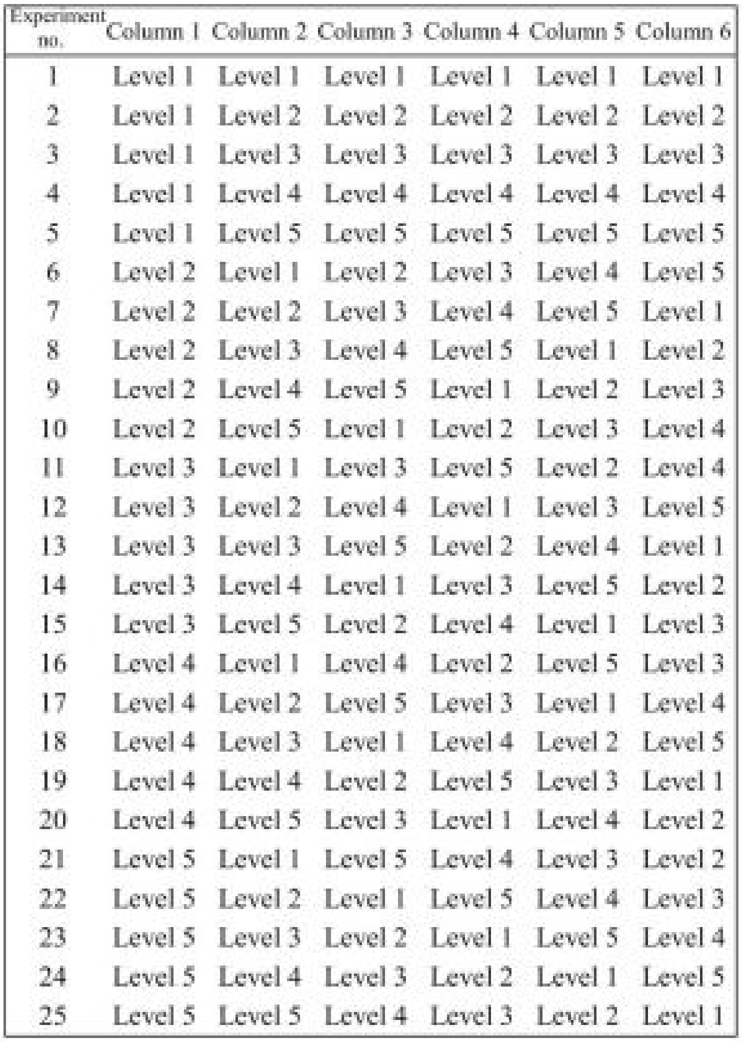

Experiment no.	Column 1	Column 2	Column 3	Column 4	Column 5	Column 6
1	Level 1	Level 1	Level 1	Level 1	Level 1	Level 1
2	Level 1	Level 2	Level 2	Level 2	Level 2	Level 2
3	Level 1	Level 3	Level 3	Level 3	Level 3	Level 3
4	Level 1	Level 4	Level 4	Level 4	Level 4	Level 4
5	Level 1	Level 5	Level 5	Level 5	Level 5	Level 5
6	Level 2	Level 1	Level 2	Level 3	Level 4	Level 5
7	Level 2	Level 2	Level 3	Level 4	Level 5	Level 1
8	Level 2	Level 3	Level 4	Level 5	Level 1	Level 2
9	Level 2	Level 4	Level 5	Level 1	Level 2	Level 3
10	Level 2	Level 5	Level 1	Level 2	Level 3	Level 4
11	Level 3	Level 1	Level 3	Level 5	Level 2	Level 4
12	Level 3	Level 2	Level 4	Level 1	Level 3	Level 5
13	Level 3	Level 3	Level 5	Level 2	Level 4	Level 1
14	Level 3	Level 4	Level 1	Level 3	Level 5	Level 2
15	Level 3	Level 5	Level 2	Level 4	Level 1	Level 3
16	Level 4	Level 1	Level 4	Level 2	Level 5	Level 3
17	Level 4	Level 2	Level 5	Level 3	Level 1	Level 4
18	Level 4	Level 3	Level 1	Level 4	Level 2	Level 5
19	Level 4	Level 4	Level 2	Level 5	Level 3	Level 1
20	Level 4	Level 5	Level 3	Level 1	Level 4	Level 2
21	Level 5	Level 1	Level 5	Level 4	Level 3	Level 2
22	Level 5	Level 2	Level 1	Level 5	Level 4	Level 3
23	Level 5	Level 3	Level 2	Level 1	Level 5	Level 4
24	Level 5	Level 4	Level 3	Level 2	Level 1	Level 5
25	Level 5	Level 5	Level 4	Level 3	Level 2	Level 1

Figure 3.3: Taguchi L25 orthogonal array, with five levels and six parameters [33].

3.2.1 Weld Parameter Variation

Force, peak to peak vibration amplitude, and weld speed account for the major differences between the 1 kW and 9 kW welding systems. Therefore, by varying force, amplitude and speed, starting from the ideal parameters used in Schick's [32] study up to the parameters identified as ideal during the Wolcott study [11], the cause of the tensile strength degradation may be identified. Using a Taguchi L25 orthogonal array (Figure 3.3), with three factors and five levels, Table 3.3 was generated, along with 5 other tables. All of the tables were variations of Table 3.3,using only columns 1, 2 and 3, with each possible variation of order with respect to force, amplitude and speed. Base plate temperature was held constant for this study. Although a feature of the OSU UAM welding system, it is not a normally used parameter when welding aluminums.

Pilot welds, shown in Figure 3.4, were conducted to determine the weldability of the parameter sets shown in Table 3.3. This parameter set was determined to be adequate to proceed to the DOE.

Table 3.3: Knockoff DOE treatments.

Treatment	**Amplitude**	**Force**	**Speed**
Number	**[micron]**	**[N]**	**[mm/s]**
1	20	1000	21
2	20	2000	37
3	20	3000	52
4	20	4000	68
5	20	5000	85
6	24	1000	37
7	24	2000	52
8	24	3000	68
9	24	4000	85
10	24	5000	21
11	28	1000	52
12	28	2000	68
13	28	3000	85
14	28	4000	21
15	28	5000	37
16	32	1000	68
17	32	2000	85
18	32	3000	21
19	32	4000	37
20	32	5000	52
21	36	1000	85
22	36	2000	21
23	36	3000	37
24	36	4000	52
25	36	5000	68

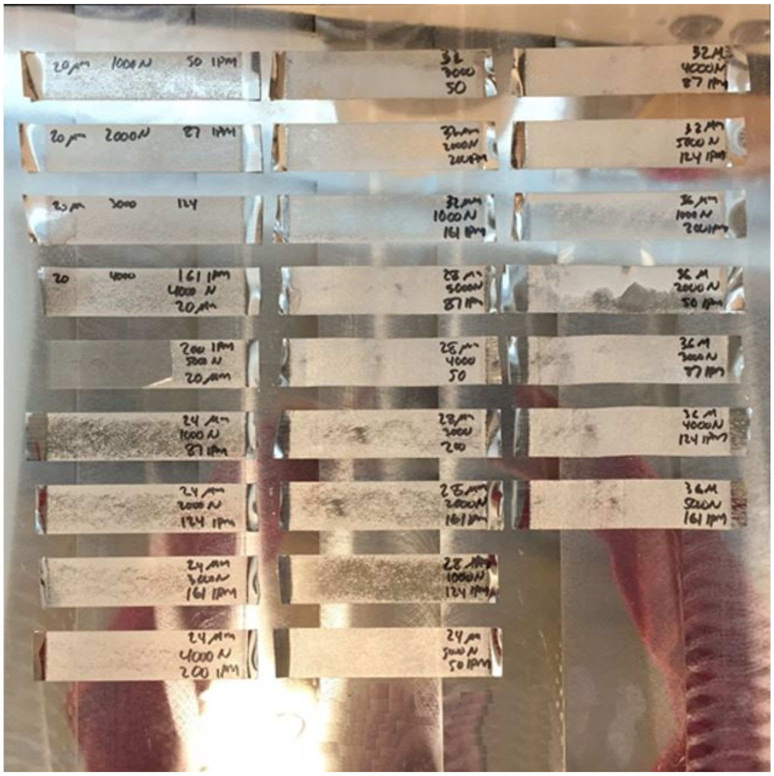

Figure 3.4: Pilot welds using weld parameter sets from Table 3.3.

Tensile Testing: X-tensile testing (weld direction) was used to characterize the stress-strain behavior of UAM constructions. The testing generated stress-strain profiles that allowed for the comparison of ultimate tensile strength and failure strain of each of the builds. The testing was guided by ASTM E8 (Standard Test Methods for Tension Testing of Metallic Materials)[6]. All sample areas along the gage length were measured using a micrometer accurate to 0.0001 in. (0.00254 mm), and recorded. All testing was conducted on an Interlaken Series 3300 test frame using a 5000 lbf. (22.2 kN) load cell. All strain measurements were captured using DIC.

Weld Quality Testing: While not conducted as part of this study, weld quality testing will be necessary to observe the effects of the chosen parameter sets. This testing will help to correlate X-tensile strength with weld quality. In order to allow for more freedom in choosing the weld quality measurement techniques, builds were constructed with twenty-five layers.

3.3 Procedure used to manufacture tensile specimens.

In order to produce the tensile specimens needed for the DOE described above, a consistent procedure was followed. A series of programs were created for the UAM machine to follow that allowed for consistent weld parameters and machining operations to take place. This procedure helped to maintain consistency across samples, even though the samples were created over a four month period.

1. The surface of the plate was machined flat using a custom CNC program. The amount of material removed was minimized to maintain consistency from sample to sample and avoid clearance issues with the welder and the plate.

2. A texture pass was made by the welder. A texture pass has been proven to help the first tape weld to the base plate, by making the weld stronger, able to absorb more energy before failure, and make the welds more consistent [16]. Anecdotally, the first weld of the tape onto the baseplate has been shown to be the weakest, where the tapes seem to weld together, and stay together, but pop off of the base plate, sometimes catastrophically. Texture pass parameters are listed in Table 3.4.

Table 3.4: Texture parameters used for X-direction tensile strength reduction DOE.

	Force [N]	**Amplitude [micrometers]**	**Speed [in/min]**	**Dwell [ms]**
Spot Parameters	5000	20	-	100
Weld Parameters	5000	20	200	-

3. The first tape was welded with a set of known parameters that have proven to be adequate for welding 6061-H18[11]. The parameters for the first tape are listed in Table 3.5.

Table 3.5: First tape parameters used for X-direction tensile strength reduction DOE.

	Force [N]	**Amplitude [micrometers]**	**Speed [in/min]**	**Dwell [ms]**
Spot Parameters	5000	28	-	300
Weld Parameters	5000	28	200	-

4. An additional weld pass was made by the welder without laying a tape. Not always, but sometimes, the first tape does not stick well to the baseplate. Therefore, another pass is made without laying tape to help weld the unwelded part of the tape to the base plate, providing for a consistent and high quality initial weld. The parameters used for this pass are listed in Table 3.6.

Table 3.6: Second welding pass on first tape parameters used for X-direction tensile strength reduction DOE.

	Force [N]	**Amplitude [micrometers]**	**Speed [in/min]**	**Dwell [ms]**
Spot Parameters	5000	28	-	300
Weld Parameters	5000	28	200	-

5. Twenty-five layers are then attempted using the parameters listed in Table 3.7. Because some of the samples being constructed are at the limit of “good” welding parameters, some of the samples pop off from the base during welding before (25) layers can be welded. While this is not ideal for consistency from sample to sample, it does illustrate how stresses within the part may be influencing the welded area, and causing the sample to peel up from the base. One sample from each experiment set was photographed after welding (shown in Appendix C).

Table 3.7: Weld parameters used for X-direction tensile strength reduction DOE.

	Force [N]	**Amplitude [micrometers]**	**Speed [in/min]**	**Dwell [ms]**
Spot Parameters	5000	28	-	300
Weld Parameters	*	*	*	-
***Parameters used are from Table 3.3 for specific treatment to investigate.**				

6. The samples are then cut into sub-sized dog-bone shapes with dimensions commiserate with ASTM E8[6]. The samples are cut to a depth that is just above

the first welded layer, so that the sample only includes the layers welded at the parameters listed in Table 3.7. Figure 3.5 shows a weld sample with the dog-bone shape cut out.

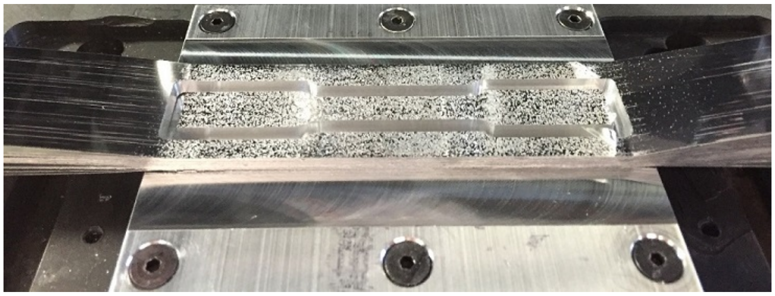

Figure 3.5: Dog-bone shape cutout of welded area.

7. After the sample shape is cut out from the top, the sample needs to be removed from the base. This is accomplished by mounting the sample upside-down and machining out the bottom to get to the sample. Figure 3.6 shows a sample before being mounted to the fixture on the the bottom, and a sample that is mounted in preparation for being removed a the top.

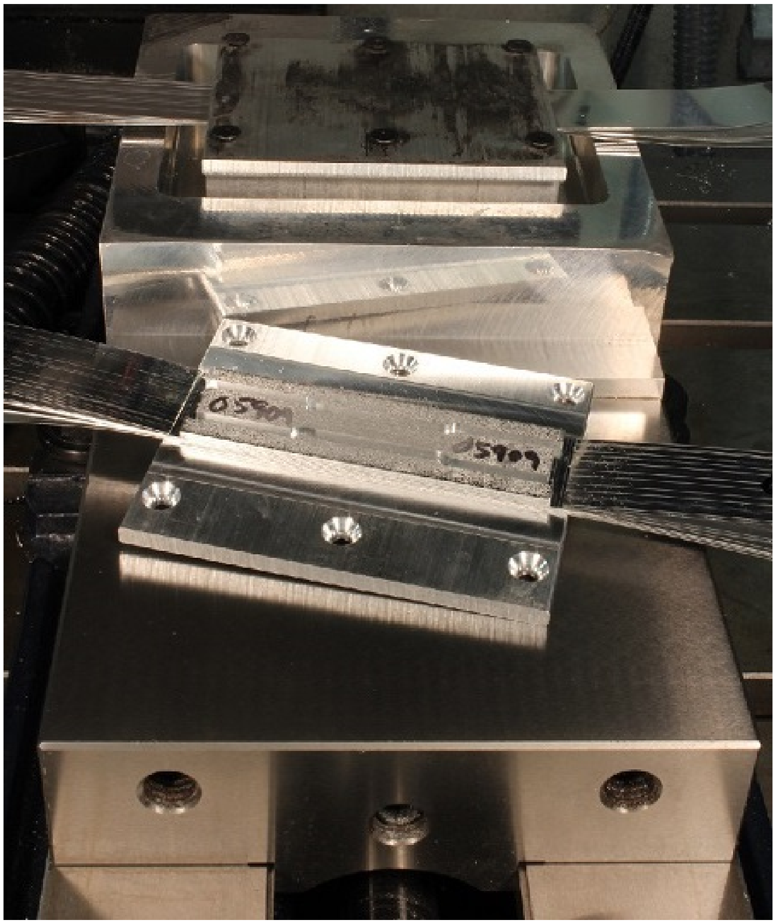

Figure 3.6: (TOP)Dog-bone shape mounted to be removed from the base plate on a custom fixture. (BOTTOM) Sample with dog-bone shape cutout, before being removed.

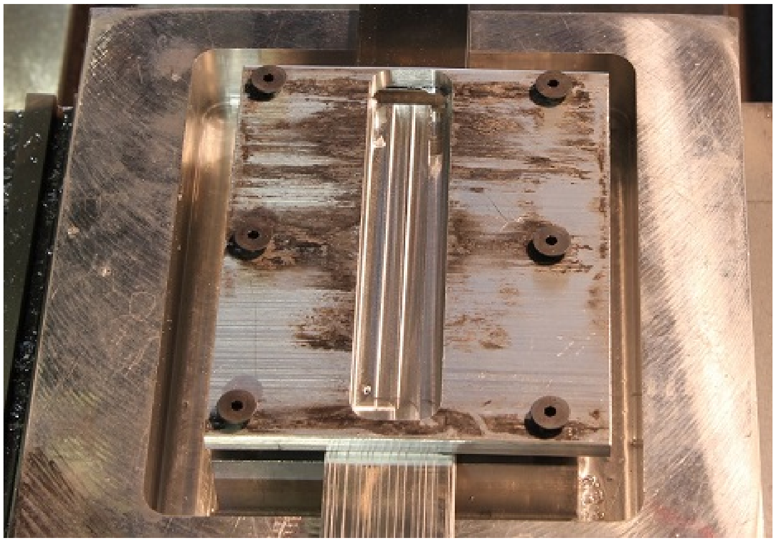

Figure 3.7: Mounted sample after machining out from the bottom. The sample is cut leaving a thin membrane around the dog-bone that is easily peeled away after the sample is removed from the fixture.

3.4 X-Tensile Strength Results

Samples were constructed in a random order, using a Matlab random number generator. Samples were tested in batches as they were created. Each sample was tested on an Interlaken 3300 series load frame with a 5000 lbf. (22.2 kN) load cell at a displacement rate of 0.05 in/min (0.021 mm/s). Strain measurements were taken using a Correlated Solutions DIC system. A virtual 1 in. (25.4 mm) extensometer was used for strain measurements as part of post-processing. Sample cross-sectional areas were measured using a micrometer accurate to 0.0001 in. (0.00254 mm).

Ultimate tensile strength and strain at failure data was taken from each test result and analyzed in Minitab using the Taguchi design of experiments feature [34]. Once the Taguchi matrix parameter sets are entered into Minitab, the 3 factor and 5-level design was selected. The option was chosen for ”Larger is Better”, which analyzes the model optimizing for the highest response output. Only the means were analyzed.

3.5 Qualitative Observations

3.5.1 Stress-strain Profiles

The stress-strain profiles of the Al 6061 UAM samples created with varying weld parameters, and tested in tension showed, two distinct failure mechanisms. The first of which is typical of aluminum, the second is normally observed in low carbon steels.

1. Experiment numbers 1 thru 9, 11 thru 13, 16, 17 and 21 exhibited normal aluminum behavior, similar to the graph shown in Figure 3.8. Under a tensile load, the sample is initially in the elastic region, until continued loading causes the sample to reach its yield point. Strain hardening occurs until it reaches its UTS, at which point the sample begins to neck, where the cross-sectional area decreases faster in a localized area than the change in load allows for increasing stress until the sample eventually fails. For the aluminum samples tested, the samples tended to experience brittle fracture after entering the necking region, with a sudden catastrophic failure.

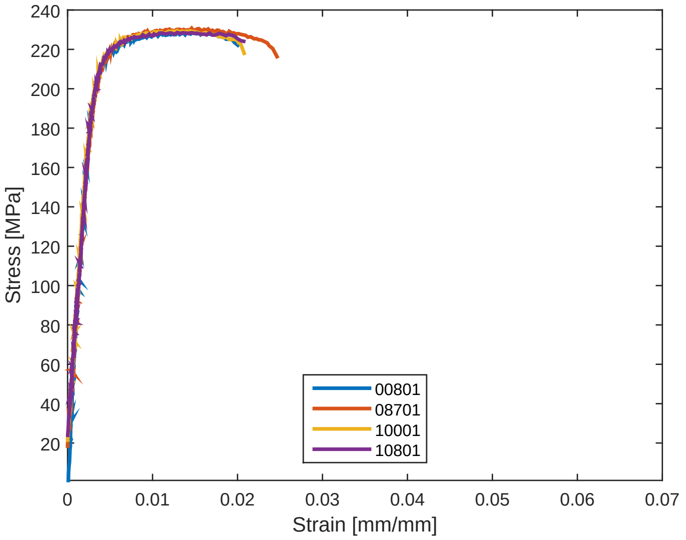

Figure 3.8: Stress-strain plot of X-direction tensile strength reduction sample set #01, representing a single yield point, which is common for most aluminum and aluminum alloy's stress strain behavior.

2. Experiment numbers 10, 14, 15, 18 thru 20, 24, and 25 exhibited abnormal behavior for aluminum under a tensile load, similar to the graph shown in Figure 3.9. After the aluminum reaches its yield point, the stress strain curve has a sharp drop. This is most likely due to dislocations escaping from Cottrell atmospheres. The relief of stresses around a dislocation by foreign atoms in solid solution can cause an equilibrium "atmosphere" to form, in which large solute atoms are gathered in the dilated part of the dislocation field and the small ones in the compressed part [35]. This atmosphere was originally described in low carbon steels [35], but has been applied to aluminum where impurities are available [36]. Another necessity for the Cottrell atmosphere to form is

the abundance of dislocations, or a high dislocation density. It is hypothesized that the UAM process, through deformation of the tapes due to pressure and ultrasonic vibrations, can supply the necessary deformation needed to increase dislocation density.

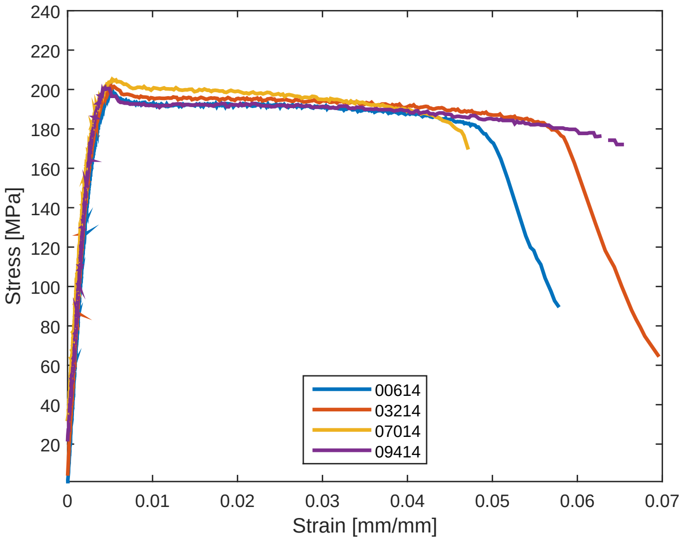

Figure 3.9: Stress-strain plot of X-direction tensile strength reduction sample set #14, representing a double yield point, which is uncommon for most aluminum and aluminum alloy's stress strain behavior.

In order to better understand what parameters, or combinations of parameters, that may help to predict the stress strain behavior, plots were generated that show the occurrence of a double or single yield point as parameters are varied. Figure 3.10 shows that both failure strain and UTS are correlated with the presence of a single and double yield point. Figure 3.11 shows that using only amplitude, force or speed individually, there is no clear interaction. Figure 3.12 shows different interaction combinations between amplitude, force and speed.

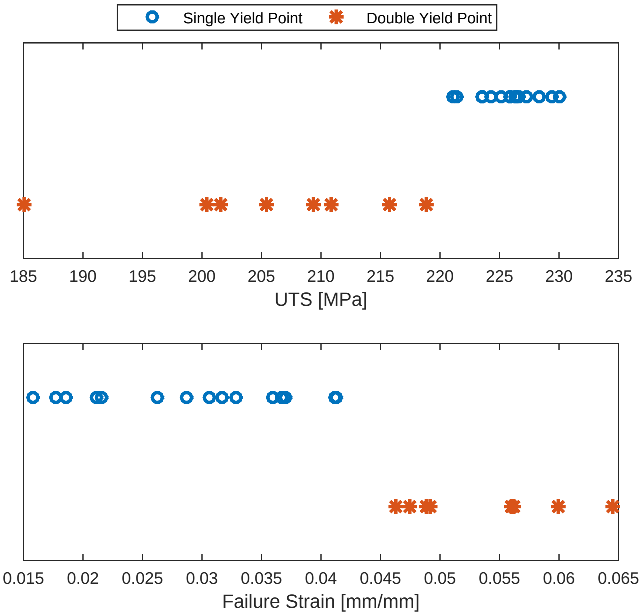

Figure 3.10: Visualization of single and double yield points as they relate to mean UTS and failure strain of X-Tensile samples.

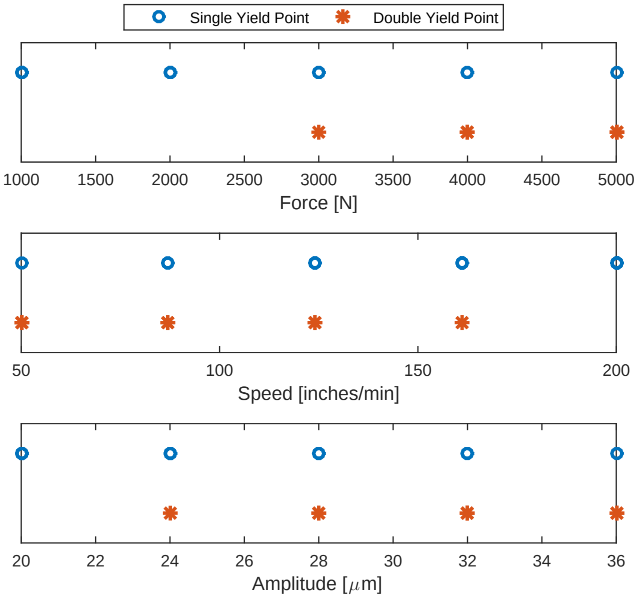

Figure 3.11: Visualization of single and double yield points as they relate to force, speed and amplitudes as individual factors.

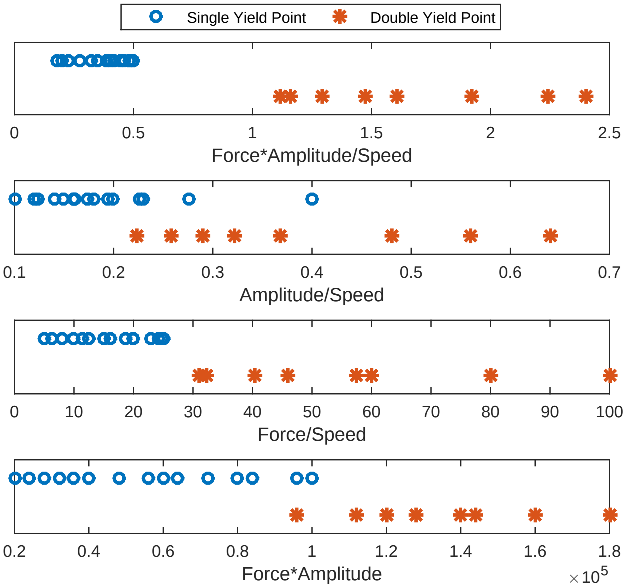

Figure 3.12: Visualization of single and double yield points as they relate to the interactions of force, speed and amplitudes.

The interaction of force*amplitude/speed, hereto referred to as Weld Energy Density (U_{weld}), was introduced by Dr. Xiang Chen through the course of this work. U_{weld} is strongly correlated with the single and double yield points, while other interactions seem to be correlated, but less strongly. U_{weld} has a physical basis and is represented by,

$$U_{weld} = \gamma_{eff} * \mu_{eff} * \beta \frac{F_N * a * 2 * \pi * f}{S * A_{tape}}, \tag{3.1}$$

the amount of energy deposited per unit volume, where U_{weld} is the weld energy density $[J/m^3]$, F_N is the normal force applied by the welder $[N]$,a is the welder amplitude, peak to peak $[\mu m]$,S is the weld speed in the X-direction $[inches/min]$, f is the frequency of welder vibration $[kHz]$, A_{tape} is the cross-sectional area of tape under horn [m^2], μ_{eff} is the non-dimensional frictional coefficient, γ_{eff} is the non-dimensional term to account for amplitude losses due to base deflection, and β is the non-dimensional term to account unit conversion. The welder inputs are F_N, a and S. The fixed values are A_{horn} and f. If you assume that $\mu \approxeq 0.2$ and $\gamma \approxeq 0.25$, plugging in normal weld parameters, the total energy entering the weld is approximately 60% of the energy that is sent to the transducers. With losses to the system due to efficiency losses and losses due to exciting the base, this number is reasonable. This idea of U_{weld} was inspired through discussions of this research and warrants further study.

3.5.2 Optical Microscopy

Optical microscopy was used as a visual observation of weld quality for select samples. The sample that failed with the highest UTS and the sample that failed with the lowest UTS were each cross-sectioned and photographed under an optical microscope. The sample that failed with the lowest UTS was a sample from group 18, where a force of 3000 N, amplitude of 32 μm, and a speed of 50 inches/min were used as the construction parameters. The sample that failed with the highest UTS was a sample from group 21, where a force of 5000 N, amplitude of 36 μm and speed of 200 inches/min were used.

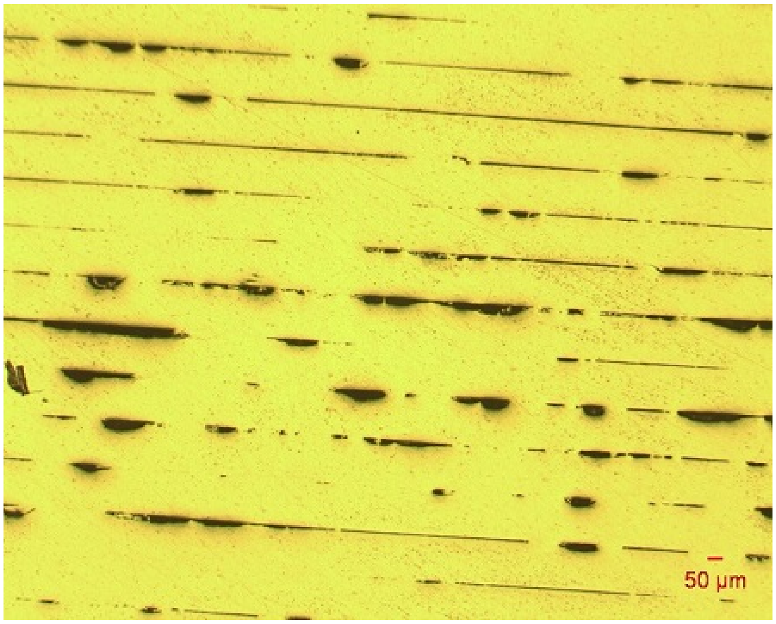

Figure 3.13: Sample from group 21, with the highest X-tensile UTS from the Al 6061-H18 X-tensile DOE (Not typical for 9 kW UAM systems welding Al 6061-H18).

Figure 3.14: Sample from group 18, with the lowest X-tensile UTS from the Al 6061-H18 X-tensile DOE (More typical of 9 kW UAM systems welding Al 6061-H18).

Figures 3.14 and 3.13 show vastly different weld quality. Of note, theses samples were created to attempt to glean insight into parameters that influence X-tensile strength, and were not constructed using optimized parameters for Al 6061-H18 [11]. Figure 3.14 is similar to what is common for 9 kW systems, where no voids are visible using optical microscopy. Figure 3.13 shows some bonding, but heavily resembles microscopy from aluminum builds constructed using low power systems. While not studied fully in this experiment, there appears to be an inverse relationship between the gapless welds and the X-tensile strength. Future work can quantify this relationship, and hopefully be used to identify a parameter set that produces high weld quality without sacrificing X-tensile strength.

3.5.3 Quantitative Results and Statistical Modeling

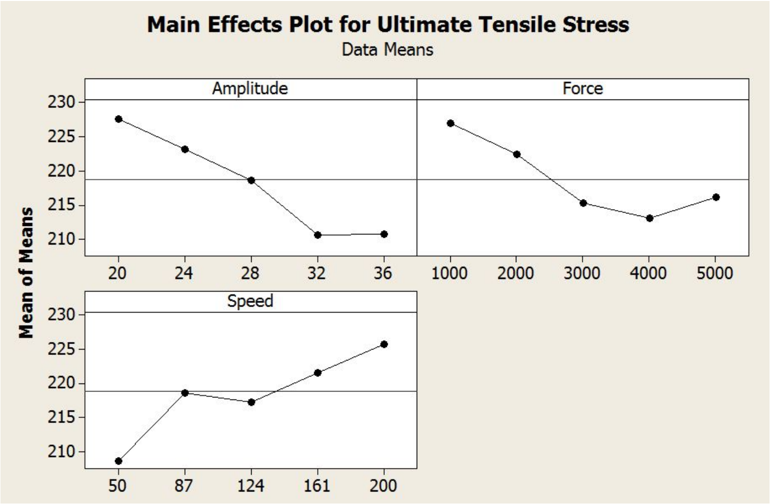

Figure 3.15: Main effects plot showing amplitude, force and speed trends for UTS values.

Table 3.8: ANOVA table for X-tensile UTS.

Source	DF	Seq SS	Adj SS	Adj MS	F	P
Amplitude	4	1010.8	1324.1	331.02	11	0.001
Force	4	655.7	689.7	172.42	5.73	0.012
Speed	4	950.9	950.9	237.72	7.9	0.004
Residual Error	10	300.8	300.8	30.08		
Total	22	2918.2				

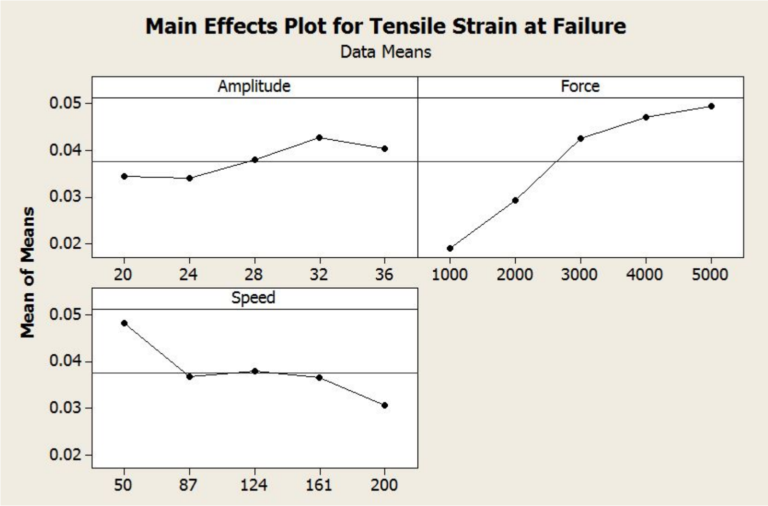

Figure 3.16: Main effects plot showing amplitude, force and speed trends for failure strain values.

Table 3.9: ANOVA table for X-tensile strain at failure.

Source	DF	Seq SS	Adj SS	Adj MS	F	P
Amplitude	4	0.000271	0.000342	0.000085	3.3	0.057
Force	4	0.003247	0.003103	0.000776	29.97	0.000
Speed	4	0.000659	0.000659	0.000165	6.37	0.008
Residual Error	10	0.000259	0.000259	0.000026		
Total	22	0.004437				

Weld force, weld speed and weld amplitude were found to be statistically significant parameters affecting the ultimate tensile strength and strain at failure of the tested samples. As seen in Figure 3.15, increasing weld amplitude and weld force and decreasing weld speed all led to a knock-off in ultimate tensile strength. As seen in Figure 3.16, increasing weld force led to an increase in strain at failure was the most substantial effect. Table 3.8 shows that force, speed and amplitude are all significant with p-values < 0.05 for X-Tensile UTS. Table 3.9 shows that force and speed are significant with p-values < 0.05 for X-tensile strain at failure. Amplitude, with a p-value of 0.057 is not significant within a confidence interval of 95%, but, because it is so near the cutoff point of 0.05, it could become significant with greater sampling. Therefore, for the purpose of linear regression, force, amplitude and speed are all considered for both the UTS and strain at failure models.

Using Minitab, a linear regression analysis was conducted on both the full X-tensile UTS and strain at failure datasets. By starting, assuming all parameters and their interactions were significant to the model, an iterative approach was conducted to eliminate factors that were not statistically significant. In addition to testing the interaction of force, amplitude and speed, inverse speed and its interactions were also tested. Testing inverse speed compliments the idea of U_{weld} introduced in Section 3.5. The UTS model was found to have amplitude, force, inverse speed, amplitude*inverse speed and force*amplitude as significant factors, while the strain at failure model was found to have amplitude, inverse speed, amplitude*inverse speed and force*amplitude as significant factors. After the statistically significant factors were determined, a random number generator was used to scramble the replicate experiments. The scrambled replicates were divided in to two equal groups. One dataset became the dataset by which the regression model was developed. The other became the validation dataset. Equations

$$UTS = 186 + 1.78 * a + 0.00973 * F_N - \frac{215 * a}{S} + \frac{4620}{S} - 0.000406 * F_N * a \quad (3.2)$$

$$FailureStrain = 0.0660 - 0.00216 * a - \frac{5.08}{S} + \frac{0.225 * a}{S} + 0.00000025 * F_N * a \quad (3.3)$$

show the linear regression models for predicted UTS and failure strain, respectively, where F_N is the normal force applied by the welder [N], a welder amplitude, peak to peak [μm] and S is the weld speed in the X-direction [inches/min].

Table 3.10: Model parameter significance table for X-tensile UTS.

Predictor	Coef	SE Coef	T	P
Constant	185.61	15.24	12.18	0.000
Amplitude	1.783	0.5197	3.43	0.001
Force	0.00973	0.002921	3.33	0.002
1/S	-214.81	32.84	-6.54	0.000
a/S	4620.1	930	4.97	0.000
F*a	-0.00041	0.000101	-4.04	0.000

Table 3.11: Model significance and error table for X-tensile strain at failure.

Source	DF	SS	MS	F	P
Regression	5	7290.3	1458.1	76.07	0.000
Residual Error	42	805	19.2		
Total	47	8095.3			

Table 3.12: Model parameter significance table for X-tensile strain at failure.

Predictor	Coef	SE Coef	T	P
Constant	0.06605	0.01177	5.61	0.000
Amplitude	-0.00216	0.000411	-5.26	0.000
1/S	-5.078	1.217	-4.17	0.000
a/S	0.22497	0.0436	5.16	0.000
F*a	2.5E-07	2E-08	10.34	0.000

Table 3.13: Model significance and error table for X-tensile strain at failure.

Source	DF	SS	MS	F	P
Regression	4	0.010528	0.002632	64.88	0.000
Residual Error	43	0.001744	4.06E-05		
Total	47	0.012273			

As shown in Tables 3.10, 3.11 3.10 and 3.13, each one of the factors within their respective models is statistically significant, with p-values < 0.001. The models were then used to predict UTS and strain at failure using the validation dataset. The models predicted the UTS and strain at failure fairly accurately. Table 3.14 shows a comparison between the prediction and validation dataset for UTS and strain at failure, where: μ is the sample mean; σ_{maxrep} is the maximum standard deviation of replicate data; and σ_{err} is the standard deviation of predicted error. Figures 3.17 and 3.18 show residuals plots for both the UTS and failure strain models, noting that the residual error does not represent a trend.

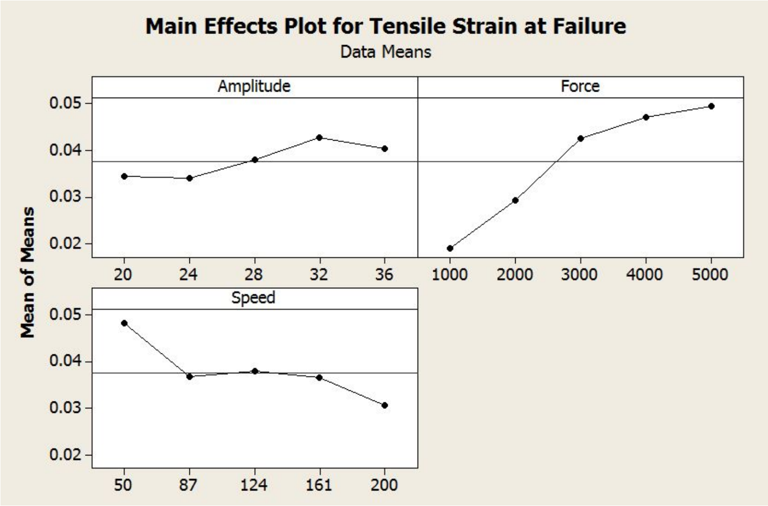

Figure 3.17: UTS regression model residuals plot.

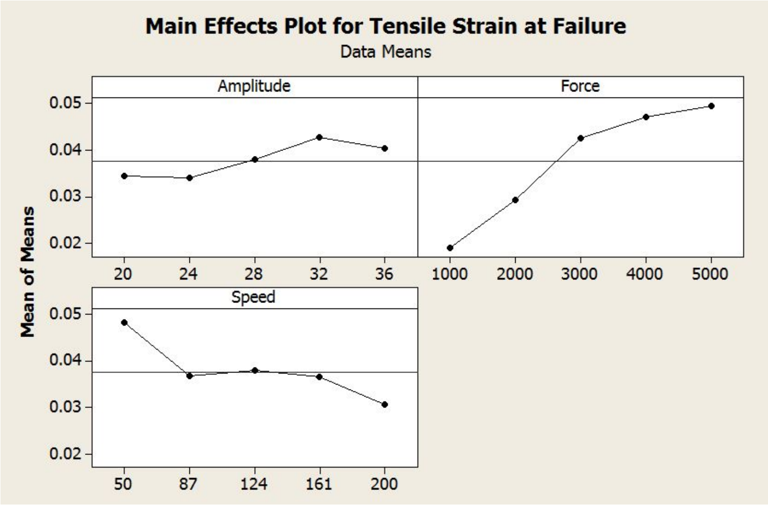

Figure 3.18: Failure strain regression model residuals plot.

Table 3.14: Model validation statistical comparison of error.

	All Data		Prediction Model		Validation Model	
	μ	σ_{maxrep}	σ_{err}	MSE	σ_{err}	MSE
UTS	218.8	6.606290279	4.1386	16.771	3.4595	11.704
Failure Strain	0.0376	0.014036728	0.0061	4E-05	0.0207	0.0005

Although both models seem to predict UTS and failure strain fairly accurately, there are potential limitations of the model:

1. The first limitation is that the model is only valid within the range of the parameters tested. The UAM machine is capable of operating at speeds between 25 and 300 inches per minute, forces of up to 10,000 N and amplitudes of up to 50 μm. Past studies of UAM welding with Al 6061-H18 [11] show a process window with adequate welds within the parameter sets used for this study, but the machine is capable of a larger range for each parameter set.
2. The second limitation of this model is that it has only been tested with certain sets of parameters. The parameter sets were chosen from six available combinations to maximize the number of experimental sets that can be welded, but it is possible that some effects were missed at different combinations of parameters.
3. A third limitation of this model is that it is a continuous linear regression model developed using levels of parameters, and not continuous parameters. To help minimize this limitation, when the study was developed it used 5 levels of weld parameters, compared to three level parameters used in other UAM experimental designs. Although this limitation was attempted to be minimized

through the use of more levels, it is possible that some effects are missed as a result.

3.6 Key Findings and Recommendations

This study showed that all three input parameters studied were statistically significant or nearly statistically significant in the response of UTS and failure strain. Those parameters were used to develop a linear regression model. Additionally, stress-strain tensile behavior of welded material in the X-direction was shown to correlate well with the weld energy density term introduced as part of this study. This could provide insight for future UAM modeling efforts.

Key Findings:

- Weld force, speed and amplitude affect X-direction tensile strength and strain at failure.
- A statistical model can be used to predict X-direction tensile strength and strain at failure.
- U_{weld} can be used to predict the appearance of a double or single yield point, with higher U_{weld} correlating with high dislocation density, the hypothesized cause for a double yield point.

Recommendations:

- It is noted that this study did not attempt to quantify the strength or quality of the welds, but how UAM welded material is affected by weld parameters in the X-direction. Future work can compare the results of this study with weld quality/strength to determine if there is a relationship.

- To better support the results of this study and the statistical model, tensile specimens using parameter sets that were not constructed as part of this study can be built and tested, helping to further develop the statistical model. The additional sample sets can be used to fill in the gaps in U_{weld} shown in Figure 3.10, ensuring that the calculated U_{weld} for the sample sets corresponds to the area without available data.

- It appears as if there is an inverse relationship between weld quality and the strength in the X-direction, but a DOE on weld strength can be used to further investigate.

- The hypothesis was made that the presence of a high dislocation density within the samples tested as part of this DOE is the cause for a double yield point. Microscopy can be conducted to verify this hypothesis.

- Residual stress measurements can be taken, possibly during different steps during the build process, to help account for the loss in strength found to be a function of weld parameters in a attempt to correlate with potential residual stresses within the UAM build.

Chapter 4: Contributions and Future Work

The goal of this thesis was to present a means of lightweighting components and improve their strength through the use of UAM. This thesis shows that lightweighting is possible through the use of UAM created metal matrix composites. The thesis is broken into lines of research, the first being fiber reinforcement of aluminum using UAM, and, inspired from findings in the reinforcement study, a study to glean insight into the cause for the reduction in strength of UAM constructed components in the X-direction.

With the goal of determining a means to create lightweight and strong metal matrix composites using UAM, a study was conducted using different fiber types and embedding and reinforcing techniques. The reinforcement study explored two new aspects to UAM as a means to reinforce base material. The first being a look at different materials, such as thermoplastics and thermoset polymers. The second being using UAM to directly reinforce a thin (0.9 mm) base material, both by welding Al 6061-H18 to the base, and by embedding reinforcing fibers within the aluminum, making an overall stronger component, relative to density. This study added several new contributions to the UAM community including: directly embedding HSS wires within an Al 6061-H18 matrix without using channels; embedding aramid thread bundles inside machined channels within 6061-H18 matrix; welding Al 6061-H18 tapes to a 0.9 mm thick Al 5052-O baseplate; and embedding Zylon, Dyneema and SiC fiber bundles, individually, inside a machined channel within an Al 6061-H18/Al 5052-O matrix. One of the major findings from this study is that fiber friction alone is not enough to absorb significant composite load without slipping within a channel, but slipping of the fiber within the matrix can be used to increase the overall toughness of a composite with the fibers continuing to bear load after matrix failure. If MetPreg can be acquired that meets the advertised properties, it may prove to be an excellent means of reinforcing thin sheets. Additionally, this study shows that welding on thin sheets has its complications, but has great potential for integrating the base material into the final part, instead of using the base as something to be discarded.

Recommendations for related future work include: investigating a means to improve matrix-fiber interface to allow the fiber to bear more load, increasing the overall strength of the composite; tuning the slippage of fibers within the matrix to maximize fiber loading without breaking, allowing the fiber to continue to bear load beyond its normal failure strain; and exploring other types of thin base plate materials with higher yield strengths to determine if the deformation of the base can be avoided, and successful welds produced. Additionally, embedding fibers in complex channels or chemically treating fibers to improve mechanical interlocking can help to improve the friction between the fibers and the channel, allowing them to bear more load under tension.

Through the investigations described above, attempting different methods to maximize the strength of aluminum matrix composites constructed using UAM, it was noted that there was a reduction in strength of the aluminum matrix, post UAM welding, compared with the as received tape. To better understand the cause for the reduction in strength, a DOE was conducted to determine if varying weld parameters contributes to varying strength within the UAM constructed parts, and if an optimal set of parameters exists to improve X-direction tensile strength. The key findings of this study include: that all three input parameters studied were statistically significant or nearly statistically significant in the response of UTS and failure strain. A linear regression model was developed that accurately predicts X-direction UTS of UAM welded Al 6061-H18 as a function of input parameters. Additionally, stress-strain tensile behavior of welded material in the X-direction, more specifically the presence of a double or single yield point, was shown to correlate well with a high or low weld energy density term, respectively. This correlation could provide insight for future UAM modeling efforts. Ultimate tensile strength in the weld direction was shown to be dependent upon the weld force, weld speed and weld amplitude, while the failure strain was only dependent upon weld force. This changes the way that we look at the weld parameters that are chosen.

Future work can help to better this study, and explore a wider parameter set to fill in areas not covered in the partial factorial study conducted. To better support the results of this study and the statistical model, tensile specimens using parameter sets that were not constructed as part of this study can be built and tested, helping to further develop the statistical model. The additional sample sets can be used to fill in the gaps in U_{weld} shown in Figure 3.10, ensuring that the area with the divide is represented in the sample space. It is important to note that this study did not attempt to quantify the strength or quality of the welds, but how UAM welded material is affected by weld parameters in the X-direction. Future work can compare the results of this study with weld quality/strength to determine if there is a relationship. It appears as if there is an inverse relationship between the presence of gapless welds and the strength in the X-direction, but a DOE on weld strength can be used to further investigate. Previous experimental designs using a 9 kW UAM system looked at force, amplitude and speed, and determined that force had no statistical effect on the quality of welds (stack direction). With this understanding, and in the future, coupling these results with weld quality at the same parametric input, a better understanding of the choice in weld parameters can be achieved. Future work can also use these results as a stepping stone toward a model that describes the welding process as a function of input parameters. In support of the hypothesis that the presence of a high dislocation density is the cause for the observance of a double yield point, microscopy can be conducted to measure the density of dislocations for different builds. Residual stress measurements can be taken, possibly during different steps during the build process, to help account for the loss in strength found to be a function of weld parameters in an attempt to correlate with potential residual stresses within the UAM build.

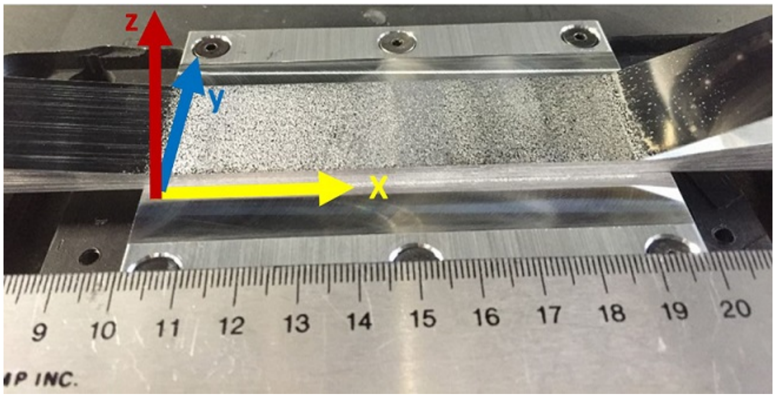

Figure 4.1: UAM build on small plate showing X, Y, and Z directions.

All of the work presented in this thesis has focused on improving and understanding the strength of UAM created coupons along the x-direction, as shown in Figure 4.1. What has still not been quantified is the strength of components in the Y and Z directions as a function of weld parameter choice. It is possible that tensile strain that causes a reduction in strength in the X-direction is compressive in the Y-direction.

Future work can also help to develop a fundamental understanding of why the parameter set variation causes the overall reduction in ultimate tensile strength. Additionally, future work can help to determine why the strain at failure varies from both above and below the failure strain of the aluminum tape it was created with. The statistical model can predict UTS and strain at failure for the parameter sets tested, but why those parameter sets affect the behavior in the way that they do is not understood. Although this thesis touches on some possible explanations of how weld parameters influence UAM welds, much work can be done to help shape the understanding of how and why parameter choice effects UAM builds, and how to take advantage of that understanding.

Bibliography

[1] National Highway Traffic Safety Administration. CAFE - fuel economy. `http://www.nhtsa.gov/fuel-economy`. Accessed: 2016-03-29.

[2] National Aeronautics and Space Administration. Advanced Space Transportation Program: Paving the highway to space. `http://www.nasa.gov/centers/marshall/news/background/facts/astp.html_prt.htm`. Accessed: 2016-03-29.

[3] M. R. Sriramana, S. S. Babu, and M. Short. Bonding characteristics during very high power ultrasonic additive manufacturing of copper. *Scripta Materialia*, 62: 560–563, 2010.

[4] B. D. Agarwal, L. J. Broutman, and K. Chandrashekhara. *Analysis And Performance Of Fiber Composites Third Edition*. John Wiley & Sons, 2006.

[5] K. Chawla. *Composite Materials Science and Engineering, Second Edition*. Springer, 1998.

[6] ASTM International. E8/E8M-08: Standard test method for tension testing of metallic materials, 2008.

[7] Jr. W. D. Callister. *Materials Science and Engineering An Introduction.* John Wiley and Sons, Inc, 2007.

[8] C. DiFrancia, T. C. Ward, and R. O. Claus. The single-fibre pull-out test. 1: Review and interpretation. *Composites Part A: Applied Science and Manufacturing*, 27:597–612, 1996.

[9] A. Hehr, J. Pritchard, and M. J. Dapino. Interfacial shear strength estimates of niti - al matrix composites fabricated via ultrasonic additive manufacturing. *Procedings of SPIE*, 9059, 2014.

[10] R0oland. Diagram illustrating the light path through a dark field microscope. `https://en.wikipedia.org/wiki/Dark_field_microscopy#/media/File:Dark_Field_Microscope_@D..svg`. Accessed: 2016-05-25.

[11] P. J. Wolcott, A. Hehr, and M. J. Dapino. Optimal welding parameters for very high power ultrasonic additive manufacturing of smart structures with aluminum 6061 matrix. *Proceedings SPIE 9059,Industrial and Commercial Applications of Smart Structures Technologies 2014*, 9059:905908–1 thru 14, 2014.

[12] G. D. J. Ram, Y. Yang, J. George, C. Robinson, and B. E. Stucker. Improving linear weld density in ultrasonically consolidated parts. *Solid Freeform Fabrication Proceedings*, pages 692–708, 2006.

[13] Y. Yang. *Fabrication of Long-Fiber-Reinforced Metal Matrix Composites Using Ultrasonic Consolidation.* PhD thesis, Utah State University, 2008.

[14] R. Gonzalez. A study on stainless steel 316l annealed ultrasonic consolidation and linear welding density estimation. Master's thesis, Utah State University, 2010.

[15] P. J. Wolcott, A. Hehr, C. Pawlowski, and M. J. Dapino. Process improvements and characterization of ultrasonic additive manufactured structures. *Journal of Materials Processing Technology*, 233:44–52, 2016.

[16] P. Wolcott. *Ultrasonic Additive Manufacturing: Weld Optimization for Aluminum 6061, Development of Scarf Joints for Aluminum Sheet Metal, and Joining of High Strength Metals.* PhD thesis, Ohio State University, 2015.

[17] H. B. Mann. *Analysis And Design of Experiments, Analysis of Variance and Analysis of Variance Designs.* Dover Publications, 1949.

[18] A. Dean and D. Voss. *Analysis And Design of Experiments.* Springer, 1998.

[19] G. W. Oehlert. *A First Course in Design and Analysis of Experiments.* W. H. Freeman and Company, 2000.

[20] Y. Yang, G. D. J. Ram, and B. E. Stucker. An experimental determination of optimum processing parameters for al/sic metal matrix composites made using ultrasonic consolidation. *Journal of Engineering Materials and Technology*, 129, 2007.

[21] M. H. DeGroot and M. J. Schervish. *Probability and Statistics, Fourth Edition.* Addison-Wesley, 2012.

[22] D. R. White. Ultrasonic consolidation : Status report on development of solid state net shape processing for direct manufacturing, 2006.

[23] G. D. J. Ram, C. Robinson, and B.E. Stucker. Multi-material ultrasonic consolidation. *Proceedings of the Sff Symposium*, 18, 2006.

[24] J. Obielodan and B. Stucker. A fabrication methodology for dual-material engineering structures using ultrasonic additive manufacturing. *International Journal of Advanced Manufacturing Technology*, 70:277–284, 2014.

[25] I. Gibson, D. Rosen, and B. Stucker. *Additive Manufacturing Technologies: 3D Printing, Rapid Prototyping, and Direct Digital Manufacturing, Second Edition*. Springer, 2015.

[26] D. O. Jarrett, J. M. Gibert, and G. M. Fadel. Performance of stainless steel aisi 304 wire reinforced metal matrix composites made using ultrasonic additive manufacturing in bending. *Proceedings of the Sff Symposium*, 2012.

[27] Touchstone Research Laboratory. Metpreg datasheet. `http://metpreg.com/documents/MetPreg_Datasheet_Metal_Aluminum_Matrix_Composite.pdf`. Accessed: 2016-06-26.

[28] ASTM International. A228/A228M-14: Standard specification for steel wire, music spring quality, 2014.

[29] TowMasters. Fiber data technical bulliten. `https://towmasters.files.wordpress.com/2009/05/fiber_characteristics_and_rope_construction.pdf`. Accessed: 2016-01-12.

[30] MakeItFrom. 5052-h12 aluminum. `http://www.makeitfrom.com/material-properties/5052-H12-Aluminum/`. Accessed: 2016-01-12.

[31] J. E. Hatch, editor. *Aluminum: Properties And Physical Metallurgy.* ASM International, 1984.

[32] D. E. Shick, R. M. Hahnlen, R. Dehoff, P. Collins, S. S. Babu, M. J. Dapino, and J. C. Lippold. Microstructural characterization of bonding interfaces in aluminum 3003 blocks fabricated by ultrasonic additive manufacturing-methods were examined to link microstructure and linear weld density to the mechanical properties of ultrasonic additive manufacturing. *Welding Journal*, pages 105–s thru 115–s, 2010.

[33] H. Huang. A taguchi-based heterogeneous parallel metaheuristic aco-pso and its fpga realization to optimal polar-space locomotion control of four-wheeled redundant mobile robots. *IEEE Transactions on Industrial Informatics*, 11:915–922, 2015.

[34] MiniTab Inc. Taguchi designs. `http://support.minitab.com/en-us/minitab/17/topic-library/modeling-statistics/doe/taguchi-designs/taguchi-designs/`. Accessed: 2016-06-26.

[35] A. H. Cottrell. Dislocation theory of yielding and strain ageing of iron. *Proceedings of the Physical Society*, 62:49–62, 1949.

[36] L. F. Mondolfo. *Aluminum Alloys: Structure and Properties.* Butterworths, 1976.

Appendix A: Welding Parameters

A.1 Procedure for Testing Factory 0.016”x0.5” MetPreg Tape Samples

1. Cut 0.016 in. x0.5 in. MetPreg Tape to 3.5 inches.
2. Attach aluminum tabs using resin to allow for test apparatus grip.
3. Install tabs into test apparatus.
4. Using LabView, ramp strain at 0.05 inches per minute until failure while simultaneously recording force and displacement over time.

A.2 Work Hardening Procedure for 0.016 in. x0.5 in. MetPreg Tape

1. Cut 0.016 in. x0.5 in. MetPreg Tape to 5 inches.
2. Secure 0.016 in. x0.5 in. MetPreg Tape test samples using tape to a steel plate mounted on a vacuum chuck in the Fabrisonic UAM machine.
3. Using the welder settings listed below, run welder over 0.016 in. x0.5 in. MetPreg Tape samples for 3.5 inches.

No ultrasonics

No tape

5000 N tack force

5000 N weld force

4. Remove sample and repeat for remaining samples.

A.3 Creating UAM Aluminum Only samples

1. Mount steel fixture to vacuum chuck.
2. Mount 3 in. x4 in. x0.190 in. base plate to steel fixture.
3. Cut 1.5 in. channel 0.015 in. deep through center of base plate.
4. Texture base plate channel to prepare for welding using below settings:

   No tape

   27 μm tack amplitude

   6000 N tack force

   27 μm weld amplitude

   6000 N weld force

   225 μsec tack dwell time

   200 in/min weld speed
5. Weld one 1 in. x0.006 in. tape for a 3.5 in. weld length using below parameters:

   With tape

29 μm tack amplitude

5000 N tack force

29 μm weld amplitude

5000 N weld force

225 μsec tack dwell time

200 in/min weld speed

6. Ensure that the base plate is secure. (Ultrasonic welding has a tendency to loosen (slightly) the base plate. Only have to re-tighten once.
7. Weld 11 more layers of Aluminum 6061 tape using same parameters.
8. Cut out test coupon shape from welded materials using CNC program.

A.4 0.016 in. x0.5 in. MetPreg Tape Test Coupon Construction

1. Weld 6 layers of Aluminum 6061 using above procedures
2. Tape layer of 0.016 in. x0.5 in. MetPreg Tape over recently welded material through center of weld.
3. Tape layer of 0.006 in. Titanium tape over 0.016 in. x0.5 in. MetPreg Tape
4. Weld 0.016 in. x0.5 in. MetPreg Tape to 6061 weld using below parameters.

No tape

36 μm tack amplitude

2000 N tack force

36 μm weld amplitude

2000 N weld force

200 μsec tack dwell time

40 in/min weld speed

5. Peel off Titanium Tape. (sticks slightly but peels back easily)
6. Weld 4 layers of Al 6061 over 0.016 in. x0.5 in. MetPreg Tape using below parameters:

   With tape

   29 μm tack amplitude

   5000 N tack force

   29 μm weld amplitude

   5000 N weld force

   250 μsec tack dwell time

   200 in/min weld speed

A.5 HSS Wire Embedding Procedure

1. Weld 6 layers of Aluminum 6061 tape using above procedures.
2. Mount 4 wires axisymmetric with weld direction in tension to allow them to remain straight.
3. Weld 1 layer of Aluminum 6061 tape using above procedures.

A.6 Individual Kevlar Thread Embedding Procedure

4. Weld 6 layers of Aluminum 6061 tape using above procedures.
5. Cut 4 channels, 0.015625 in. wide and 0.008 in. deep axisymmetric with weld direction.
6. Mount 4 threads within the channel.
7. Weld 1 layer of Aluminum 6061 tape using below parameters.

   With tape

   32.5 μm tack amplitude

   3000 N tack force

   32.5 μm weld amplitude

   3000 N weld force

   225 μsec tack dwell time

   200 in/min weld speed

A.7 Aramid Thread Flat Bundle Embedding Procedure

1. Weld 5 layers of Aluminum 6061 tape using above procedures.
2. Cut 1 channel, 0.125 in. wide and 0.005 in. deep, axisymmetric with weld direction.
3. Mount 18 threads within the channel.

4. Weld 1 layer of Aluminum 6061 tape using below parameters.

   With tape

   28.96 μm tack amplitude

   6000 N tack force

   28.96 μm weld amplitude

   6000 N weld force

   275 μsec tack dwell time

   200 in/min weld speed

5. Change tack and weld amplitude to 20.79 μm and weld over the top of previously laid tape (no tape added).

6. Change tack and weld amplitude to 24.87 μm and weld over the top of previously laid tape (no tape added).

7. Repeat steps 4, 5, and 6 twice.

8. Change tack and weld amplitude to 31 μm and weld over the top of previously laid tape (no tape added).

A.8 Aramid Twisted Bundle Embedding Procedure

1. Weld 6 layers of Aluminum 6061 tape using above procedures.

2. Cut 1 channel, 0.0625 in. wide and 0.020 in. deep, axisymmetric with weld direction.

3. Mount 40 threads within the channel.

4. Weld 1 layer of Aluminum 6061 tape using below parameters.

    With tape

    28.96 μm tack amplitude

    6000 N tack force

    28.96 μm weld amplitude

    6000 N weld force

    275 μsec tack dwell time

    200 in/min weld speed

5. Change tack and weld amplitude to 20.79 μm and weld over the top of previously laid tape (no tape added).
6. Change tack and weld amplitude to 24.87 μm and weld over the top of previously laid tape (no tape added).
7. Repeat steps 4, 5, and 6 twice.
8. Change tack and weld amplitude to 31 μm and weld over the top of previously laid tape (no tape added).

*NOTE: While both methods of adding aramid were successful, a greater volume fraction of aramid was achieved using the second method; 5% vs 12%. Also, by the nature of the twisting action, the threads are less likely to pull out individually with the tight bundle over the flat strip of threads.

Appendix B: Knock-Off Study Stress-Strain Curves

Table B.1: Knockoff DOE treatments.

Treatment Number	Amplitude [micron]	Force [N]	Speed [mm/s]
1	20	1000	21
2	20	2000	37
3	20	3000	52
4	20	4000	68
5	20	5000	85
6	24	1000	37
7	24	2000	52
8	24	3000	68
9	24	4000	85
10	24	5000	21
11	28	1000	52
12	28	2000	68
13	28	3000	85
14	28	4000	21
15	28	5000	37
16	32	1000	68
17	32	2000	85
18	32	3000	21
19	32	4000	37
20	32	5000	52
21	36	1000	85
22	36	2000	21
23	36	3000	37
24	36	4000	52
25	36	5000	68

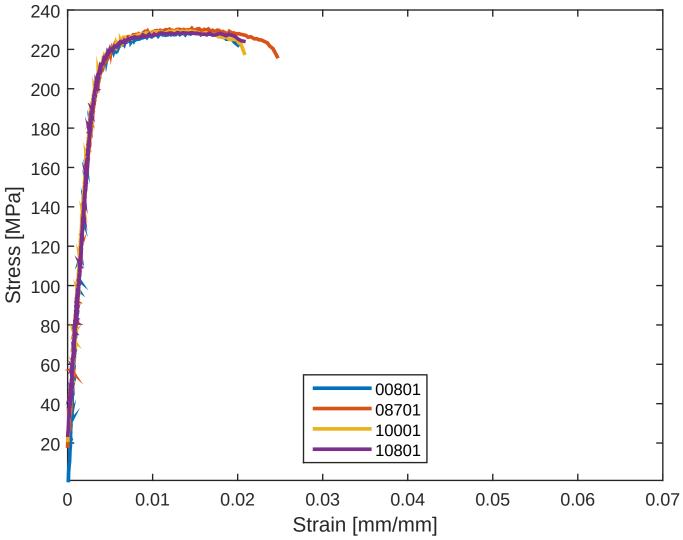

Figure B.1: Stress-strain plot of knockoff sample set #01.

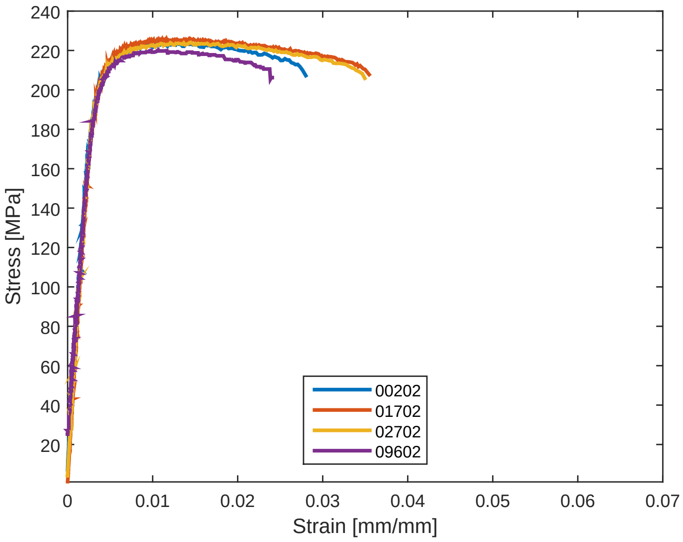

Figure B.2: Stress-strain plot of knockoff sample set #02.

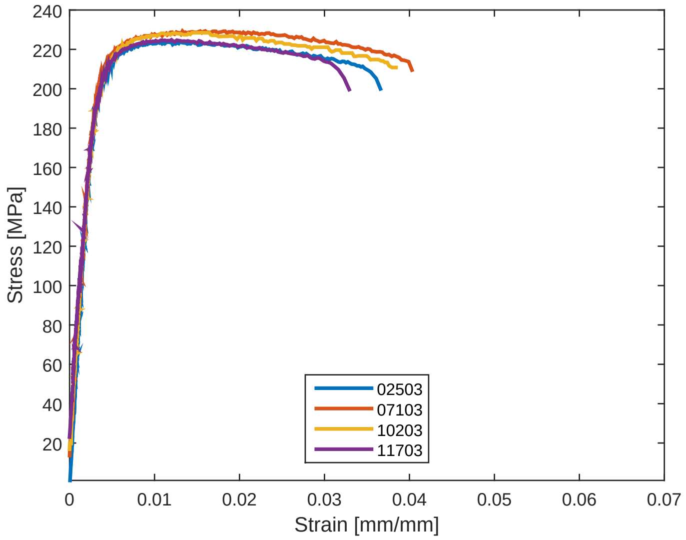

Figure B.3: Stress-strain plot of knockoff sample set #03.

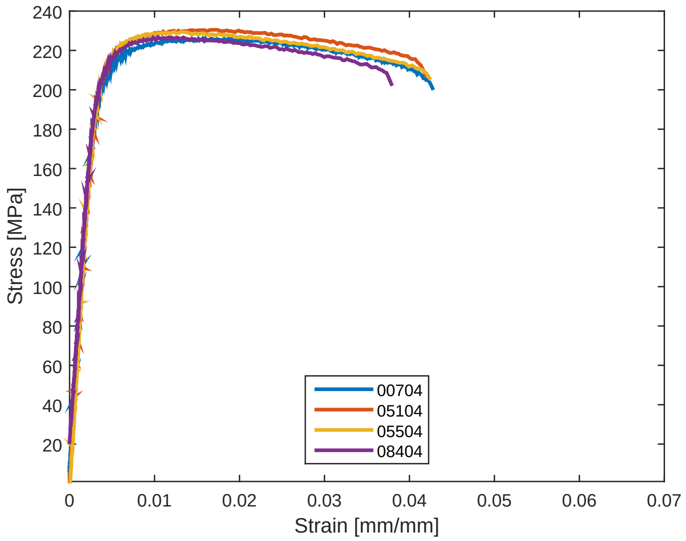

Figure B.4: Stress-strain plot of knockoff sample set #04.

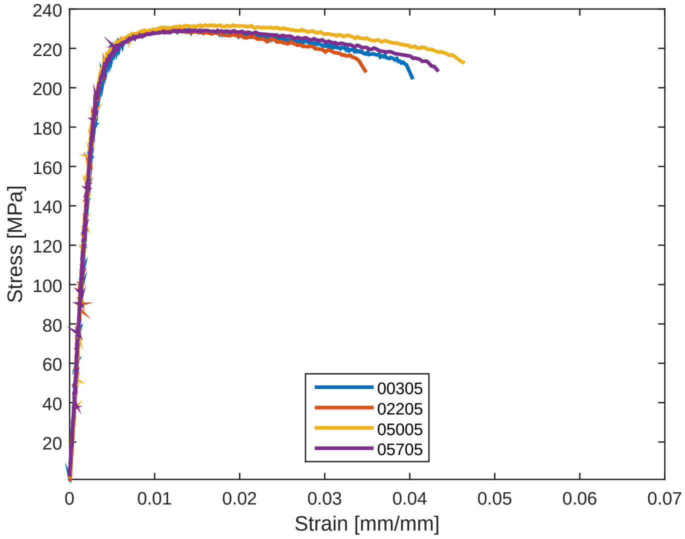

Figure B.5: Stress-strain plot of knockoff sample set #05.

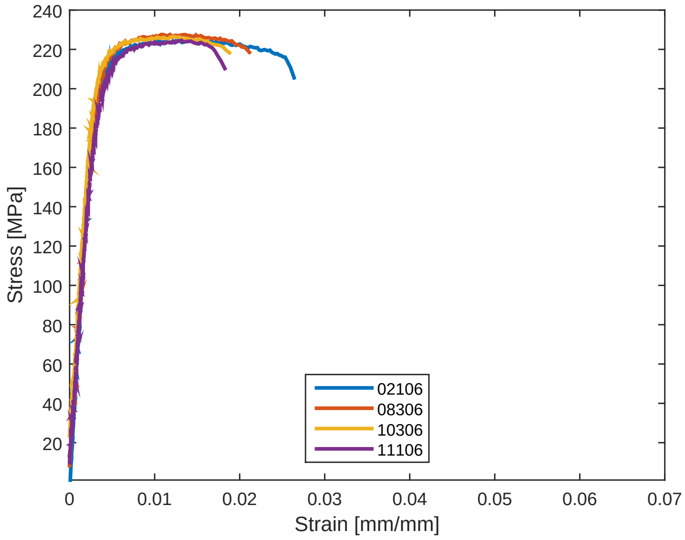

Figure B.6: Stress-strain plot of knockoff sample set #06.

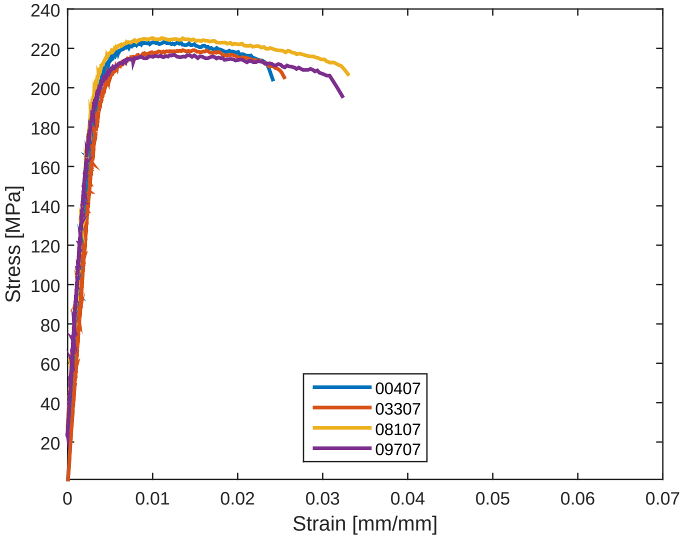

Figure B.7: Stress-strain plot of knockoff sample set #07.

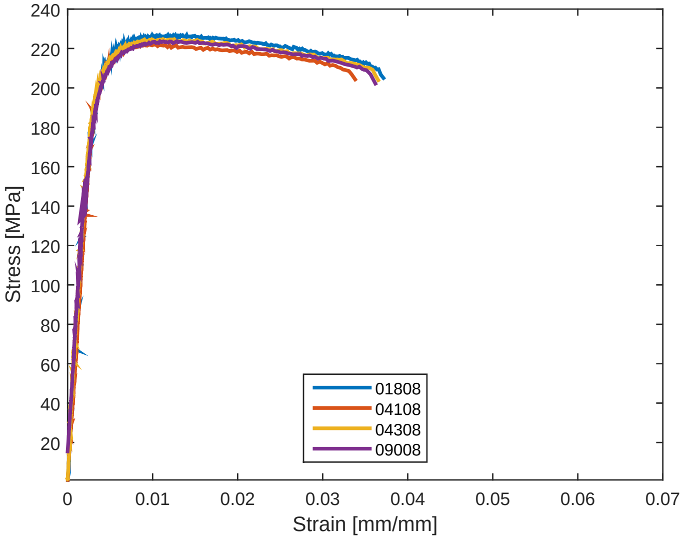

Figure B.8: Stress-strain plot of knockoff sample set #08.

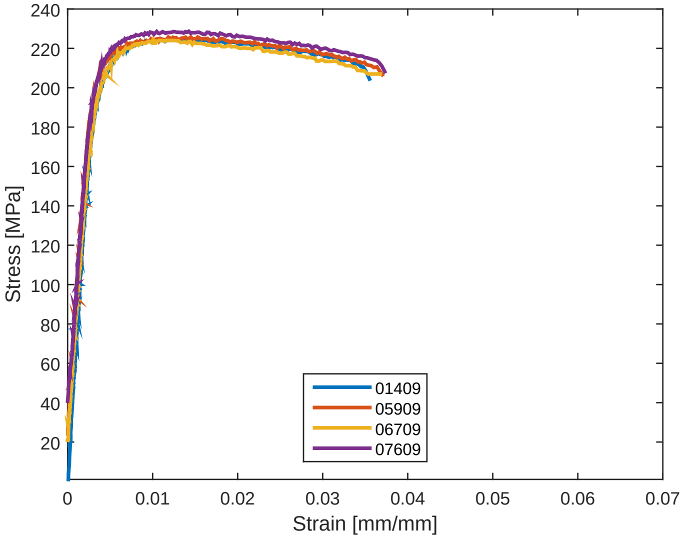

Figure B.9: Stress-strain plot of knockoff sample set #09.

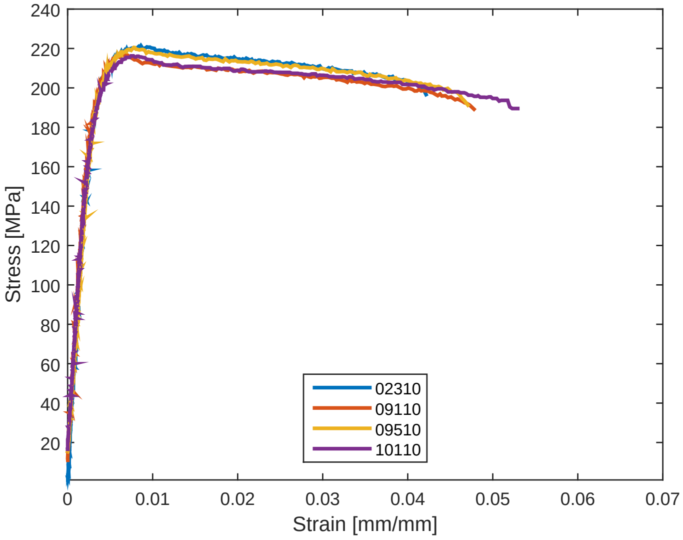

Figure B.10: Stress-strain plot of knockoff sample set #10.

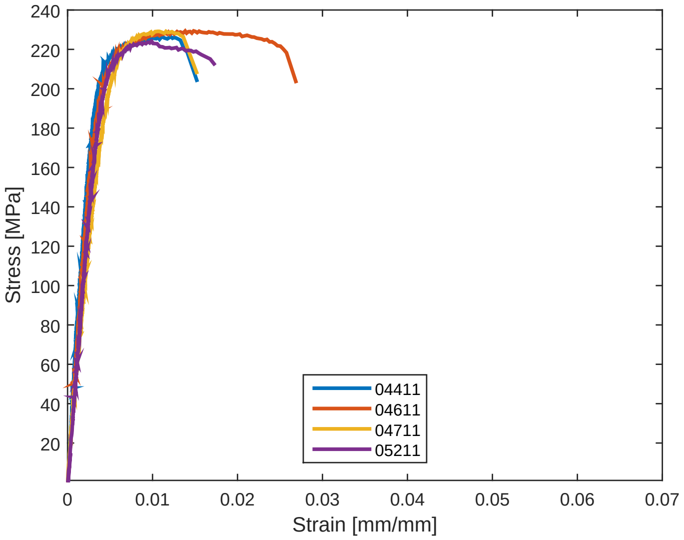

Figure B.11: Stress-strain plot of knockoff sample set #11.

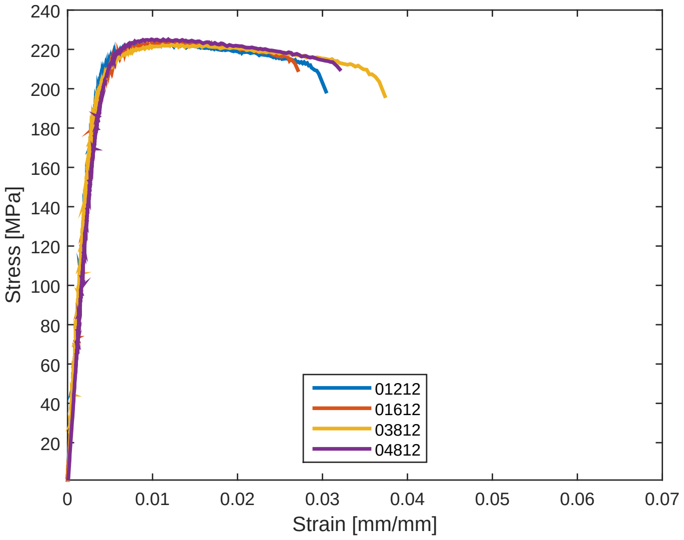

Figure B.12: Stress-strain plot of knockoff sample set #12.

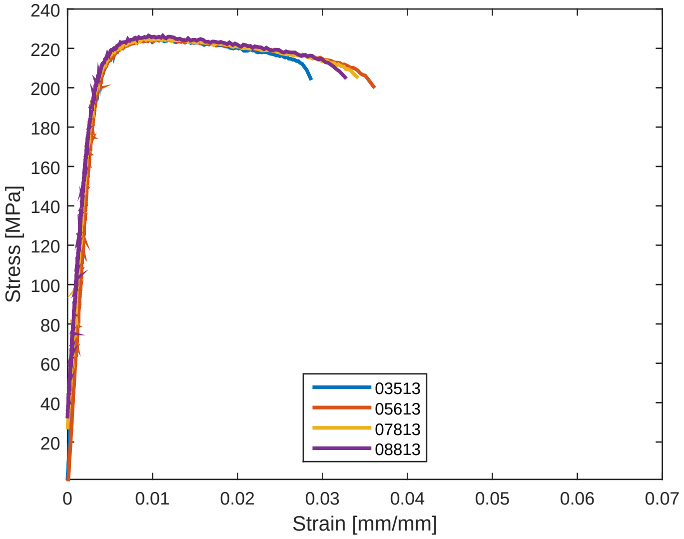

Figure B.13: Stress-strain plot of knockoff sample set #13.

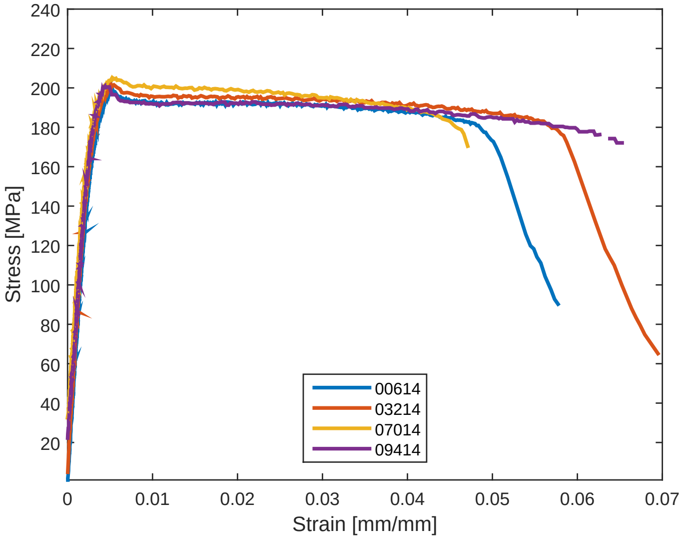

Figure B.14: Stress-strain plot of knockoff sample set #14.

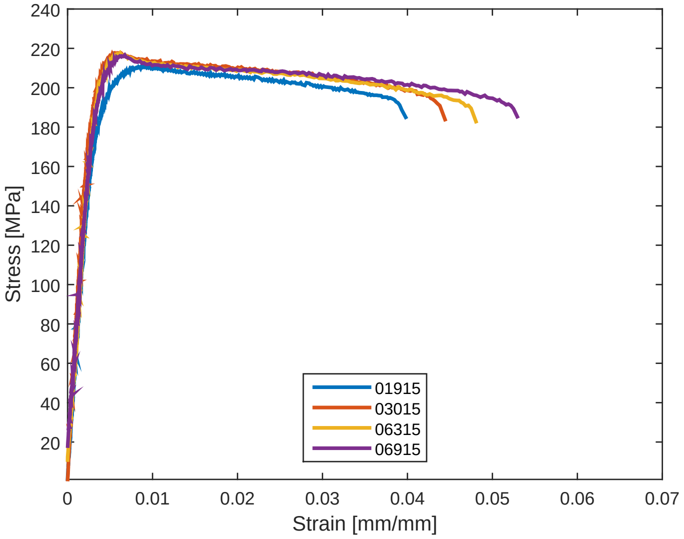

Figure B.15: Stress-strain plot of knockoff sample set #15.

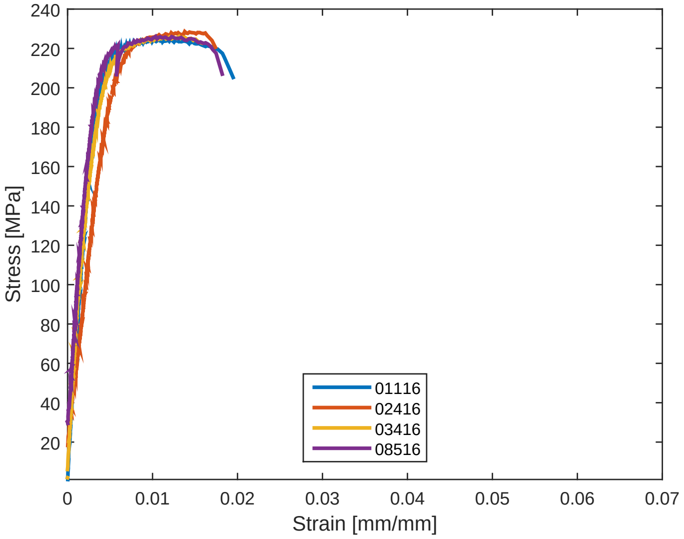

Figure B.16: Stress-strain plot of knockoff sample set #16.

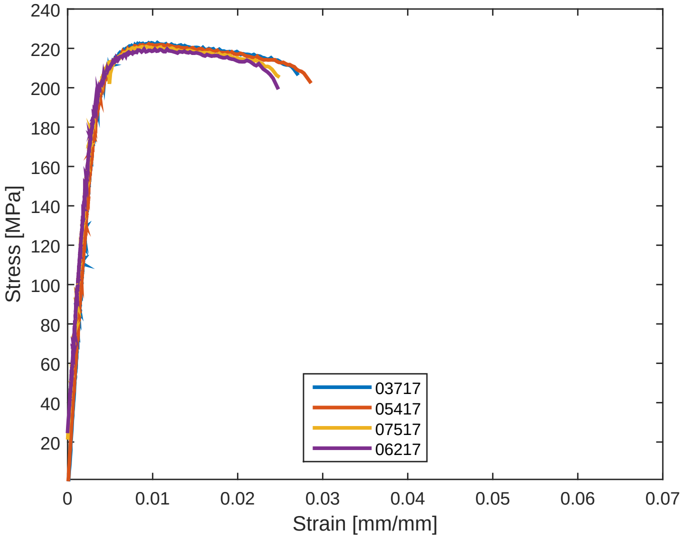

Figure B.17: Stress-strain plot of knockoff sample set #17.

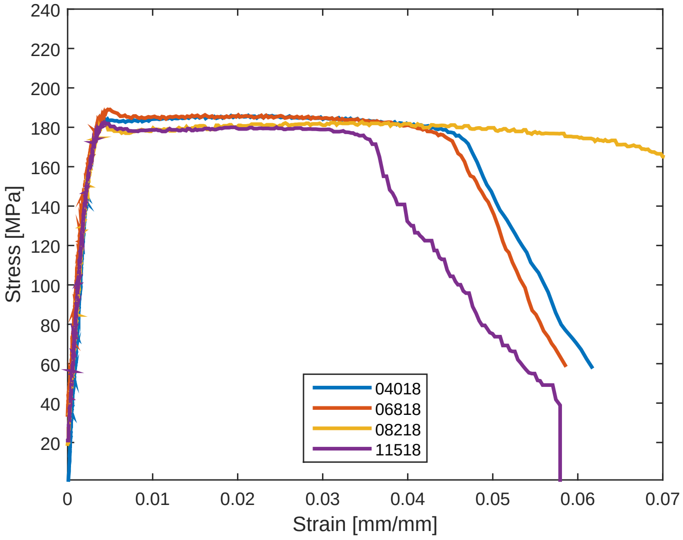

Figure B.18: Stress-strain plot of knockoff sample set #18.

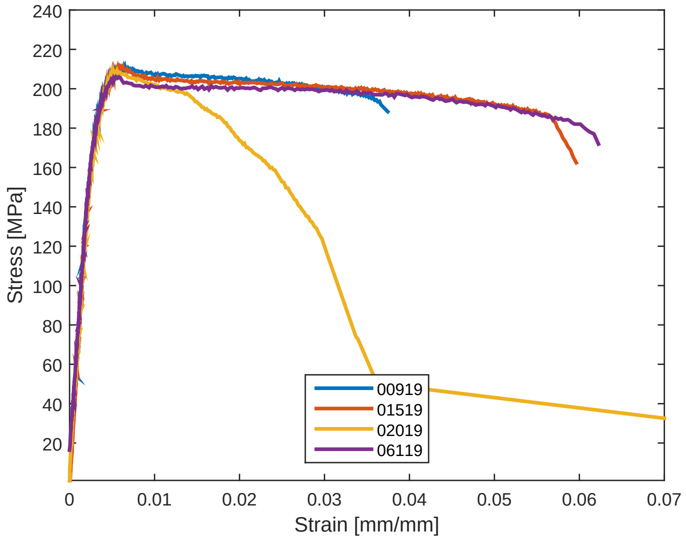

Figure B.19: Stress-strain plot of knockoff sample set #19.

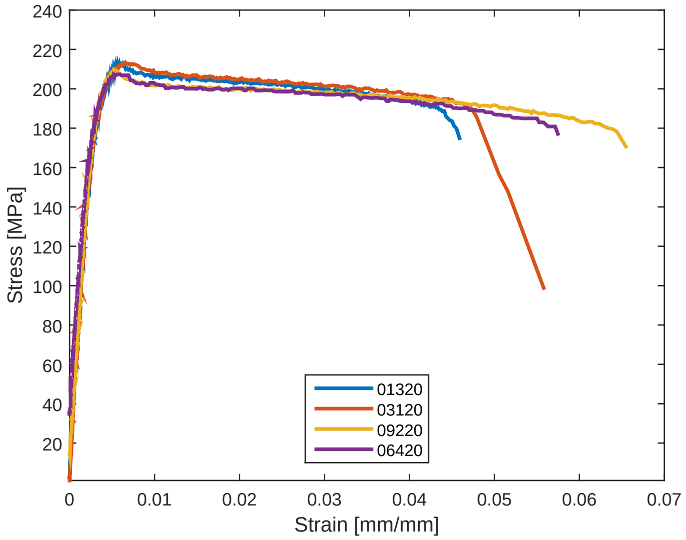

Figure B.20: Stress-strain plot of knockoff sample set #20.

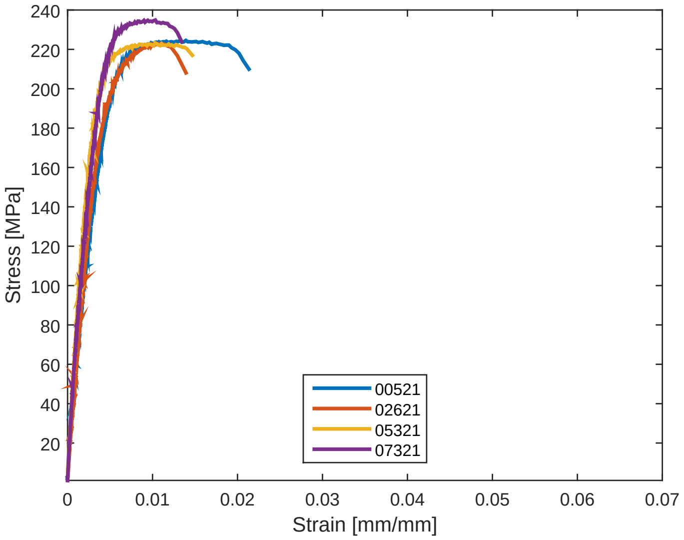

Figure B.21: Stress-strain plot of knockoff sample set #21.

Sample could not be constructed due to nuggetting.

Figure B.22: Stress-strain plot of knockoff sample set #22.

Sample could not be constructed due to nuggetting.

Figure B.23: Stress-strain plot of knockoff sample set #23.

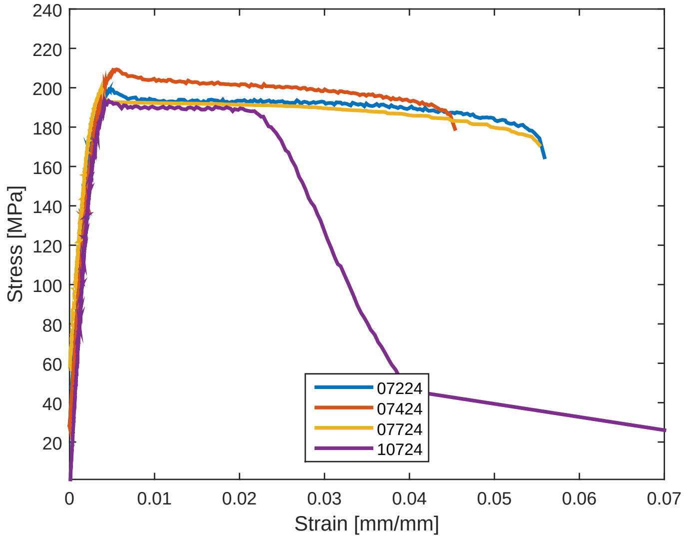

Figure B.24: Stress-strain plot of knockoff sample set #24.

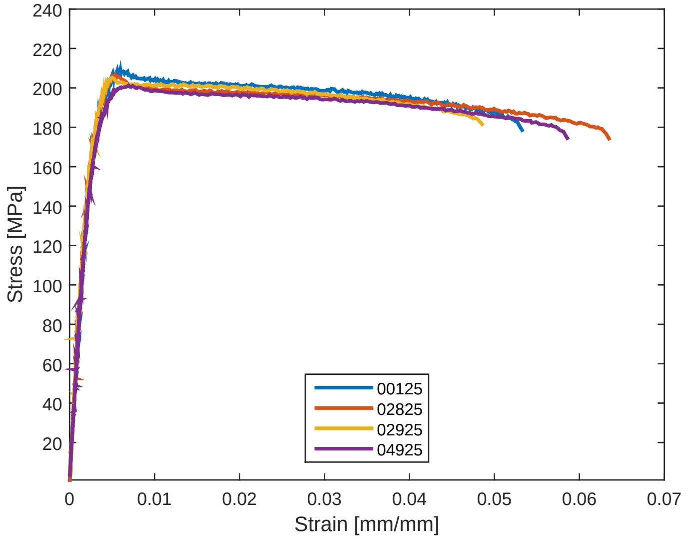

Figure B.25: Stress-strain plot of knockoff sample set #25.

Appendix C: Knock-Off Study Sample Photographs

Table C.1: Knockoff DOE treatments.

Treatment	**Amplitude**	**Force**	**Speed**
Number	**[micron]**	**[N]**	**[mm/s]**
1	20	1000	21
2	20	2000	37
3	20	3000	52
4	20	4000	68
5	20	5000	85
6	24	1000	37
7	24	2000	52
8	24	3000	68
9	24	4000	85
10	24	5000	21
11	28	1000	52
12	28	2000	68
13	28	3000	85
14	28	4000	21
15	28	5000	37
16	32	1000	68
17	32	2000	85
18	32	3000	21
19	32	4000	37
20	32	5000	52
21	36	1000	85
22	36	2000	21
23	36	3000	37
24	36	4000	52
25	36	5000	68

Figure C.1: Photograph of knockoff study treatment #01.

Figure C.2: Photograph of knockoff study treatment #02.

Figure C.3: Photograph of knockoff study treatment #03.

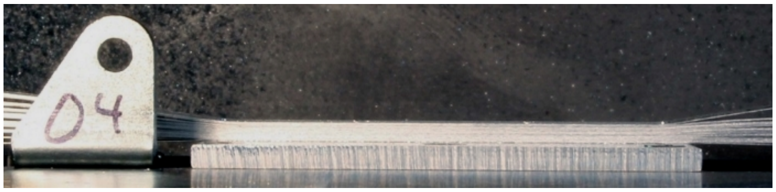

Figure C.4: Photograph of knockoff study treatment #04.

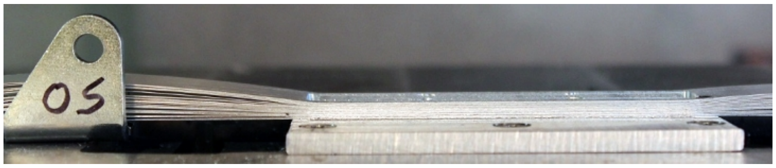

Figure C.5: Photograph of knockoff study treatment #05.

Figure C.6: Photograph of knockoff study treatment #06.

Figure C.7: Photograph of knockoff study treatment #07.

Figure C.8: Photograph of knockoff study treatment #08.

Figure C.9: Photograph of knockoff study treatment #09.

Figure C.10: Photograph of knockoff study treatment #10.

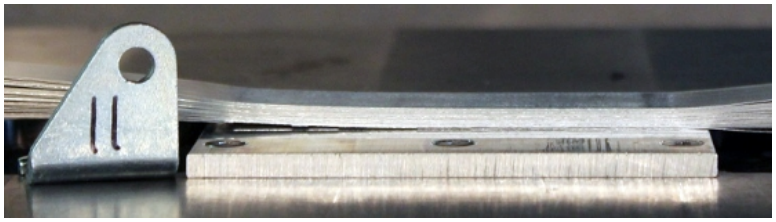

Figure C.11: Photograph of knockoff study treatment #11.

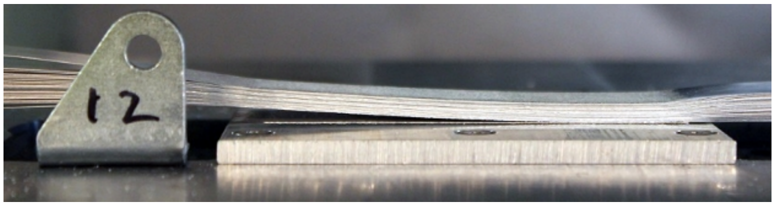

Figure C.12: Photograph of knockoff study treatment #12.

Figure C.13: Photograph of knockoff study treatment #13.

Figure C.14: Photograph of knockoff study treatment #14.

Figure C.15: Photograph of knockoff study treatment #15.

Figure C.16: Photograph of knockoff study treatment #16.

Figure C.17: Photograph of knockoff study treatment #17.

Figure C.18: Photograph of knockoff study treatment #18.

Figure C.19: Photograph of knockoff study treatment #19.

Figure C.20: Photograph of knockoff study treatment #20.

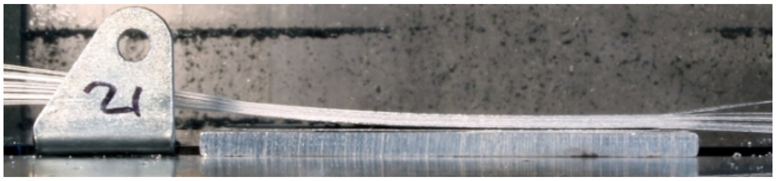

Figure C.21: Photograph of knockoff study treatment #21.

Sample could not be constructed due to nuggetting.

Figure C.22: Photograph of knockoff study treatment #22.

Sample could not be constructed due to nuggetting.

Figure C.23: Photograph of knockoff study treatment #23.

Figure C.24: Photograph of knockoff study treatment #24.

Figure C.25: Photograph of knockoff study treatment #25.